

## **Integration of a rib-channel design to improve air-side contacting in solid oxide cell (SOC) stacks**

Yavuz Selim Ayhan

Energie & Umwelt / Energy & Environment

Band / Volume 651

ISBN 978-3-95806-797-4





Forschungszentrum Jülich GmbH  
Institute of Energy Materials and Devices (IMD)  
Werkstoffsynthese und Herstellungsverfahren (IMD-2)

# **Integration of a rib-channel design to improve air-side contacting in solid oxide cell (SOC) stacks**

Yavuz Selim Ayhan

Schriften des Forschungszentrums Jülich  
Reihe Energie & Umwelt / Energy & Environment

Band / Volume 651

ISSN 1866-1793

ISBN 978-3-95806-797-4

Bibliografische Information der Deutschen Nationalbibliothek.  
Die Deutsche Nationalbibliothek verzeichnet diese Publikation in der  
Deutschen Nationalbibliografie; detaillierte Bibliografische Daten  
sind im Internet über <http://dnb.d-nb.de> abrufbar.

Herausgeber  
und Vertrieb:      Forschungszentrum Jülich GmbH  
                         Zentralbibliothek, Verlag  
                         52425 Jülich  
                         Tel.: +49 2461 61-5368  
                         Fax: +49 2461 61-6103  
                         [zb-publikation@fz-juelich.de](mailto:zb-publikation@fz-juelich.de)  
                         [www.fz-juelich.de/zb](http://www.fz-juelich.de/zb)

Umschlaggestaltung: Grafische Medien, Forschungszentrum Jülich GmbH

Druck:                      Grafische Medien, Forschungszentrum Jülich GmbH

Copyright:              Forschungszentrum Jülich 2024

Schriften des Forschungszentrums Jülich  
Reihe Energie & Umwelt / Energy & Environment, Band / Volume 651

D 82 (Diss. RWTH Aachen University, 2024)

ISSN 1866-1793  
ISBN 978-3-95806-797-4

Vollständig frei verfügbar über das Publikationsportal des Forschungszentrums Jülich (JuSER)  
unter [www.fz-juelich.de/zb/openaccess](http://www.fz-juelich.de/zb/openaccess).



This is an Open Access publication distributed under the terms of the [Creative Commons Attribution License 4.0](https://creativecommons.org/licenses/by/4.0/),  
which permits unrestricted use, distribution, and reproduction in any medium, provided the original work is properly cited.

## Abstract

Energy transition worldwide can be realized with the contribution of promising and advanced technologies such as solid oxide cells (SOCs). Although commercial products are on the market, this ceramic-based technology can still be improved to increase both operating efficiency and lifetime, and reduce the cost of the end product.

Non-optimal air-side contacting in SOC stacks causes performance loss compared to single-cell measurements and may be avoided by a novel design, which is the direct printing of an air-side electrode contact layer in a rib-channel form. This ceramic layer also provides gas distribution, eliminating the need for machined or stamped gas channels on the metallic interconnect. Since the machining/pressing process is costly and time-consuming, printing this ceramic layer with a novel design might be advantageous in terms of performance enhancement and cost-effectiveness in SOC stacks.

To realize the novel idea, stencil printing was used to print ribs from pastes with different recipes and preparation routes. Two different perovskite materials, developed and used in-house, were utilized in the paste preparation. It is observed that changing solid content and binder content by keeping the type of ingredients and the particle size distribution (PSD) within the paste batch the same did not change the rheological behavior. It has been observed that the reason was the lack of a three-dimensional (3D) network within the paste structure which provides structural recovery after the printing. It led to an undesired shape on the printed design because the paste flows and does not retain its printed shape. However, by adding a dispersant and varying the PSD of the powders, the pastes became more controllable, and the influence was directly seen in the shape of printed ribs with sharper edges and flatter surfaces. In addition, rheology results were applied to the printing process to achieve successful printing results, i.e. a delay before separation of the substrate from the stencil was applied according to the time-dependent behavior plot obtained from rheology measurements.

Thus, ribs with a thickness of about 500  $\mu\text{m}$  with an appropriate surface flatness were successfully printed and characterized by electron microscopy, 3D confocal microscopy, and white light topography. As an outlook, the best-performing design, microstructure, and material combination for the rib-channel form will be investigated. In addition, a stack test consisting of cells with this rib-channel design of the cathode contact layer will be performed and evaluated.

## Kurzfassung

Die weltweite Energiewende kann durch den Beitrag vielversprechender und fortschrittlicher Technologien wie Festoxidzellen (SOC) verwirklicht werden. Obwohl bereits kommerzielle Produkte auf dem Markt sind, kann diese auf Keramik basierende Technologie noch verbessert werden, um sowohl die Betriebseffizienz als auch die Lebensdauer zu erhöhen und die Kosten des Endprodukts zu senken.

Eine nicht optimale luftseitige Kontaktierung in SOC-Stacks führt zu Leistungseinbußen im Vergleich zu Einzelzellenmessungen und kann durch ein neuartiges Design vermieden werden, nämlich das direkte Drucken einer luftseitigen Elektrodenkontaktschicht in Form eines Stegs und Kanals. Diese keramische Schicht sorgt auch für die Gasverteilung und macht maschinell bearbeitete oder gestanzte Gaskanäle auf der metallischen Verbindung überflüssig. Da der Bearbeitungs-/Pressprozess kostspielig und zeitaufwändig ist, könnte das Drucken dieser Keramikschicht mit einem neuartigen Design in Bezug auf die Leistungssteigerung und Kosteneffizienz in SOC-Stacks von Vorteil sein.

Um die neuartige Idee zu verwirklichen, wurden mit Hilfe des Schablonendrucks Stege aus Pasten mit unterschiedlichen Rezepturen und Herstellungswegen gedruckt. Bei der Herstellung der Pasten wurden zwei verschiedene Perowskit-Materialien verwendet, die im eigenen Haus entwickelt und eingesetzt wurden. Es wurde festgestellt, dass eine Änderung des Feststoff- und Bindemittelgehalts bei gleichbleibender Art der Inhaltsstoffe und der Partikelgrößenverteilung (PSD) innerhalb der Pasten-Charge keine Änderung des rheologischen Verhaltens bewirkte. Es wurde festgestellt, dass der Grund dafür das Fehlen eines dreidimensionalen (3D) Netzwerks innerhalb der Pasten-Struktur war, das für eine strukturelle Erholung nach dem Druck sorgt. Dies führte zu einer unerwünschten Form des gedruckten Designs, da die Paste fließt und ihre gedruckte Form nicht beibehält. Durch die Zugabe eines Dispergiermittels und die Variation der PSD der Pulver wurden die Pasten jedoch kontrollierbarer, und der Einfluss zeigte sich direkt in der Form der gedruckten Stege mit schärferen Kanten und flacheren Oberflächen. Darüber hinaus wurden die rheologischen Ergebnisse auf den Druckprozess angewandt, um erfolgreiche Druckergebnisse zu erzielen, d. h. es wurde eine Verzögerung der Trennung des Substrats von der Schablone entsprechend dem aus den rheologischen Messungen gewonnenen zeitabhängigen Verhaltensdiagramm angewandt.

Auf diese Weise wurden Stege mit einer Dicke von etwa 500  $\mu\text{m}$  und einer angemessenen Oberflächenebenheit erfolgreich gedruckt und durch Elektronenmikroskopie, konfokale 3D-Mikroskopie und Weißlichttopografie charakterisiert. Darüber hinaus zielt diese Arbeit darauf ab, einen Ausblick auf das beste Design, die beste Mikrostruktur und die beste Materialkombination für die Steg-Kanal-Form zu geben. Außerdem soll in Zukunft als abschließende Charakterisierung ein Stack-Test bestehend aus Zellen mit diesem neuartigen Steg-Kanal-Design der Kathodenkontaktschicht durchgeführt werden.

## Table of contents

Abstract .....	1
Kurzfassung.....	2
Table of contents .....	3
1. Introduction .....	6
2. Literature research .....	9
2.1. Importance of hydrogen technology.....	9
2.2. Solid oxide cells (SOCs).....	10
2.2.1. Electrolyte .....	11
2.2.2. Anode.....	13
2.2.3. Cathode.....	14
2.2.4. Interconnect.....	14
2.2.5. Contacting in SOC stacks .....	15
2.2.6. Glass sealants .....	16
2.3. SOC cell types and production methods .....	16
2.4. Stencil printing .....	19
2.4.1. Stencil printing in the field of ceramics .....	19
2.4.2. Use of stencil printing in different fields .....	21
2.5. Four-point probe measurements .....	22
3. Materials and Methods.....	23
3.1. Used perovskites .....	23
3.1.1. LCC2 .....	23
3.1.2. LSCF.....	23
3.2. Substrates .....	23
3.3. Printing process .....	24
3.4. Characterization methods.....	25
3.4.1. Particle size distribution .....	25
3.4.2. Surface area analysis.....	25
3.4.3. Rheological analysis .....	25
3.4.4. Scanning electron microscopy (SEM) with energy-dispersive X-ray spectroscopy (EDS) .....	26



3.4.5. Confocal laser microscopy.....	26
3.4.6. White light topography.....	27
3.4.7. Four-point probe (4PP) measurements.....	27
4. Stencil printing of LCC2 .....	28
4.1. Capital introduction .....	28
4.2. Experimental part .....	29
4.2.1. Material.....	29
4.2.2. Paste compositions and preparation routes .....	30
4.2.3. Stencil printing experiment and process parameters .....	31
4.2.4. Characterization of the pastes and printed ribs .....	33
4.3. Results & Discussion .....	33
4.3.1. Process parameters in stencil printing .....	33
4.3.2. Influence of Different Paste Formulations on the Printing Experience with Rheological Aspects .....	34
4.3.3. Influence of varied stencil printing parameters on the printing experience .....	38
4.3.4. Investigation of the revised paste recipe with revised printing parameters – Paste P6 and Print B .....	40
4.4. Chapter conclusion .....	42
5. Stencil printing of LSCF.....	43
5.1. Capital introduction .....	43
5.2. Experimental part .....	44
5.2.1. Material.....	44
5.2.2. Paste compositions and preparation routes .....	45
5.2.3. Stencil printing experiment and process parameters .....	47
5.2.4. Characterization of the pastes and printed ribs .....	49
5.3. Results & Discussion .....	49
5.3.1. Achievement of the desired printing results .....	49
5.3.2. Characterization of the printed ribs from Paste X3v2 .....	50
5.3.3. Study of the rheology for paste X3v2 .....	52
5.3.4. Effect of dispersant and PSD on paste behavior with respect to printing results .....	54
5.3.5. Mono- and poly-modal PSD effect on the paste behavior with respect to printing results ....	57
5.3.6. Printing of different rib-channel designs.....	59
5.3.7. Study of printing parameters .....	60
5.3.8. Reproducibility of paste X3v2 with desired printing results.....	60

5.3.9. Reproducibility attempt with old paste.....	62
5.4. Chapter conclusion .....	64
6. Evaluation of the novel idea .....	65
6.1. Novel idea: How much is it going to contribute to the stack resistance? .....	65
6.2. Rib-channel design: What are the best rib-channel widths? .....	65
6.3. Four-point probe (4PP) measurements.....	66
6.4. Cell assembly.....	67
Summary.....	69
Outlook .....	70
List of abbreviations.....	71
References .....	73
Index of Figures.....	79
Index of Tables.....	81
Acknowledgments .....	82

## 1. Introduction

Global warming warns us to take action for a safe and sustainable world, not only for now, but also for the future. Most recently, the Paris Agreement as a global one and national policies of several countries have come up with the goal of decarbonizing all sectors as much as possible. As the world's energy needs are mainly met by fossil fuels, researchers have been developing new methods to generate electricity efficiently and with no or less harmful gas emissions, such as fuel cells, which convert chemical energy into electrical energy through electrochemical reactions. One of the well-known types is the solid oxide fuel cell, which can also be used for water splitting to produce hydrogen.

Solid oxide cell (SOC) technology represents an eminent potential for the energy transition with its flexibility in reversible use (in fuel cell mode as a solid oxide fuel cell and in electrolysis mode as a solid oxide electrolysis cell) [1,2]. Besides this and many other advantages, the technology requires some improvements to lower the cost and to increase the performance with a longer lifetime to be competitive in the market [3–5]. Related to the cost issue, a study in the literature highlighted that the machinery cost for interconnect (IC) with the cost of other metal parts such as frames, end plates, and nickel mesh dominates the CAPEX (Capital Expenditures) for a stack system in Jülich (FIII20) [6]. The latter study also mentioned the case of a 50% reduced power density due to the loss of contact area between the IC and the cell's anode and the cathode. Several other groups also agree that the contact resistance between cells and interconnects should be reduced [7–9] to ensure high performing repeat unit resulting in higher stack performance. Thus, it is obvious that the cost reduction with a performance increase in a stack system will accelerate the market establishment of this technology faster.

In the structure of the Jülich stationary stacks, the contact on the fuel electrode side is provided by nickel mesh, which is performing well. However, a machining process is used to grind the gas channels on the air-side metal interconnect, which is costly and time-consuming. Moreover, the contact between the air-side interconnect and the cell is not ideal for adequate electron transport, as shown in the SEM (Scanning Electron Microscopy) images in Figure 1-a. An alternative design (see Figure 1-b) that eliminates these issues may be advantageous at this point. This is the idea of printing a ceramic structure with gas channels directly on the cell has been established in Jülich. A ceramic layer with a rib-channel design can provide a sufficient gas supply with an appropriate contact from its top surface to the metal interconnect. The fabrication of this three-dimensional and ca. 500  $\mu\text{m}$  thick ceramic layer with rib-channel design is the aim of this work.

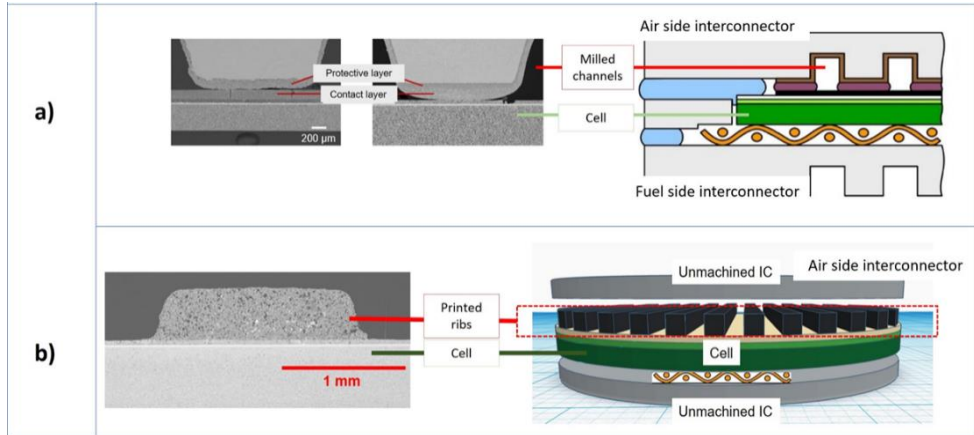


Figure 1 a) SEM images showing actual non-ideal contact between the interconnect and the cell with a schematic illustration of a single repeat unit, b) SEM image of newly stencil printed layer with improved surface flatness coupled with the schematic illustration of a novel design in a single repeat unit of a stack

According to the manufacturing routes followed in SOCs, the screen printing method plays a vital role due to its low cost and ability for mass production [10,11]. However, this technique is mostly used for layers with a thickness up to 100 μm [11,12]. For thicker layers with specific geometries, stencil printing could be an alternative if high aspect ratios on printed shapes can be achieved [12]. It is a stencil-using version of screen-printing and the thickness of the stencil can be varied with the aperture design for the applications. It is popular in the micro-electronics field, where area array packages such as flip chips have been manufactured by this method using solder pastes [13–15]. However, it is not a well-known method in the ceramic field as only a few studies can be found in the literature [16,17]. Nevertheless, for simple three-dimensional (3D) geometries of ceramic layers, stencil printing could be a promising manufacturing technique in terms of cost-effectiveness and faster production. Therefore, this method was used in this study with the consideration of the influence of process parameters, paste recipes, and rheological behaviors of the pastes on the printing result.

Printing experience and results with stencil printing include: printability of the paste without printing failures such as stencil clogging; suitable paste characteristics for the desired geometry related to the paste formulation and preparation; suitable printing parameters to control/assist the printing process concerning the printing shape. The paste structure that is ruptured by applied shear should recover itself to maintain the printed shape that can be influenced by paste formulations. The stencil printing parameters should be set appropriately to be sure that the paste will be printed well and that it is compatible with the rheological characteristic of the paste. This cannot be known exactly without trying, as the influence of the parameters on the printing experience can vary from paste to paste. However, oscillatory step test measurements demonstrate the printing process, which can be very helpful in predicting printing results. Therefore, an evaluation of the rheological results is an asset to achieve successful printing results.

Overall, different types of pastes have been prepared, characterized, and printed in this PhD thesis. Chapter 4 and Chapter 5 cover many details about LCC2 and LSCF containing pastes, respectively, and their characterization with printing results. For the characterization of the pastes and prints, various instruments such as rheometry, electron microscopy, white light topography, etc. were utilized which are discussed in Chapter 3. According to the characterization results, it has been seen that adequate printing results were achieved via the printing of the LSCF-containing paste to reach good performance in an SOC stack. The novel design was briefly/roughly evaluated to demonstrate its suitability for cell assembly through conductivity and pressure drop calculations as well as a mechanical test in Chapter 6. On the other hand, the basics of SOC technology, including system parts, fabrication routes, etc., were presented in Chapter 2 on the way from cell fabrication to the cell assembly.

## 2. Literature research

### 2.1. Importance of hydrogen technology

The world's population is growing and consumption is increasing. It is predicted that the population will be approx. 9 billion and global energy consumption will increase by 77% by 2050 [18]. Fossil fuels are still used as the major feedstock for global energy supply with some disadvantages [19]. The non-homogeneous distribution and the limited nature of fossil fuels lead to political uncertainties between countries, which may limit the accessibility to this feedstock. On the other hand, CO<sub>2</sub>-related emissions from fossil fuels contribute to global warming, which causes climate change [19,20]. Therefore, environmentally friendly alternatives such as renewable energy sources (i.e. wind and solar) are necessary and can be used to harvest electricity, although these alternatives are occasionally related to environmental conditions. It can be overcome with storage of the obtained energy that will prevent the intermittent nature of the renewable energy [20]. Hydrogen, methane, methanol, or dimethyl ether is the form for the storage and Ebbesen et al. mentioned that hydrogen is the most environmentally friendly and efficient fuel [20]. Another paper emphasized that hydrogen as an energy carrier can be used as a storage medium [21]. There is now a global movement by several countries for the production and consumption of hydrogen to contribute to the decarbonization goals related to the Paris Agreement [22,23].

Although today most hydrogen is produced by steam reforming of natural gas due to the higher efficiencies (60-85%) [19–21], emission-free (green) hydrogen production is needed to contribute to the energy transition [24]. It is important to note that the way how hydrogen is produced is color-coded. If hydrogen is produced by burning natural gas at higher temperatures, it is called gray hydrogen. If its CO<sub>2</sub> emission is removed or captured, it is called blue hydrogen. Without any emission in the production (i.e. water/steam electrolysis by using electricity from renewable sources), the hydrogen becomes green hydrogen [23].

Hydrogen, one of the most abundant elements in the universe, can be used in its green form to support a circular and green economy worldwide. There are various production methods to obtain hydrogen, such as biological processes, photochemical processes, etc., but the high purity one can be obtained by water electrolysis which is currently the most basic industrial process [19].

There are several types of technologies in use for electrolysis and/or electricity generation such as polymer electrolyte fuel cells and electrolyzers (PEFCs, PEECs), alkaline fuel cells and electrolyzers, phosphoric acid fuel cells (PAFCs), molten carbonate fuel cells (MCFCs) and solid oxide fuel cells and electrolyzers [25]. The latter are those that can be used reversibly in a single unit for both electricity generation in fuel cell mode and H<sub>2</sub> production in electrolysis mode. In electrolysis mode, it is also capable of co-electrolyzing H<sub>2</sub>O and CO<sub>2</sub>, resulting in a synthetic gas (H<sub>2</sub> and CO) that can later be converted into various fuels such as methane, methanol, and dimethyl ether [20]. If the required electricity for SOEC is obtained from renewable energy sources, CO and H<sub>2</sub> will be further used in the chemical industry as green feedstock, while synthetic fuels will be beneficial in the transportation sector to make it green.

## 2.2. Solid oxide cells (SOCs)

A basic definition for solid oxide cells is that they can convert chemical energy into electrical energy or vice versa. This means that an SOC as a unit is reversible and is abbreviated as rSOC. The fuel cell mode of the system (Solid Oxide Fuel Cell) can be used for electricity production, and the electrolysis mode (Solid Oxide Electrolysis Cell) can be used not only for hydrogen production, but also for synthesis gas production [3,25].

A single solid oxide cell consists of an oxygen electrode and a fuel electrode separated by an electrolyte. The basic working principle of rSOCs, which are defined as solid oxide electrolysis and fuel cells (SOEC & SOFC, respectively), can be seen in Figure 2 with the electrochemical reactions. Electrolysis of water, CO<sub>2</sub>, or both is possible via SOECs resulting in the production of hydrogen (H<sub>2</sub>), carbon monoxide (CO), or syngas (H<sub>2</sub>+CO), respectively. The solid oxide fuel cell converts chemical energy into electricity. Figure 2 shows only H<sub>2</sub> and CO as fuels, but the system is fuel flexible and can even run on fossil fuels such as natural gas, to generate electricity.

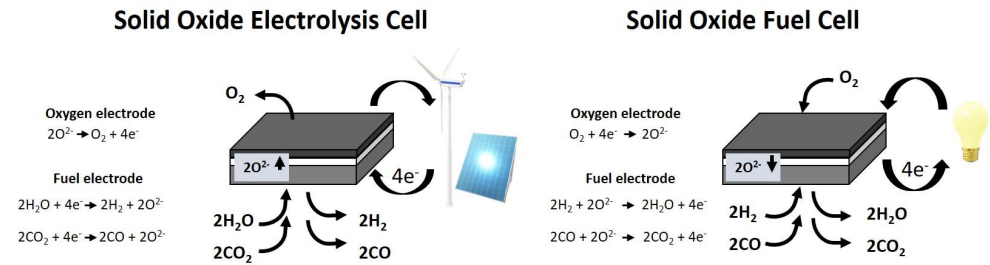


Figure 2 Schematic illustration of the working principles of solid oxide electrolysis cells (left) and solid oxide fuel cells (right)

For a detailed explanation of the electrochemical phenomena, the SOFC system for electricity generation by using hydrogen as a fuel works as follows:

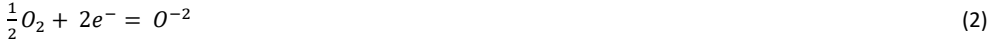
- Fuel as a gas from the fuel electrode side (anode) and
- Air (oxygen) from the air/oxygen electrode side (cathode) are purged at high temperatures (650 - 1000 °C).
- The open circuit voltage is generated obeying the Nernst equation. (Equation 1)

$$E = E_0 + \frac{RT}{nF} \left( \frac{P_{\text{H}_2} P_{\text{O}_2}^{\frac{1}{2}}}{P_{\text{H}_2\text{O}}} \right) \quad (1)$$

where E is the generated open circuit potential, E<sub>0</sub> is the standard potential, R is the ideal gas constant, n is the number of electrons, F is the Faraday constant, and P is the partial pressure of the relevant gases, i.e. H<sub>2</sub> and O<sub>2</sub>.

- The obtained voltage is converted into electrical work by closing the circuit of the system and then the current is drawn.

As the system operates, the oxygen gas is reduced to oxygen ions at the cathode (equation 2) and then transported through the electrolyte, which is an ionic conductor, to the anode side, where a reaction of hydrogen and oxygen ions occurs to produce water vapor and electrons (equation 3). This completes the circuit.



On the other hand, there are some losses in the cell as voltage drops during the current flow due to different types of kinetic losses such as activation losses, ohmic losses, and mass transfer losses, which are also demonstrated in Figure 3. Activation losses are dominant at low currents and associated with the rates at the electrochemical reactions at electrodes. Ohmic losses are due to the resistance in ion transport and, according to some papers also due to contact resistance in stack operation [7,9]. Mass-transfer losses, also called concentration polarization, occur due to the limited transport of reactant gases to the electrochemically active sites in the cell [26].

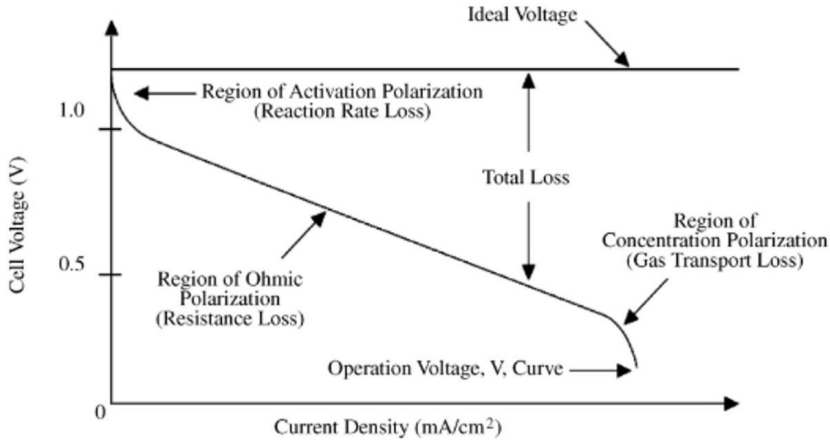


Figure 3 I-V curve for the ideal and actual performance of a fuel cell [26]

### 2.2.1. Electrolyte

There are several requirements for an electrolyte; good conductivity of ions or protons, gas tightness, chemical stability, and no electron conduction. Depending on the electrolyte type and temperature, cells and electrolyzers are referred to as polymer electrolyte cells, alkaline cells, phosphoric acid cells, molten carbonate cells, and solid oxide cells [25]. While a proton-conducting fuel and electrolysis cell, which is a



variant of a solid oxide cell, requires proton conduction on the electrolyte, a solid oxide fuel and electrolysis cell requires oxygen ion transport. Electrolytes should not also conduct electrons, which would cause a short circuit in the cell system.

More specifically, the oxygen ion conductivity is a function of the oxygen diffusion coefficient, which is a thermally activated process as described in the Nernst-Einstein relation in Equation 4.

$$\sigma_i T = z_i e c_i u_i T = (z_i e)^2 c_i B_i T = \frac{(z_i e)^2 c_i}{k} D_i = \frac{(z_i e)^2 c_i}{k} D_{i,0} \exp^{-\frac{\Delta H_m}{kT}} \quad (4)$$

where  $\sigma$  is the conductivity,  $T$  is the absolute temperature (in kelvin (K)),  $z$  is the valence,  $e$  is the electronic charge,  $c$  is the number of charged particles (concentration) per unit volume,  $u$  is the jump distance,  $\beta$  is the particle mobility,  $k$  is the Boltzmann constant,  $D$  is the diffusion coefficient,  $\Delta H_m$  is the enthalpy change.

However, Equation 4 can be rewritten in a simpler form (Equation 5) by defining all of the pre-exponential parameters as a single factor of  $A$ , and the new equation looks as follows;

$$\sigma T = A \exp(-EA / kT) \quad (5)$$

The relationship between temperature and conductivity can be seen in Figure 4, which shows the temperature dependence of several electrolyte conductivities in the Arrhenius plot. Yttria-stabilized zirconia (YSZ) is a typical electrolyte material in SOCs [27]. It has variants such as 3YSZ (with 3 mol% yttria) and 8YSZ (with 8 mol% yttria). Depending on the design of the cell: the former is the commonly used electrolyte for electrolyte supported cells (ESC), while the latter is mostly used in fuel electrode supported (FESC) or metal supported cells (MSC). YSZ shows good mechanical strength and is cheaper than some other electrolytes such as ScCeSZ (zirconia co-stabilized with scandia and ceria) [25]. However, the trend today is to lower the operating temperature of SOCs (<600 °C). Therefore, several other options show higher ionic conductivity such as  $\text{Bi}_2\text{O}_3$ . Ayhan et al. [28] mentioned the advantage of bismuth oxide ( $\text{Bi}_2\text{O}_3$ ) based electrolytes in terms of higher ionic conductivity due to the more oxygen vacancies in the sub-lattice compared to other ionic conductors, i.e. zirconia or ceria but the limitation with  $\text{Bi}_2\text{O}_3$  was the phase stability, although it was doped with yttria in that study. Alternatively, the design parameters of the SOC layers can be varied, i.e. a thin layer of YSZ can be used in the cell to minimize the ohmic resistances due to its low ionic conductivity. Thus, electrode-supported cells can be used instead of electrolyte-supported cells in which the electrolytes are relatively thick (80 -150  $\mu\text{m}$ ) [25].

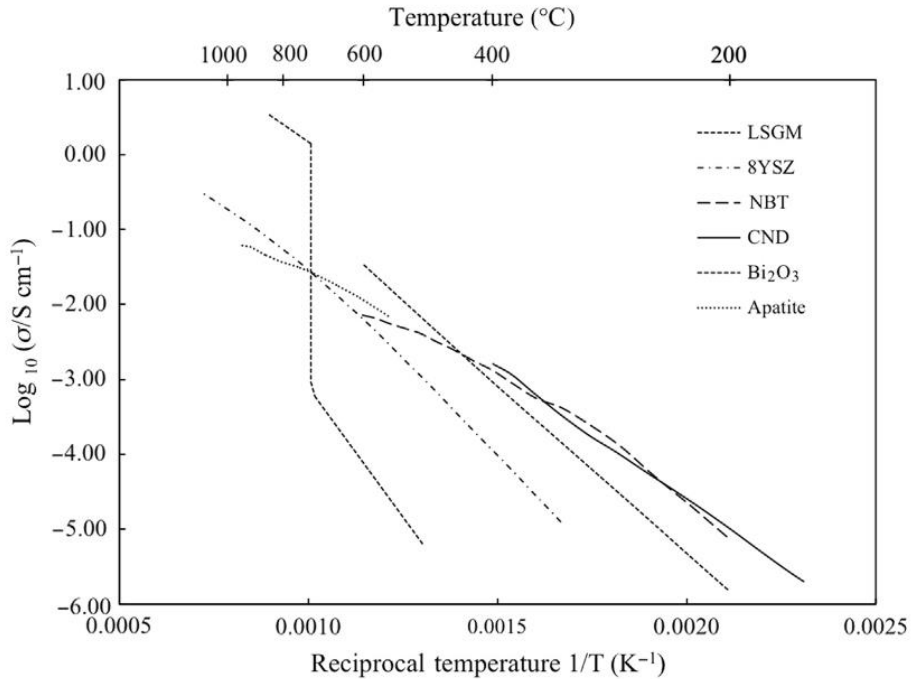


Figure 4 Conductivity of oxygen ion conductors at different temperatures.  $\text{La}_{0.8}\text{Sr}_{0.2}\text{Ga}_{0.9}\text{Mg}_{0.1}\text{O}_{3-6}$  (LSGM),  $\text{Zr}_{0.84}\text{Y}_{0.16}\text{O}_{1.92}$  (8YSZ),  $\text{Na}_{0.5}\text{Bi}_{0.49}\text{Ti}_{0.98}\text{Mg}_{0.02}\text{O}_3$  (NBT),  $\text{Ce}_{0.9}\text{Nd}_{0.1}\text{O}_{1.95}$  (CND),  $\text{Bi}_2\text{O}_3$  and  $\text{La}_{10}\text{Si}_{5.8}\text{Mg}_{0.3}\text{O}_{26.8}$  (Apatite) [29]

### 2.2.2. Anode

The fuel electrode needs to fulfill the requirements of porous structure for gas diffusion, electronic and ionic conductivity, and chemical stability. Triple phase boundaries where ion conduction, electron conduction, and pores meet should be well distributed to maximize the anodic reactions. The coefficient of thermal expansion (CTE) should also be well-matched to the adjacent electrolyte layer to prevent delamination.

Fuel electrode-supported cells (FESCs) have been used in Jülich for more than 20 years now [30]. The Ni/8YSZ support layer is 250-500  $\mu\text{m}$  thick with a coarse microstructure. The anode layer is fine-grained in a thickness of about 10  $\mu\text{m}$  and is made of Ni/8YSZ just like the support, which is tape cast, and the rest (an electrolyte ( $d \sim 10 \mu\text{m}$ ), barrier layer of GDC ( $d \sim 5 \mu\text{m}$ ), and air electrode ( $d \sim 50 \mu\text{m}$ )) is screen printed, which is the typical production method [25].

Nickel/YSZ cermet is often used as the anode material but there are several degradation issues. Nickel particles undergo coarsening yielding a loss of triple-phase boundaries [31]. In the operation of SOCs with hydrocarbon fuels, carbon deposition [32] or sulfur poisoning [33] in these Ni-containing anodes leads to

a loss of performance. There have been several studies to overcome this by using e.g. Ni/GDC [34] or Ni/ScYSZ [33] based anodes to tolerate the degradation issues with carbon and sulfur, respectively.

### 2.2.3. Cathode

Similar to fuel electrodes, air electrode also needs a porous structure for air diffusion, electrical and ionic conductivity, and chemical stability. In addition, good catalytic activity for oxygen splitting in SOFC modus and for the recombination of  $O^{2-}$  ions in SOEC modus are also required [25]. Depending on the design of the SOC, the CTE should be well matched with adjacent layers for compatibility.

Ceramic-based mixed ionic and electronic conducting (MIEC) perovskites are typically used as air electrodes.  $ABO_3$  is the chemical structure of perovskites, and LSCF (La, Sr, Co, Fe) with LSC (La, Sr, Co) are examples for the well-known MIEC perovskite materials for air electrodes air electrode [25,27,29,35]. Additional to this, LSM, which is almost pure electron conductor, has been used coupling with i.e. YSZ as an air electrode [29]. Sick et. al compared the conductivity values of these three perovskites as shown in Table 1. LSC has the highest conductivity value but compatibility with other components may be an issue, especially during thermal cycling. Its ionic conductivity is lower than that of LSCF [36] but it is not a limiting factor for its use as a cathode material at lower temperatures (600 - 800 °C) as well as LSCF. On the other hand, compared to LSM, LSCF is more prone to Sr segregation or to poisoning by impurities (sulfur, silicon) than LSM for the degradation point of view [37,38], but LSCF is still advantages for using in SOC because of its higher power density, which is also studied in the literature [39].

In addition, a protective layer of gadolinium-doped ceria (GDC) is applied between the YSZ electrolyte and the LSCF [40,41] and LSC [42] cathodes to slow down/prevent the degradation.

Table 1 Properties of some SOC materials [35]

Layer	Name	$\sigma_e$ / $S\text{cm}^{-1}$ at 800°C	TEC / $10^{-6}\text{K}^{-1}$ for 30-800°C
Interconnector	Crofer22APU	8700 <sup>10</sup>	11.9 <sup>10</sup>
Protective coating	MCF	26-30 <sup>21</sup>	~13 <sup>21, 22</sup>
Protective coating	MnOx	0.1 <sup>49</sup>	8.8 <sup>49</sup>
Contact layer	LSMC	~180 <sup>38</sup>	12-16 <sup>27, 38</sup> (30-1000°C)
Contact layer	LCC10	~80 <sup>46</sup>	~14 <sup>46</sup>
Contact layer, Cathode	LSCF	100-200 <sup>37, 38</sup>	13-16 <sup>37, 38</sup> (30-1000°C)
Cathode	LSC	>1220 <sup>38</sup>	19 <sup>38</sup> (30-1000°C)
Cathode	LSM	~160 <sup>38</sup>	11-12.4 <sup>27, 38</sup> (30-1000°C)

### 2.2.4. Interconnect

Cell assembly is required to increase the energy output of cells. It creates single repeat units (SRU) as shown in Figure 5, and connectors are needed with several requirements in the name of interconnects or

bipolar plates. They are used to connect the SRUs electronically, to separate the gas chambers, and to distribute the gas streams [25].

Stainless steel interconnects such as Crofer 22 APU or Crofer 22 H are used industrially and consist of a high chromium content (20 - 26 wt% Cr). In particular, manganese (Mn) is also added to form a double-layer oxide scale during operation, which is the Cr-Mn spinel layer on the top of a  $\text{Cr}_2\text{O}_3$ -rich scale [7,25]. This naturally formed chromium scale is useful in protecting the interconnect from corrosion and oxidation at elevated temperatures. Another advantage of metallic interconnects over ceramic-based ones is higher conductivity values [43]. However, volatile chromium species poison the cathode contact layer or cathode, causing degradation via the formation of detrimental  $\text{SrCrO}_4$  crystallites [44,45]. To prevent this, e.g. MCF layer  $(\text{Mn},\text{Co},\text{Fe})_3\text{O}_4$  is applied as a protective layer by atmospheric plasma-spraying [46,47].

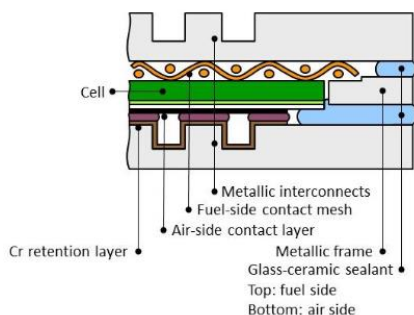


Figure 5 Cross-sectional schematic of a single repeat unit for SOCs

### 2.2.5. Contacting in SOC stacks

The assembly of multiple repeat units forms a "stack". Interconnects have been used in a stack system (for the reason explained above) and contact elements are necessary to provide better electrical and mechanical contact between the SOC cathode and the interconnect [7,25]. On the fuel electrode side, Ni mesh is used which provides good gas permeability and compensates for manufacturing tolerances. It also avoids the machining process on the fuel side interconnect to form gas channels as it provides the gas distribution. On the air electrode side, Ni mesh cannot be used due to oxidation issues. K. Sick et al. found in their study that a coarse-structured LSCF layer on top of a fine-structured LSCF cathode is the most suitable contact for the Jülich SOC stacks [35].

According to N. K. Karri et al., the contact between the cathode and the interconnect has been identified as the weakest link in the present SOCs [48] which also means the main source of ohmic resistance in the fuel electrode-supported cell stacks. In the same direction, C. Lenser et al. [7] mentioned the contribution of the contact resistance to the cell impedance at different temperatures compared to other elements such as electrolyte, cathode, and anode as shown in Figure 6. The priority of any improvement in the

contact part for better performance of SOC stacks has been highlighted in the literature not only in the latter study but also in the study by R. Spotorno et al. [9].

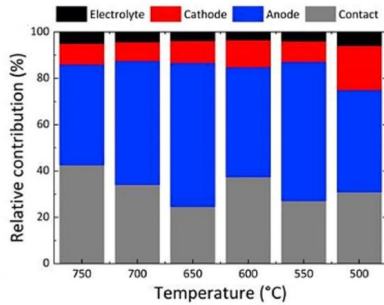


Figure 6 Relative contribution of SOC elements on the cell impedance within a stack at different temperatures [7]

#### 2.2.6. Glass sealants

There is another element that is used in the cell assembly in a stack, which is the glass sealant. Gas tightness in the cell design is provided by an electrolyte and in the stack system by glass sealants. The edges of the cells are sealed to the metal frame and the fuel gas compartments are sealed to the outside. Good adhesion to metallic and ceramic surfaces, gas tightness, robustness, and stability under reduction and oxidation are fundamental requirements for glass sealants.

There are several types of sealants such as glass, glass-ceramic, metal, and composite sealants [49]. A glass-ceramic sealant was used in Jülich with two different methods;

- First, screen printing of a sealant directly to the stack parts
- Second, the sealant is applied to a foil and dried to be placed separately in a stack

The second method allows decoupling of the sealant production from the stack manufacturing, simplifies the process, and enables storage of the sealant for later use and was developed by Forschungszentrum Jülich [50].

### 2.3. SOC cell types and production methods

Several types of cells differ in their mechanical support layers. This is how their names are defined, such as electrode-supported cells when the anode or cathode layer is used as a support with a thicker layer than other layers. For the sake of simplicity, the cell types were named based on solid oxide fuel cells. There is no anode-supported cell (ASC) but fuel electrode-supported cell (FESC) in SOC stacks because anode-

supported cell in SOFC is cathode supported cell in SOEC. So, the types of the cells are shown schematically in Figure 7 in the PhD thesis of F. Grimm [51].

ASCs were developed in Jülich as an alternative to the electrolyte-supported cell (ESC) design for two basic reasons:

- To reduce the ohmic resistance by using a much thinner electrolyte
- Hence, to reduce the operating temperature

Lowering the operating temperature gives more possibilities that limited high-temperature resistant materials will not be the only choice in cell manufacturing [30]. However, ESCs are among the most mature SOC technologies mentioned in the literature and the issue of higher ohmic resistances due to thick electrolytes can be overcome by operating the SOC system at higher temperatures to decrease the area-specific resistance (ASR) [52]. Another cell type that was developed by Bosch is an inert-supported cell to reduce manufacturing costs and increase the marketability of the system [53]. In addition, metal-supported cells (MSC) have attracted interest due to their low cost and being advantageous in manufacturing [54]. Thin-film technologies such as PVD, electrophoretic deposition, and sputtering are used to coat cell layers on the porous metallic support. High sintering temperatures for coating are not required [25] and higher power densities have been targeted with this cell design [55].

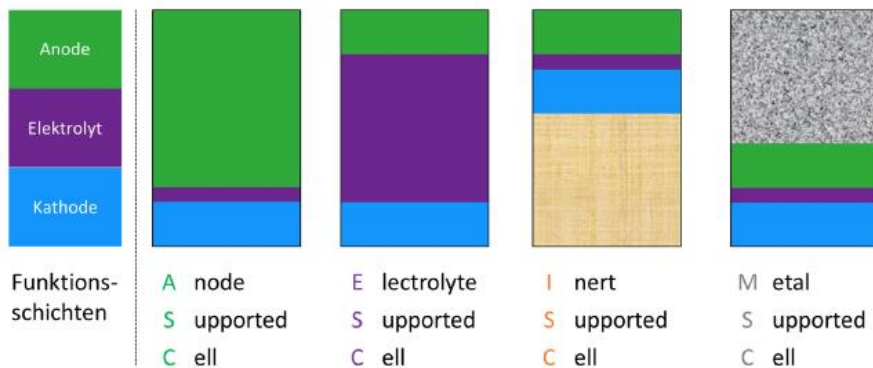


Figure 7 Schematic representation of SOFC cell types. Green, purple, and blue stand for functional layers of anode, electrolyte, and cathode, respectively [51]

Back to the ASCs in Jülich, warm pressing was used to produce the supports and anode and electrolyte were applied via vacuum slip casting. Subsequently, tape casting was used in combination with screen printing to produce cell layers [56]. The tape casting process is shown in Figure 8 where a slurry is placed in the reservoir of a doctor blade. The latter moves and casts the slurry to produce a ceramic tape. Depending on the setup, a drying chamber can be adapted. This technique can also be used for sequential casting to minimize sintering steps as Menzler et al. highlighted the possibility of sequential tape casting

of a half-cell fabricated green-on-green (electrolyte + fuel active layer + fuel electrode support) with only one-time sintering at the end [57].

Screen printing is demonstrated in Figure 9, where the slurry is printed onto a substrate by squeegee movement over a screen and pressing the paste through the screen openings. In the typical fabrication route of SOFCs in Jülich, the anode support is fabricated first and then the rest of the layers are printed by screen printing. One of the advantages of screen printing is that no cuts are made after printing, which reduces material loss [6].

For both of the above techniques, slurry preparation is critical and should be coupled with rheological characterization. With an appropriate slurry/paste, a screen printing method can enable three-dimensional (3D) fabrication [12] which will be discussed later.

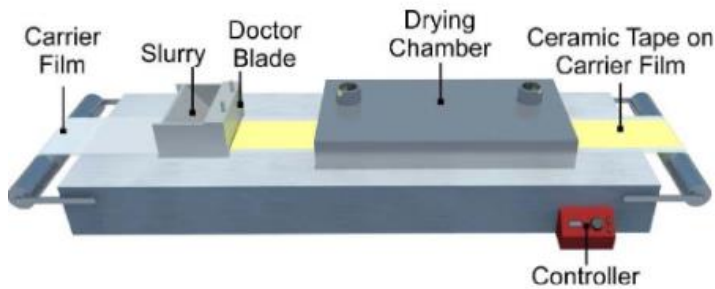


Figure 8 Typical illustration of a tape casting setup [58]

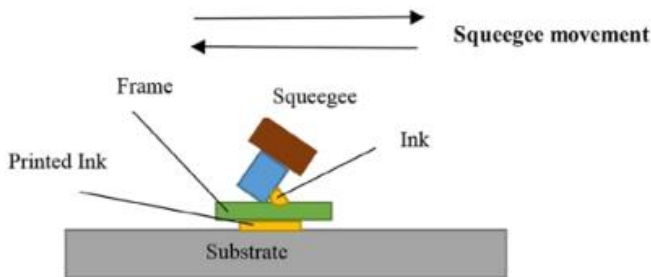


Figure 9 Schematic illustration of screen printing [59]

## 2.4. Stencil printing

Stencil is the name of a sheet made of any material that has apertures of any size, and it is mostly made of silicon, polymers, or metal, which varies depending on the application. Patterning by deposition or printing by using paste through a stencil can both ultimately give similar results in the sense of having a geometry/height on a substrate in different fields/applications.

Stencil lithography as a nanofabrication method, in which the modification of a substrate surface by i.e. deposition or ion implantation of functional materials through a stencil is based on the principle of shadow masking, aims at surface patterning in the submicron range [60,61]. For instance, in the work of Barnabe et al. [62], shown in Figure 10, this method was used to deposit ZnO structures on ultrathin (10 nm) SiO<sub>2</sub> substrates. Similarly, in this work, a 3D geometry was to be printed on a substrate using stencil printing on a mm scale.

Stencil printing differs slightly from screen printing in that a stencil is used instead of a screen and the utilized pastes have different rheology. In this method, a stencil with desired apertures/openings is placed on the substrate. A squeegee moves and prints the paste through the stencil onto the substrate, which could be a rough explanation without detailed process parameters. The scope of applying stencil printing could be to reduce the complexity of manufacturing in terms of printing wafer-sized electronic parts, or in some cases, to have a thicker and more complex printed shape on a substrate rather than applying only a thin layer by screen printing. Studnitzky et al. [12] have mentioned that the stencil-printed parts can reach 0.2 mm or more, while 5-100  $\mu\text{m}$  can be taken as a typical thickness for screen-printed layers. 0.5 mm thick prints with desired properties are the aim of this work, therefore the stencil printing method should be well understood through literature research so that the latest developments can be evaluated in terms of the highest thickness reached so far, the way the characterization of the pastes works or the discovery of the process parameters how they influence the quality of the printed parts, etc.

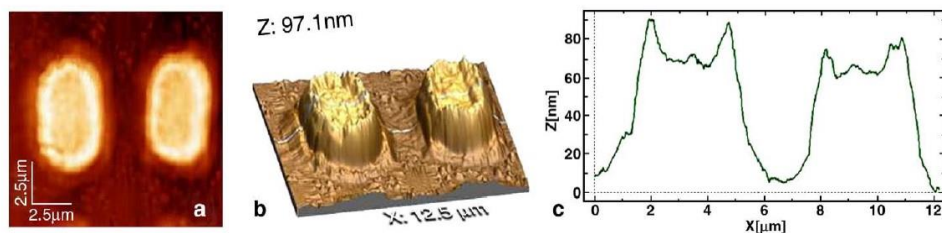


Figure 10 (a) 2D view of ZnO patterns deposited by stencil lithography; (b) 3D profile of the same patterns; (c) thickness of these two ZnO profiles [62]

### 2.4.1. Stencil printing in the field of ceramics

Stencil printing is not as well-known as tape casting and screen printing in the field of ceramics, but there are a few studies using this technique.



The use of stencil printing in the fabrication of SOCs was only mentioned in one study [16], where the NiO-GDC anode layer was printed by screen and stencil printing on an 80% porous and 2 mm thick metal foam. In the first step, stencil printing was utilized to obtain a flat surface on the porous foam to facilitate the application of the screen-printed layers. The SEM image of the printed and sintered foam with the fabrication route schematically shown can be seen in Figure 11. The flow behavior was studied for two different inks with different viscosities for each printing process. Stencil printing on foam sounds like an infiltration but the thicker paste, the one used for stencil printing, stopped flowing and stayed at one point in the foam so that flatness was achieved on the top of the foam.

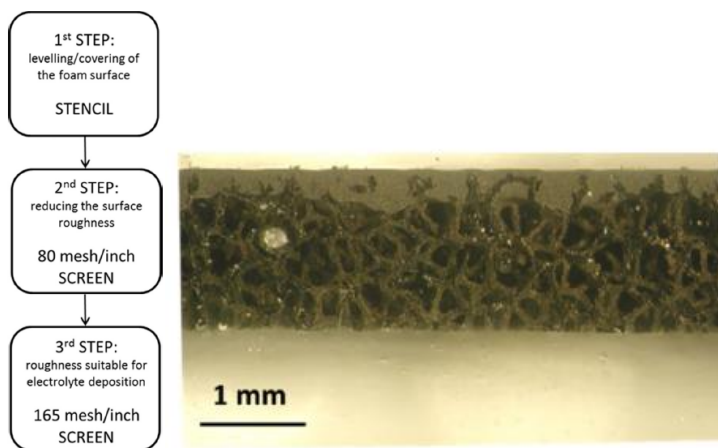


Figure 11 (left) Flowchart of the deposition steps for the anodic layer; (right) printed and sintered anodic layer on metal foam [16]

Medesi et al. [63] have focused on a co-casting process that allows the fabrication of multilayer ceramics with a layer thickness of less than 25  $\mu\text{m}$ . The group used magnetically assisted stencil printing (MASP) to print patterned electrode layers onto the surface of dried green tape by using a mask but did not provide rheology data for the commercial paste used for printing. Another group, Li et al. [64], aimed to use a simple, inexpensive, and effective method which is stencil printing to fabricate grain-oriented lead-free PZT (lead zirconate titanate) ceramics. The study did not provide more information than that the printing was done repeatedly until the thickness of a 150  $\mu\text{m}$  thick multilayer film was achieved.

Zhao et al. [65] have worked on the fabrication of nitrogen-doped indium tin oxide (ITO) and platinum (Pt) thin-film thermocouples to enable in-situ surface temperature measurements of aero turbine blades. However, the group focused on characterizing and calibrating the printed thermocouples rather than providing at least some information about the printing process. Figure 12 indicates the stencil-printed thermocouples are less than 30  $\mu\text{m}$  thick on an alumina substrate. For future electronic applications such as IoE (Internet of Everything) or wearable devices for PZT ceramic sensor fabrication, PZT-containing composite ink has been stencil printed in a study [17]. This was done on a polyethylene terephthalate

(PET) polymer substrate through a 200  $\mu\text{m}$  thick stencil without any rheological characterization of the ink.

A general issue I noticed in this literature review was that the rheological measurements were not well considered in many cases, and in one or two studies more than flow curves were not obtained. Characterizing the paste just by looking at the consistency may not be the best way to ensure a successful and repeatable stencil printing process.



*Figure 12 Stencil printed ITON/Pt thin film thermocouple on alumina substrate [65]*

#### 2.4.2. Use of stencil printing in different fields

A current topic, the chip shortage in the automotive industry, may be interesting to mention because of the role of stencil printing in the production of flip chips in the electronics industry. Flip chip technology requires the formation of bumps for board assembly, but a low-cost bumping process is needed to make the overall production system cost-effective. Therefore, there are many studies in the literature focusing on solder paste stencil printing with consideration of paste rheology and printing parameters.

In terms of low-cost flip-chip bumping using stencil printing, one group as an example in the literature [66] gave importance to the stencil printing parameters and stencil design. Therefore, the dimensional stability of the aperture and the quality of the printing on a micrometer scale were emphasized. The group set the squeegee angle at 60° to ensure obtaining a better aperture filling by considering the aperture width and average particle size ratio for better paste release, longer stencil life, and aperture filling. The type of stencil, either laser-cut or electroformed, was also considered for aperture wall quality. Similar to the latter, another group [67] highlighted the need to better understand and control the flow and deformation behavior of solder pastes. The close relationship between paste transfer efficiency and stencil aperture size as well as the correlation of paste rheological behavior with transfer efficiency were investigated. Therefore, a detailed rheological investigation of pastes was performed in the study, taking into account the flow behavior, viscoelastic behavior, and time-dependent behavior of the pastes.

Solder paste printing is a broad area where stencil printing has been used and studied. A major source of soldering defects in surface mounting technology has been attributed to the solder paste stencil printing process where rheology, modeling, and optimization studies have been coupled to improve the printing results. For further interest, these works can be reviewed in the literature [15,68–76].

It is obvious that the mass of knowledge in the microelectronics field about the stencil printing process is useful and can be used to improve the printing process in the ceramic field.

## 2.5. Four-point probe measurements

The stencil-printed ribs must be characterized in terms of their conductivity values, which can be used to optimize their widths and the width of the channels that can be modeled using numerical methods.

This method is based on four contacts: two of them are used to apply the current and the other two are used to measure the voltage drop. It is an advantageous method for eliminating voltage drops across wires or contacts.

In addition, it has different measurement modes, such as van der Pauw mode, collinear mode, square mode, and dual probe configuration mode. The most common is the collinear mode [77] (see Figure 13) which was used in this study for the electrical characterization of printed LSCF stripes.

The four-point probe resistance ( $R$ ) is calculated with voltage over current which is based on the measurement principle. The current is applied from the outer wires and the voltage drop is measured from the inner wires.

The conductivity of a printed LSCF stripe can be calculated using Equation 6,

$$\sigma = 1/R \times L/A \quad (6)$$

where  $\sigma$  is the conductivity,  $R$  is the resistance,  $L$  is the length (distance between inner wires), and  $A$  is the area which is equal to the thickness multiplied by the width of the measured shape.

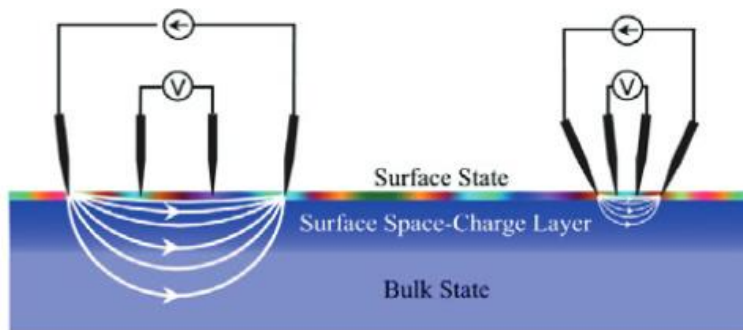


Figure 13 Schematic illustration of the collinear four-point probe measurement setup in macro (left) and micro (right) scale [77]

## 3. Materials and Methods

### 3.1. Used perovskites

#### 3.1.1. LCC2

Anode-supported cells have been developed and used in stack tests at Jülich since the mid-1990s. One of the stack designs used at that time was the 5th generation, the so-called F-design, with a metal interconnect. A modified ferritic steel, coded JS-3 (later-on licensed to VDM Metals as Crofer 22 APU), was used for the E-design short stack test with a cathode contact layer of LCC2 specially developed for JS-3 [78]. The remainder of this powder has since been stored at IEK-1 and used in this study for paste preparation to gain experience.

The  $(\text{La}, \text{Ca})(\text{Cr}, \text{Co}, \text{Cu})\text{O}_3$  powder was synthesized in-house by spray drying followed by calcination at 900 °C.

#### 3.1.2. LSCF

This is the material that was planned to be used within the frame of this work as a cathode contact layer, which must have some properties such as sufficient electronic conductivity, stability in an oxidizing atmosphere, chemical stability, and compatibility with adjacent layers as mentioned in the literature [79]. At this point, the thermal expansion behavior of this material will be compatible with one of the most commonly used cathode materials, LSCF, from one side [80], and another side with MCF coating on the interconnect [79]. Therefore, this material was chosen for the paste preparation to stencil print the 3D geometries desired in this dissertation.

$\text{La}_{0.58}\text{Sr}_{0.4}\text{Co}_{0.2}\text{Fe}_{0.8}\text{O}_3$  powder was synthesized in-house by spray drying and calcined at 900 °C.

### 3.2. Substrates

The surface characteristics and flatness of the substrates should be well considered for the printing process, i.e. printing a paste on a porous surface requires a different rheological behavior than a paste printed on a dense substrate surface. Therefore, the paste must be designed according to the surface characteristics of the substrates because of the differences in the adhesion of the paste to the substrate surface. On the other hand, if the surface flatness of the printed stripes is to be achieved, the flatness of the substrate used should also be considered in order to avoid printing errors.

Initially, 35 mm diameter pellets of LSCF powder were pressed and sintered. LSCF was intentionally chosen so that the pellets could be printed on the same surface as the cathode surface of industrial-size cells. However, bending and cracking were the limitations in pellet fabrication. Several adjustments were tried to prevent them, but no definite improvement was achieved. Pellet fabrication is far from the goal of this work, so this topic will not be mentioned again.

Commercially available anode-supported Elcogen complete cells in the size of 10 cm to 10 cm were utilized as a “substrate” for the printing of ceramic stripes. This size is more beneficial than a button size, because the industrial-size printing results can be directly examined and evaluated for cell assembly into a stack.

20 mm x 20 mm Kerafol 3YSZ supports were also utilized in this study. It allowed us to observe how a prepared paste behaves on a different surface characteristic.

### 3.3. Printing process

The printing process involves several steps from paste preparation to the setting of printing parameters. An appropriate paste formulation and rheological characterization are a must for an adequate paste behavior that is linked to the desired printing results. Once the paste is ready, printing parameters are considered to complete the printing process.

The prepared paste recipes within this work mainly contained solid loading which is the powder of the chosen perovskite material; solvent which is the terpineol; binder which is the ethyl cellulose (EC); and rheology additive as a dispersing and wetting agent. The binder used was added to the batch as a mixture of solvent and binder, which is called a transport agent.

EC was used as an organic binder and a rheology modifier that dissolved in terpineol. EC and terpineol mixture was found in a study [81] that it generates non-Newtonian fluid which is desired for this work. A rheological additive was used to create a three-dimensional network within the paste structure, therefore Anti-Terra-204 (BYK, Germany) was chosen.

Three different paste preparation routes were followed with different recipes. The basic one was the addition of a solid loading and transport agent. With the addition of a dispersing agent to the recipe, the route was changed: dissolving the dispersing agent was used as the first step. All other details were explained in the experimental sections of Chapter 4 and Chapter 5.

The printing parameters on the screen printer are seven. If a waiting time (a delay for a separation of the substrate from the stencil) is applied, the total number of variables becomes eight. Snap-off distance and LP (Leiterplatte in German which means circuit board) thickness are related to the distance between the stencil and the moving board. On the board, a metal sheet is used to fix the substrate which has a certain thickness. The LP thickness value can be chosen similar to this thickness. Snap-off distance is then the gap between the surface of the substrate and the stencil. Squeegee-related parameters are squeegee pressure, squeegee speed, and squeegee travel distance. How far the squeegee moves was not considered in this study. Furthermore, the moving table has two variables; separation distance and separation speed. How far and how fast the moving table moves down is related to the latter two variables. The values chosen for these parameters were mentioned in chapters 4 and 5.

The pastes were printed by using two different stencils. Details of these stencils with a schematic illustration are given in Chapter 5. Stencil No:1 was mainly used for both LCC2- and LSCF-containing pastes. Stencil No:2 was used a few times and has smaller masks for YSZ substrates to see how pastes behave on a dense surface during printing and drying.

### 3.4. Characterization methods

#### 3.4.1. Particle size distribution

Particle size distribution (PSD) is the method to analyze the PSD of dispersed particles in a suspension by laser diffraction. When the laser beam is subjected to the particles, each particle in the suspension diffracts the light. Depending on the particle size, the light is scattered intensely or weakly, at wide or narrow angles. The intensity and angle of the scattering are therefore recorded and then analyzed. There are two models for analyzing the collected data: Fraunhofer Approximation and Mie Theory [82,83]. The latter was chosen for the measurements with the refractive index of 2.20-0.2i LSCF powders and 2.4 for LCC2 powders due to its suitability for the analysis of smaller particles. PSD measurements were performed with the Horiba instrument (LA950-V2, Retsch GmbH, Germany) after the suspensions were subjected to the ultrasonic bath for several minutes to de-agglomerate and homogenize them.

#### 3.4.2. Surface area analysis

The BET (Brunner-Emmett-Teller theory) is used to measure the surface area of solid or porous materials. It is a critical property in material characterization to know as the surface of the material interacts with its environment. For example, the surface area of particles affects the rheology of prepared suspensions as reported in the literature [84]. In general, the samples are dried under a flow of inert gas to clean the surface and prevent contamination. At a given temperature, the volume of the gas covering the surface of the sample is measured by the BET theory in units of area per mass of the sample ( $\text{m}^2/\text{g}$ ).

In this work, this measurement has been made for the powders used in this study by conventional BET one-point  $\text{N}_2$  adsorption apparatus (Areamat, Jung Instruments GmbH, Germany).

#### 3.4.3. Rheological analysis

Rheological data were collected using a rheometer instrument (Physica MCR 301) with a plate-plate measurement setup (PP25/S) with a distance of 0.5 mm. All rheological measurements were conducted at 20 °C, and a pre-shear rate of  $1 \text{ s}^{-1}$  was applied to all. The field of rheology is wide and a standardization of program values in the rheometer requires some experience with early measurements. Therefore, at the beginning of this thesis, most of the LCC2 samples were pre-sheared for 30 seconds with a resting time of 30 seconds at zero shear rate immediately prior to the measurements, but then the values were adjusted. The updated values for all samples to obtain reproducible results are a pre-shear of  $1 \text{ s}^{-1}$  for 1 minute with a resting time of 1 minute at  $0.1 \text{ s}^{-1}$ .

On the other hand, three different rheological measurements were considered in this study to determine the paste behavior. They are plots of flow curves, a viscoelastic behavior, and a time-dependent behavior.

Shear rate vs. viscosity plots can be used to detect shear thinning or thickening of the paste, which provides information about the flow behavior of the pastes. In addition, zero-shear viscosity, i.e. a plateau at low shear rates, indicates that the paste is not stable at rest and can also be detected to gather information about the paste quality.

The viscoelastic behavior of the pastes was determined via the oscillatory amplitude sweep test (frequency: 10 rad/s). The presence of the yield point in the paste structure provides information about the strength of the paste structure. Shear stress vs  $G'$  (storage modulus - elastic response) and  $G''$  (loss modulus - viscous response) graphs are used to detect the yield point which is a sign of the viscoelasticity. If the latter is present in the paste, the paste degenerates itself after it flows with an applied shear over the yield point. However, this test does not provide information on recovery and structure formation.

An oscillatory step test (three-interval thixotropy test) was performed to simulate the printing/coating process with three intervals. At the first interval, the paste should be at rest, so a low shear is applied. This is used as a reference value. At the second interval, high shear is applied to simulate the printing/coating process. At the third interval, the paste is again at rest with a low shear (similar to interval 1) so that the time-dependent structure recovery can be measured.

#### 3.4.4. Scanning electron microscopy (SEM) with energy-dispersive X-ray spectroscopy (EDS)

Scanning Electron Microscopy (SEM) is the process of taking images of samples using a focused electron beam that produces signals (secondary electrons, backscattered electrons (BSE), and characteristic X-rays) after interacting with atoms in the sample. Backscatter is used to detect different chemical compositions, while secondary electrons are useful for topographical analysis. In elemental analysis, a characteristic X-ray is produced due to the energy differences between electron shells after an outer shell electron moves to a lower-level shell. The energy of this characteristic X-ray is unique to each element. Therefore, it is used to determine which elements are present in the sample and in what amounts. Collectively, this elemental analysis is called energy-dispersive X-ray spectroscopy (EDS) [85,86].

The microstructural evaluation of sintered specimens for shape detection of printed stripes and the analysis of their microstructure was performed via scanning electron microscopy (Hitachi TM3000 tabletop SEM - Japan). BSE-SEM images of the samples were published in this thesis with an EDS analysis.

The sample preparation step was also performed after the printed and sintered samples were crushed for cross-sectional analysis. The specimens were embedded in epoxy (EpoFix, Struers, Germany), and ground with grinding papers of grit size 80 to 2500 in several steps. Polishing was performed on perforated cloths soaked with diamond particle suspensions of 3  $\mu\text{m}$  and 1  $\mu\text{m}$ . The final polishing step was performed with 0.05  $\mu\text{m}$  colloidal silica. Finally, the samples were sputter coated (Cressington 108 auto coater, UK) with gold to avoid charging problems on the sample during the measurements.

#### 3.4.5. Confocal laser microscopy

Conventional optical microscopy provides two-dimensional (2D) information, while confocal laser microscopy enables the construction of three-dimensional (3D) images by rejecting light that does not come from the focal plane [87]. This advantage of 3D image generation for the shape of pellets and their surface flatness with the edge cavity, the printed ribs were characterized via a confocal laser microscope (Keyence, Germany). Through the analysis software, a profile mode can be applied to the measured data where the surface flatness can be better detected and compared.

#### 3.4.6. White light topography

Surface roughness, geometry, and flatness measurements can be performed to characterize samples via white light topography. The usefulness of this method for this work is that large samples (10 cm to 10 cm) can be characterized and evaluated in terms of height distribution and surface flatness of printed ribs. Therefore, the samples were characterized using a non-contact profilometer (CyberSCAN CT 350T, cyberTECHNOLOGIES GmbH, Germany), equipped with a chromatic sensor head (CHRocodile E10000, Precitec Optronic GmbH, Germany). Surfaces (10 cm x 10 cm) were analyzed with a scan step size of 20  $\mu\text{m}$  x 500  $\mu\text{m}$ .

#### 3.4.7. Four-point probe (4PP) measurements

The collinear four-point probe measurements were performed to electrically characterize the LSCF stripes and the LSCF cathode layer. The current was applied from outer wires through a DC power source (Keithley 2230-30-1) and the voltage drop between two inner wires was recorded with a voltmeter (Fluke Deutschland GmbH, Germany).

Measurements were made over a temperature range of 650 to 850  $^{\circ}\text{C}$  (External Thermo Couple (Dostmann Electronic GmbH, Germany)) and I/V curves were plotted to calculate the conductivity of the stripe which was printed on an  $\text{Al}_2\text{O}_3$  substrate. The latter is an electrically non-conducting material and was used to obtain only the conductivity of the printed stripe.



## 4. Stencil printing of LCC2

### 4.1. Capital introduction

Lanthanum Calcium Chromium Cobalt Copper Oxide (LCC2) is the material used as a cathode contact material in the former Jülich stacks. It is an in-house synthesized spray-dried perovskite powder that was used for the experimental process to prepare a suitable paste recipe for printing half-millimeter-thick ceramic stripes on a substrate. A learning-by-doing process was sought due to the complexity of the overall printing process, which includes so many variable parameters.

Printing experience includes; printability of the paste without printing failures such as stencil clogging; suitable paste characteristics for the desired geometry which is related to the paste recipe and preparation; suitable printing parameters to manage/assist the printing process by influencing the result. The prepared pastes should exhibit shear-thinning behavior. The paste structure that is ruptured by the applied shear should recover itself to retain the printed shape which can be influenced by paste formulations studied by rheological measurements. Moreover, stencil printing parameters should be set appropriately to ensure that the paste will be well printed. This cannot be known exactly without trying as the influence of the parameters on the printing experience can vary from paste to paste.

Stencil printing is the technique chosen for the printing process. A stencil was used instead of a screen. This technique is rarely used in the field of ceramics and only a few studies can be found in the literature [16,17]. However, it is useful for printing thicker layers (about 200  $\mu\text{m}$  and above) compared to the screen printing method [11,12].

In this study, six different paste recipes were prepared. As a starting point, five of them were prepared simply by mixing transport agent and solid loading according to the procedural instructions in Jülich for a LSCF air-electrode slurry to be printed by screen printing (standard operation procedure No. VAW 007.2.3). However, it is subsequently revised according to the literature and some necessities for the process.

The behavior of the five pastes was investigated after adjusting the binder content and solid loading, supported by rheological measurements and printing results. As the binder content was increased, the viscosity of the pastes increased. The consistency was changed, but the shape characteristic on printed ribs did not change. Increased solid loading affected paste viscosity as well. However, it led to an increase in tackiness resulting in cracking on printed ribs and stencil clogging as a print failure.

In addition, several printing parameters were varied to improve the surface flatness. The dome-like shape due to sagging remained in the printed ribs made with all five pastes. Therefore, a complete revision of the paste recipes with their preparation methods was made and different printing parameters were set, which were modified according to the literature and the needs of the process. The sixth paste was prepared in relation to this revision and the difference in paste rheology and printing results were investigated via some characterization methods.

Overall, it was observed that the printing results changed after the addition of dispersant and the use of different particle sizes within the batches of pastes including several adjustments in the printing parameters.

## 4.2. Experimental part

### 4.2.1. Material

The materials used in the paste preparation are:

- Ethyl cellulose as a binder (EC) (10 cP - No. 200689, Aldrich, Sigma-Aldrich Chemie GmbH and 45 cP - No. E8003, Sigma, Sigma-Aldrich Chemie GmbH)
- Terpineol as a solvent ( $C_{10}H_{18}O$ , No. 86480, Aldrich mixture of isomers, anhydrous, Sigma-Aldrich Chemie GmbH, Taufkirchen, Germany;  $\rho = 0.925 \text{ g/cm}^3$ )
- In-house spray-dried LCC2 powder ( $La_{0.8}Ca_{0.2}Cr_{0.1}Co_{0.3}Cu_{0.6}O_{3-6}$ ) as solid content
- Dispersing agent named ANTI-TERRA-204 (Wetting and dispersing agent, BYK-Chemie GmbH, Germany)

LCC2 powder was used in this study as a representative perovskite material to gain experience in the printing process and the knowledge gained can then be applied to the state-of-the-art perovskite material of LSCF (Lanthanum Strontium Cobalt Ferrite) in the fabrication of the cathode contact layers.

The LCC2 powder was ball milled for 2 hours to be used in the pastes P1 to P5, while raw powder was utilized for paste P6. Their particle size distribution (PSD) plots are shown in Figure 14. Details of the particle size values are given in Table 2.

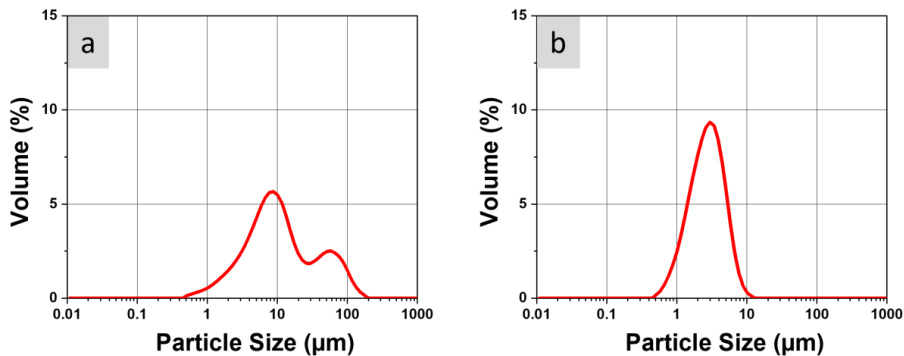


Figure 14 a) PSD of LCC2 raw powder after the spray drying process, b) PSD of LCC2 raw powder after 2 hours of ball milling

Table 2 Particle sizes of LCC2 as raw and 2 hours ball-milled powder

Name	LCC2 – Raw powder	LCC2 – 2h milling
Particle size	D(v,0.1) 2.43 (μm) D(v,0.5) 9.07 (μm) D(v,0.9) 58.79 (μm)	D(v,0.1) 1.15 (μm) D(v,0.5) 2.53 (μm) D(v,0.9) 4.96 (μm)

#### 4.2.2. Paste compositions and preparation routes

Six different paste formulations were prepared and their contents are listed in Table 3. The first five formulations listed in the table were prepared by only solid content and transport agent, while paste P6 contained additional solvent and rheology additive (dispersant) as different from the others. For the latter paste, a different paste preparation route was followed with a shortened binder chain length (10 cP instead of 45 cP). In addition, the particle size was changed: bi-modal PSD was preferred instead of mono-modal PSD, which was the case for the other five.

As can be seen in Table 3, the binder content was increased in pastes P1, P2, and P3, while keeping the solid loading constant. The solid content of pastes P1 and P2 was increased and then renamed pastes P4 and P5, respectively. The amount of binder and solvent in grams was kept constant in the batches. For these five pastes, Figure 15-a shows the preparation route in which a pre-prepared transport agent (15% binder containing solvent prepared by mixing with a laboratory mixer to a certain consistency) was mixed with 2 hours of ball-milled solid content via a planetary centrifugal mixer (THINKY mixer ARV-930 TWIN) for five times (each for 90 seconds at 1000 U/min) with a few minutes pause between each step to obtain a well-mixed paste.

An alternative paste preparation route was followed for paste P6 (see Figure 15-b). First, a pre-suspension, which is the mixture of the dispersant and the solvent, was prepared by a handshake for approx. 2-3 minutes until the mixture reaches a certain level of transparency. Followed by the powder and the transport agent were added into the pre-suspension in several steps, each step being mixed by the centrifugal mixer to ensure that the liquid content could wet the solid content.

Table 3 Compositions of prepared pastes

Name of the paste	Content of transport agent (g)	EC in transport agent (%)	Chain length of EC (CPs)	Content of solid (LCC2 powder) (g)	Content of additional solvent (g)	Dispersant (g)	EC in the paste (wt.%)	Powder in the paste (wt.%)	Solvent in the paste (wt.%)	Dispersant in the paste (wt.%)
Paste P1	60	10	45	60	0	0	5	50	45	0
Paste P2	55	15	45	55	0	0	7.5	50	42,5	0
Paste P3	60	20	45	60	0	5	10	50	40	0
Paste P4	60	10	45	100	0	0	3.75	62.5	33.75	0
Paste P5	55	15	45	95	0	0	5.5	63.3	31.2	0
Paste P6	13	15	10	100	5	15	1.5	75.2	12.1	11.3

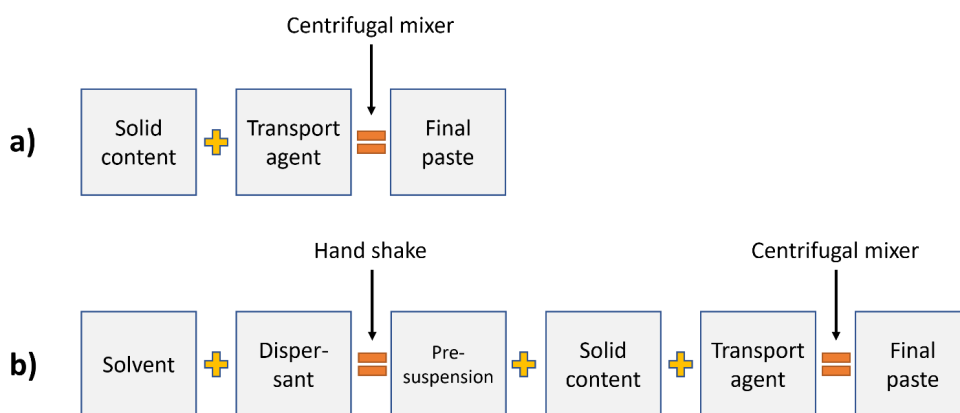


Figure 15 Paste preparation routes for a) Pastes P1 to P5 and b) Paste P6

#### 4.2.3. Stencil printing experiment and process parameters

Stencil printing was performed via an EKRA E2 semi-automatic printer. The used stencil, named “Stencil No:1”, is 0.5 mm thick and 1.5 mm wide for each of the ribs and channels, with the apertures on the stencil surface representing the ribs on the substrate after printing (see Table 9). With this rib-channel design on the stencil, the pastes were printed on 10 cm by 10 cm solid oxide cells (0.5 mm thick Elcogen cells).

The printing was performed as follows: two squeegees with a 30° angle moved forward and backward on the stencil to push the paste through the apertures onto the surface of the substrate. At this point, the

squeegees contribute three variable parameters to the printing process: the pressure applied to the stencil, the speed of movement, and the printing distance. When the squeegee movement is complete, the printed substrate moves down and separation from the stencil occurs. The separation speed and the separation distance can also be set. On the other hand, the distance between the substrate and the stencil can be changed by setting two parameters which are the LP thickness and the snap-off distance. The LP thickness can be set according to the thickness of the substrate used. The snap-off distance can be considered for the desired distance between the surface of the substrate and the bottom of the stencil. Waiting time right after printing before the separation cannot be set but is manually applied to the printing process, which can be defined as one of the process parameters.

The parameters explained above (except for the delay time) were listed in Table 4 with the selected values. Pastes P1 to P5 were printed under Print A and paste P6 was printed under Print 2 conditions as shown in the same table. The squeegee pressure, snap-off distance, and separation speed parameters were varied in Print A, as shown in Table 5. Print conditions A-1 to A-4 were additionally applied to paste P3; Print A-5 to paste P5.

*Table 4 Listed printing parameters under Print A conditions for pastes P1 to P5, and Print 2 conditions for paste P6*

<b>Variations</b>	<b>Print A</b>	<b>Print 2</b>
Snap-off Distance	0 mm	0 mm
Pressure of Squeegees	5 Bar	5 Bar
Separation Speed	0.5 mm/s	1 mm/s
Separation Distance	3 mm	3 mm
LP Thickness	0.3 mm	0.5 mm
Speed of Squeegees	110 mm/s	20 mm/s

*Table 5 Varied printing parameters of Print A*

<b>Name</b>	<b>Pressure (bar)</b>	<b>Snap-off distance (mm)</b>	<b>Separation speed (mm/s)</b>
Print A-1	2	0	0.5
Print A-2	2	1	0.5
Print A-3	5	1	0.5
Print A-4	5	-1	0.5
Print A-5	5	0	0.1

#### 4.2.4. Characterization of the pastes and printed ribs

The rheological data were collected using a rheometer instrument (Physica MCR 301) with a plate-plate measuring set-up (PP25/S) at a distance of 0.5 mm. All rheological measurements were carried out at 20 °C and a pre-shearing of  $1 \text{ s}^{-1}$  for 30 seconds with a rest time of 30 seconds at zero shear rate was applied to pastes P1 to P5, while a pre-shearing of  $1 \text{ s}^{-1}$  for one minute with a rest time of one minute at a shear rate of  $0.1 \text{ s}^{-1}$  was applied for paste P6 right before the measurements.

The flow behavior of the pastes was determined over the shear rate range from 0.1 to about  $2200 \text{ s}^{-1}$ . The viscoelastic behavior of the pastes was determined via the oscillatory amplitude sweep test (Frequency:  $10 \text{ rad/s}$ ) which provides information on how the paste structure changes under applied deformation. The response of the paste to the applied shear is measured in terms of  $G'$  which refers to the elastic response (solid-like behavior), and  $G''$ , which refers to the viscous response (liquid-like behavior). Next, the oscillatory step test (three-interval thixotropy test) was performed to observe the time-dependent behavior of pastes, where the test includes three intervals. At the first and third intervals, the paste is at rest with an applied shear of  $0.1 \text{ s}^{-1}$ . The second interval is the representative of printing. Therefore, a higher shear rate is applied. The high shear rate aims to break up the paste structure, whose behavior can be observed at the third interval under almost no shear rate to know if the structure recovers itself or not. If it recovers, how fast and how much recovery will occur can be observed.

The printed ribs were dried at 80 °C overnight and heat-treated at 850 °C in the air in a furnace for 10 hours with a 5 K/min ramp for both heating and cooling. The reason of the chosen temperature for heat treatment and dwell time (100 hours in real application) are overall to simulate stacking of cells. The shape of the three-dimensional printed ribs in terms of surface flatness and the edge cavity was determined by cross-sectional images using scanning electron microscopy and laser microscopy. Printing failures, such as stencil clogging, were also revealed by photographic images.

### 4.3. Results & Discussion

#### 4.3.1. Process parameters in stencil printing

Stencil printing is a complex system with many variable parameters. Amalu et al. [67] listed these parameters and divided them into five categories:

- Stencil parameters
- Paste parameters
- Substrate parameters
- Printer parameters
- Environmental parameters

Each category also has sub-variables and each of them has its own way of influencing the printing process. It is not 100% certain how much influence each variable has, as this depends on the printing conditions, including the rheological properties of the pastes. However, one study generalizes some points about parameter interactions in stencil printing that can be found in the literature [6]. It was found that the effect of the pressure applied by the squeegee was significant in terms of its interaction with printing and

aperture geometry parameters. The squeegee speed and the separation speed were also included in the data analysis with two-way interactions of the parameters.

The way to determine how parameters affect printing results is to change one variable while keeping the others constant, which is what has been done in this study. However, which parameters to vary is a choice based on the needs and objectives of the investigation. One group in the literature wanted to observe the paste release efficiency during stencil printing, therefore they varied some parameters such as aperture shape, stencil thickness, and paste type [88]. Another group focused on the flow processes of the paste in stencil printing and investigated the influence of the size and the shape of the paste particles as well as their packing ability with rheological aspects on the printing experience [89]. Another study highlighted that the variation of printing parameters may lose its significant importance for some kinds of pastes in terms of achieving the desired geometry on printed shapes [90]. All these indicate that not only the printing parameters, but also the factors that influence the paste behavior should be considered in order to achieve the desired results in the end.

To achieve surface flatness on printed ribs within the frame of this work, binder and solid content in the paste recipes were varied with squeegee pressure, snap-off distance, and separation speed in the printing parameters during the preparation/printing of pastes containing LCC2. In this way, it was possible to see the influence of the different parameters on the printing experience, not only on the shape of the printed geometries, but also on some aspects such as the printability of the paste, i.e. stencil clogging, sagging after printing or microstructural changes, i.e. crack formation.

#### 4.3.2. Influence of Different Paste Formulations on the Printing Experience with Rheological Aspects

According to the recipes presented in Table 3, the binder content and the solid content were adjusted on the five different pastes (P1 to P5). As known and mentioned in the literature [10,91,92], an increase in the binder content causes an increase in viscosity, as shown in Figure 16, where paste P3 has the highest viscosity and paste P1 has the lowest one. The idea behind increasing the binder content was to increase the consistency level of the pastes to stop the sagging effect right after the printing. However, the addition of so much binder resulted in an increase in the tackiness of the pastes and a harder printability, which can be observed in paste P3. Approx. 3 minutes of pre-shearing was necessary to reduce the consistency before printing. On the other hand, less amount of binder resulted in an extremely fluid nature that caused paste P1 to show a high degree of sagging. A photo taken after printing can be seen in Figure 17-a. Pastes P1, P2, and P3 did not work according to the printing results that were characterized under the electron microscope (see Figure 18-a and -b). Paste P1 has no data due to the formation of almost a layer after a high degree of sagging occurred. For paste P2 and P3, a semicircular dome-like shape was observed, which has no surface flatness.

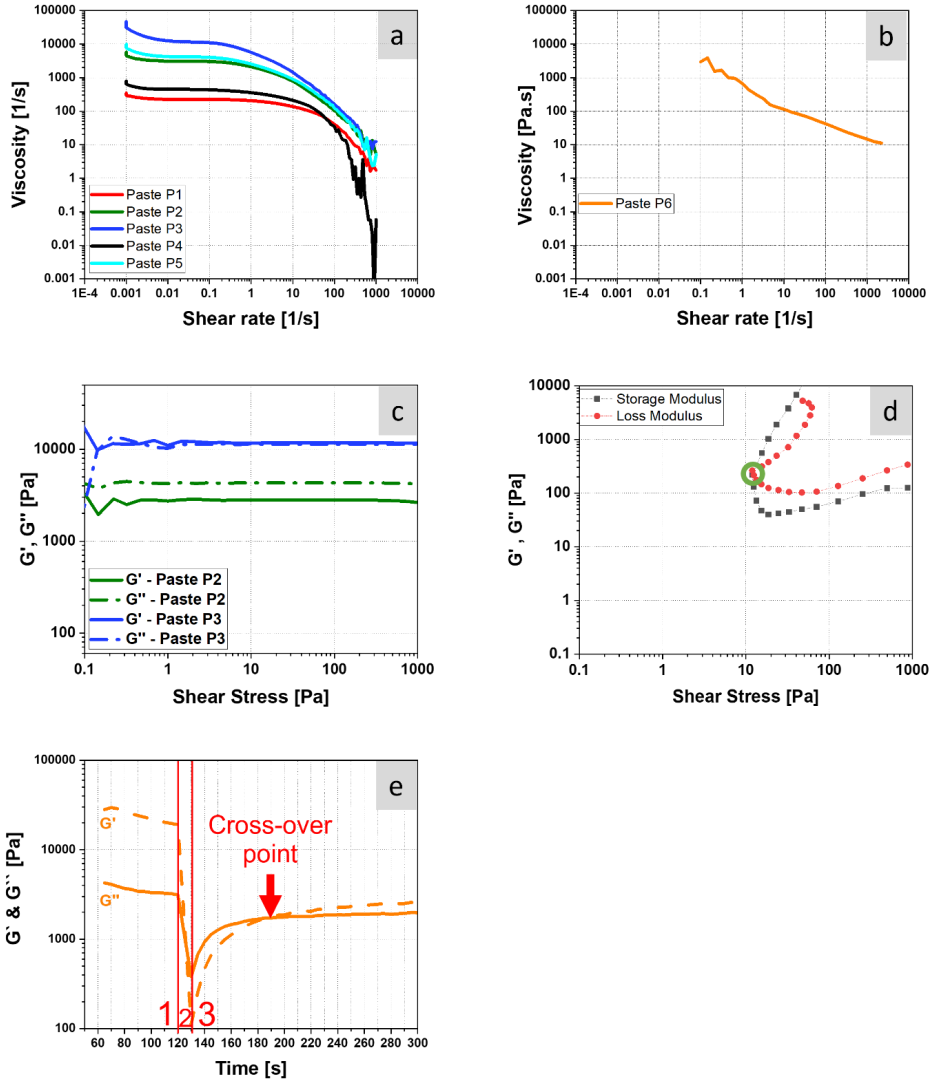


Figure 16 Rheological results of a) pastes P1 to P5 with their flow curves, b) paste P6 with its flow curve, c) pastes P2 and P3 with a plot for their viscoelastic behavior, d) paste P6 with a plot for its viscoelastic behavior and e) paste P6 with a plot for its time-dependent behavior



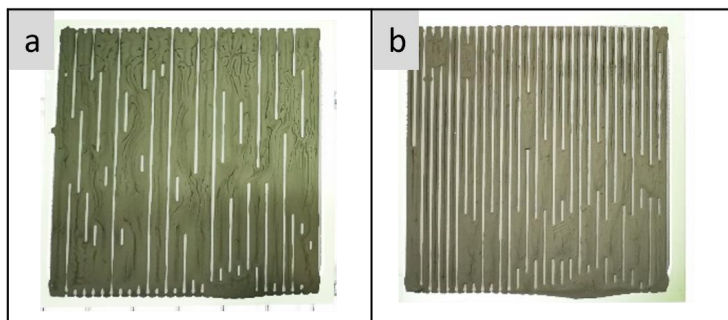


Figure 17 Printed stripes from a) paste P1 and b) paste P4 after drying in a furnace

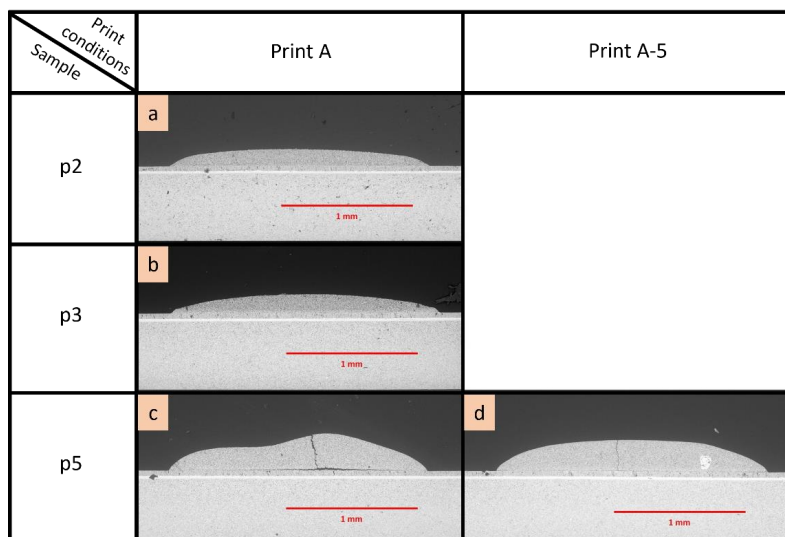


Figure 18 SEM images of Paste a) P2, b) P3, and c) P5 under Print A conditions, d) SEM image of paste P5 under Print A-5 conditions

The flow behavior of these three pastes with the plot of shear rate vs. viscosity (see Figure 16-a) indicates that the viscosity of the pastes decreases with increasing shear rate. This is a sign of shear-thinning behavior, which is beneficial during printing when the paste can flow and fill the stencil aperture with the applied shear. However, these pastes show plateaus of varying lengths at relatively low shear rates before the viscosity begins to decrease. This is known as zero-shear viscosity, which means that these samples are not stable at rest, and neither a 3D structural network nor a yield point (yield stress) can be expected from them.

The viscoelastic behavior of paste P2 and P3 with the plot of shear stress vs  $G'$  and  $G''$  (see Figure 16-b) indicates that the  $G''$  (viscous behavior) is higher than  $G'$  (elastic behavior) in the whole shear stress regime for sample P2. This means that the paste is a viscoelastic fluid rather than a viscoelastic solid. The curves are always in the linear viscoelastic region (LVR) and at no point in the given shear stress regime do they go down into the non-linear viscoelastic region (nLVR) where the inner structure of the paste is degenerated. Even at certain high shear rates, when these pastes are forced to yield, there will be no cross-over point where the paste is more elastic than viscous. On the other hand, Paste P3 shows similar behavior to P2 with one difference. Paste P3 has a very small yield point (cross-over point at about 0.15 Pa. in Figure 16-c), which does not change the characteristics of the paste behavior and the printing result. The pastes must stop flowing and maintain the shape of the stencil aperture, but this is possible with a paste that shows solid-like behavior ( $G' > G''$ ) right after the printing, which was not the case with paste P1, P2, and P3 (no data were shared for paste P1).

These results indicate that an increase in binder content causes greater consistency, but it does not mean that the paste will gain a structural network that will help to control the paste behavior in such a way that the structural build-up occurs after printing instead of sagging without any control. A study in the literature [10] mentioned that the binder content is useful for a network formation in the paste structure and the lack of binder leads to a viscoelastic fluid characteristic on pastes. However, the studied pastes already contain a dispersing agent, which is not the case for pastes P1 to P5. It is important to know that the presence of a dispersant in recipes should affect the behavior of the paste due to its interaction with the binder and the solid content [93,94]. The effect of a dispersant, which was used as a three-dimensional (3D) network generator, can be seen with paste P6 in 4.3.4. of this chapter.

Alternatively, the solid loading for pastes P4 and P5 was increased from 50% to ca. 62-63% to improve the paste behavior. A positive effect on paste rheology by increasing the solid loading has been reported in the literature [95,96]. An improvement in viscosity with less sagging effect was observed for paste P4 compared to paste P1 and the improvement in the printing results can be seen in Figure 17-b (for viscosity values, see Figure 16-a). However, bridging still occurred between the printed stripes. The reason is that the liquid-like behavior of paste P4 as well as paste P5 remained unchanged (no data published), the same as pastes P1, P2, and P3. As a result, dome-shaped prints remained on these two pastes after printing. Furthermore, an extremely tacky nature was observed on paste P5 with the increased solid amount, which led to cracks in the microstructure of the printed ribs, as shown in Figure 18-c, and stencil clogging as a printing failure, as seen in Figure 19.

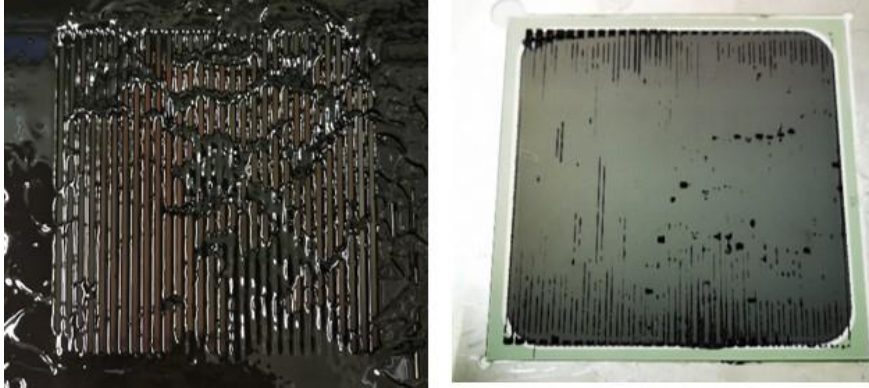


*Figure 19 Left) Stencil clogging due to the extreme tackiness of paste P5; right) An almost empty substrate surface after printing*

#### 4.3.3. Influence of varied stencil printing parameters on the printing experience

Pastes P1 to P5 were printed under "Print A" conditions (see Table 4). Pastes P1 and P4 showed sagging after printing and paste P2 had similar printing results as paste P3. Therefore, pastes P3 and P5 were chosen only to investigate the influence of varied printing parameters on the printing results in terms of any improvement in the shape of the ribs.

Paste P3 was printed and evaluated under four different Print A conditions (see Table 5). The shape of the rib - dome-like shape - remained similar for all prints that were observed after the characterization of the sample under the electron microscope (see Figure 20). However, the thickness of the ribs was affected and compared. The squeegee pressure was increased from 2 to 5 Pa (Print A-2 to A-3) while keeping the snap-off distance constant, resulting in a decrease in the thickness as shown in Table 6. This effect is due to a reduced gap underneath the stencil with increased squeegee pressure. On the other hand, the snap-off distance was increased from 0 mm to 1 mm (Print A-1 to A-2) while keeping the pressure constant. This increased the thickness of the printed ribs as calculated and listed in Table 6. These two varied parameters are a matter of increasing or decreasing the distance between the substrate and the stencil and both have similar effects on the printing process, which should be avoided by combining the variation parameters in a way that they have more impact on the output.

Another printing condition, Print A-5, was applied to paste P5, which has the highest solid loading than the others. The aim was to prevent crack formation and to improve the surface flatness of the ribs, which is the result of printing under Print A conditions as seen in Figure 18-c. The paste left the stencil aperture walls more slowly with a decrease in separation speed. A positive change with a thickness gain was seen in the shape of the printed rib (see Figure 18-d). The crack formation was minimized and the second dome-like shape generation at the top of the printed rib was prevented. However, the dome-like shape remained. From these experiments, it can be seen that the paste behavior dominates the printing parameters in terms of achieving the desired printing results. This does not mean that the printing parameters play no role. The printing parameters are important to achieve the desired printing results

once a suitable paste behavior has been achieved. In other words, they are tools that cannot dominate the printing results when a non-ideal paste is used.

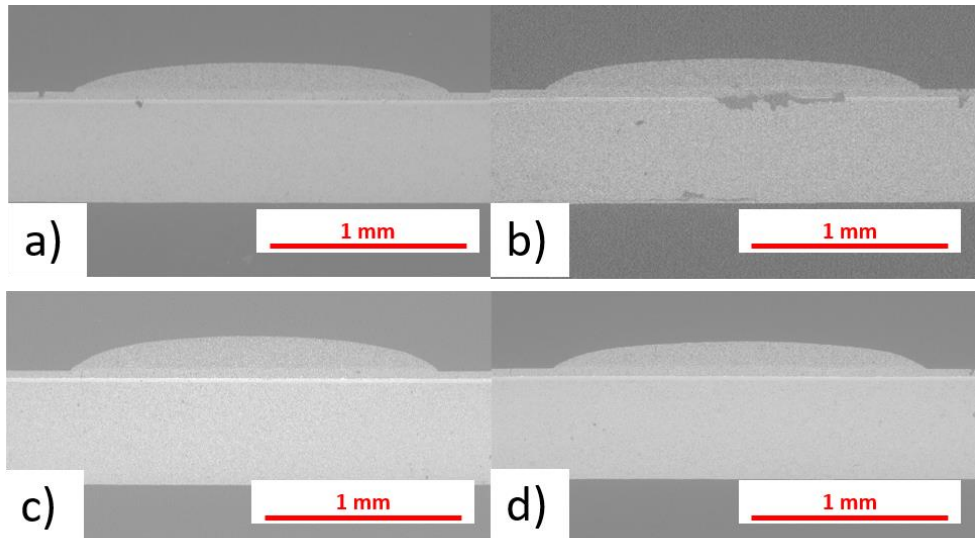


Figure 20 SEM images of paste P3 printed under four different printing conditions listed in Table 6. a) was under Print A-1, b) was under Print A-2, c) was under Print A-3 and d) was under Print A-4 printed

Table 6 Thickness values of printed ribs from paste P3 under four different printing conditions

Name of the printing variations	Thickness of a rib – 1 (μm)	Thickness of a rib – 2 (μm)
Print A-1	145	151
Print A-2	179	179
Print A	129	129
Print A-3	158	158
Print A-4	125	120

#### 4.3.4. Investigation of the revised paste recipe with revised printing parameters – Paste P6 and Print B

Due to the necessity of having a proper paste behavior to improve the surface flatness of the prints, the paste preparation method was renewed by changing two points:

- Having bi-modal PSD instead of mono-modal for the solid content
- Adding dispersant to the batch

These changes are in accordance with the literature. Tari et al. investigated that ceramic powder with bi-modal PSD and coarser particles enables obtaining batches with higher solid loading and lower viscosity compared to another ceramic powder with continuous PSD and finer particles [97]. A mixture of particles with different sizes in the prepared batches affected the rheological properties, which were also investigated [98,99]. The idea of varying the viscosity for a given solid loading and having control over some physical properties of the samples seems beneficial and may be the reason why commercial dispersions such as paints and inks do not have mono-modal PSD [98]. Bi-modal PSD is the result of a mixture of two different particle sizes, but LCC2 raw powder already indicates a bimodal PSD after the spray drying process (see Figure 14-a), thus it was used directly in the formulation of paste P6.

On the other hand, in terpeneol-based vehicles, ethyl cellulose was commonly used as a binder for the pastes used in the fabrication of some SOFC parts. The reason was that the use of the binder plays a role not only in the viscoelastic behavior of the pastes but also in the green properties of the printed samples [10]. Another group in the literature also pointed out that the ethyl cellulose in their prepared ceramic-based paste system was the reason for increasing the viscosity and dispersing the ceramic particles [100]. However, in this study, ethyl cellulose alone did not help to achieve proper paste behavior. Therefore, a dispersant was used in paste P6 to create a three-dimensional network and increase the particle-particle interactions within the paste structure, since the molecules/particles are in interaction along the flow direction when shear is applied to the paste should be well optimized [98].

In addition, the binder chain length was shortened for paste P6 to reduce both the consistency and tacky nature of the transport agent used in the paste preparation routes. This was practically beneficial for the paste preparation. Changes in the chemical structure of the molecules/particles within the paste vehicle with any influence on the rheology were not considered.

After applying the above-mentioned changes, the first thing that happened was that the solid loading within the revised batch increased up to 75 wt%, as already mentioned in the literature review. The rheological results indicate further changes in that the zero-shear viscosity disappeared as seen in the flow curve in Figure 16 with no plateau at lower shear rates. This indicates that the paste should have a yield point, which can be detected in the shear stress vs  $G'$  and  $G''$  plot. The cross-over point at about ca. 10 Pa is the yield point. The paste initially exhibits solid-like behavior, and liquid-like behavior dominates after this yield point, where the paste structure has been ruptured with increasing shear. When the shear is removed, a structural recovery is expected. As seen in Figure 16-d, at the third interval, 50-60 seconds are required to reach the cross-over point, which is the recovery time for the paste to return to a solid state again. This gives a hint that the separation of the substrate from the stencil should be delayed after the shear is removed until the recovery of the paste is completed. This may allow the paste to retain the desired shape as the aperture walls and the substrate surface act as a mold.

Therefore, a waiting time of 60 seconds after printing and before the separation was applied to the paste in the printing process, and the characteristics of the printed shapes changed with sharper edges on the printed ribs as seen in Figure 21. The surface of the ribs contains a high degree of topography, which may be due to the addition of dispersant that evaporated in the drying furnace. The LSCF-containing pastes listed in Chapter 5 contain ca. 3 wt% dispersant, so the amount in paste P6 should be reduced for further study if planned. However, ribs with the dome-like shape obtained in other pastes are no longer the case with the revised batch of paste P6.

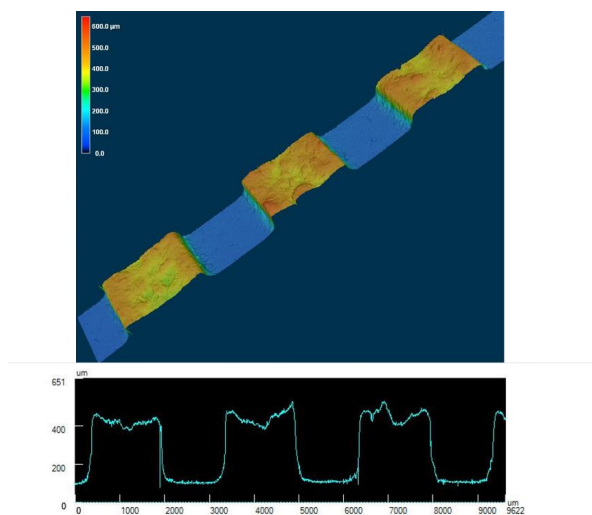


*Figure 21 Characterization of paste P6 under confocal laser microscopy in profile mode after printing under Print B conditions (dried at 60 °C overnight)*

Paste P6 was printed under Print 2 conditions (see Chapter 5), which is different from the printing conditions applied for pastes P1 to P5. Separation speed, LP thickness, and squeegee speed were varied. The separation speed was increased to speed up the process because the 60-second waiting time before the separation took place slowed down the process. The thickness of the LP should match the thickness of the substrate. The substrate used was not changed for any paste, but more contact between the substrate and the stencil was aimed at in the beginning by making the distance smaller than the thickness of the substrates. However, after gaining more experience in the field, it was decided that the exact thickness value of the substrate should be given to the LP thickness on the screen printer device. In addition, the squeegee speed was reduced to the recommended speeds of 20-50 mm/sec according to the literature [59].

Overall, the sum of the adjusted paste formulation and printing conditions changed the shape characteristics of the printed ribs. Although the surface flatness can still be improved, the LCC2 material used in these experiments is no longer used in the Jülich stacks, and it was only a training process to

investigate the paste preparation and stencil printing process. The experience gained with this material was then transferred to the state-of-the-art material LSCF.

#### 4.4. Chapter conclusion

Five paste formulations were varied by adjusting the binder and solid content and then printed under the same printing conditions to investigate the differences in paste behavior and printing results. According to the characterization results, the printed rib geometries were undesirable due to inappropriate paste behavior. Even though printing parameters of squeegee pressure, snap-off distance, and separation speed were varied to eliminate the undesired printing outcome, only a slight improvement in the shape and thickness of several ribs was observed. It indicated that the paste behavior dominated other varied factors, therefore the paste behavior was the focus to change its behavioral characteristics.

Paste P6 was alternatively prepared following a different preparation route and adjusted not only by adding a rheology additive but also by changing its particle size distribution from mono- to bi-modal. This resulted in an improvement in the paste behavior as indicated by the rheology results. A viscoelastic behavior with a yield point was achieved on the paste, which undergoes a structural breakdown when shear is applied. The paste structure self-degenerates and recovers its internal ruptured structure after printing. Structural build-up was also detected which helped to achieve sharper edges on the printed ribs. The shape characteristic of the ribs were completely positively changed, but the much addition of dispersant in the paste may be the reason for the uneven surface topography, which can be improved with further study on the paste formulation.

On the other hand, the potential of stencil printing in 3D manufacturing could also be seen with this study, as it allows cost-effectiveness and speed in the fabrication of 3D ceramic parts with simple shapes. Overall, a successful combination of variables optimized for the specific requirements is essential and will enable the desired results to be achieved in the printing process.

## 5. Stencil printing of LSCF

### 5.1. Capital introduction

LSCF (Lanthanum Strontium Cobalt Ferrite) is a well-known perovskite material due to its adequate properties for use as a cathode layer in SOFCs [79,101,102]. For the Jülich cells, the same material was also chosen for the cathode contact layer (CCL) in order to keep the coefficient of thermal expansion (CTE) the same as that of the cathode material, which is made of LSCF, and to ensure compatibility of the layers with each other [79]. As explained at the beginning of this thesis, the main objective is to print 500  $\mu\text{m}$  thick CCL with surface flatness on printed ribs with uniform height distribution for a cell assembly in a stack system for proper contacting. Therefore, the printing process, which includes paste formulation, paste preparation, and printing parameters, has been revised with respect to both the literature and the experience gained during the preparation and printing of the LCC2-containing pastes mentioned in Chapter 4.

The paste (Paste X3v2) prepared under this revision performed well according to the printing results. Thus, the main objective of this work was achieved. Nevertheless, the mechanism behind the successful printing process is further discussed with the main factors involved. In addition to this, some improvement possibilities for the process were suggested. Therefore, special importance was given to the rheological results to evaluate the paste behavior in relation to the paste recipes. The use of dispersant and the change in particle size with its distribution were studied by comparing several pastes, using Paste X3v2 as a reference. It was found that the 3D generator dispersant for the purpose of this work plays a crucial role and changes the characteristic of the printed shapes. The particle size also influences the paste behavior, which influences subsequently the printing results. A full recovery over time after printing was detected via rheology measurements. It is beneficial for the post-print structure build-up to retain the printed shape without sagging. Printing parameters played a complementary role with a manual intervention during the printing. A 20-second delay before the separation resulted in surface flatness of the printed stripes. However, successful printing results are still open for improvement, such as a slightly existing surface roughness that can be improved to make it smoother was suggested according to the printing results.

On the other hand, the reproducibility of the reference paste with printing results was attempted and conditionally achieved due to the lack of consideration of environmental effects and/or user factors with a semi-automatic printing machine. Furthermore, another reproducibility attempt was made for the results of a former employee who had the idea of printing the rib-channel form on the cell. His very first printing results were successful, but could not be reproduced directly. Several possible reasons for the failure have been discussed. Different batches of synthesized powders leading to failure due to changes in particle size were thought to be a major effect.

The technique used for printing was stencil printing and is well known for the solder paste applications in electronics. In the field of ceramics, it is not well known and rarely used that the thickness usually obtained in printings is 200  $\mu\text{m}$  as reported in the literature [12], while the achievement of 500  $\mu\text{m}$  thick ceramic stripes in this work is novel. For several applications in ceramic manufacturing, this technique will be a benchmark as a cost-effective and fast alternative one for several additive manufacturing techniques, i.e. 3D printers.



Overall, 500  $\mu\text{m}$  thick ceramic ribs on 10 cm to 10 cm Elcogen full cells were fabricated by stencil printing from the state-of-the-art material used in SOC fabrication - LSCF - and a promising surface flatness was achieved without any significant printing failure such as sagging or stencil clogging.

## 5.2. Experimental part

### 5.2.1. Material

The materials used in the paste preparation are:

- Ethyl cellulose as a binder (EC) (10 cP - No. 200689, Aldrich, Sigma-Aldrich Chemie GmbH and 45 cP - No. E8003, Sigma, Sigma-Aldrich Chemie GmbH)
- Terpineol as a solvent ( $\text{C}_{10}\text{H}_{18}\text{O}$ , No. 86480, Aldrich mixture of isomers, anhydrous, Sigma-Aldrich Chemie GmbH, Taufkirchen, Germany;  $\rho = 0.925 \text{ g/cm}^3$ )
- Transport agent for the mixture of ethyl cellulose and terpineol with the ratio of 15% EC and 85% Terpineol
- In-house spray-dried LSCF powder ( $\text{La}_{0.58}\text{Sr}_{0.4}\text{Co}_{0.8}\text{Fe}_{0.2}\text{O}_{3-6}$ ) as solid content with two different production series/batches (SP325-3 and SP319-1)
- Dispersant named ANTI-TERRA-204 (Wetting and dispersing agent, BYK-Chemie GmbH, Germany)

Particle size distribution (PSD) of two raw powders and SP325-3, ball-milled powders can be seen in Figure 22. Their detailed particle size values with BET-specific surface areas are shown in Table 7.

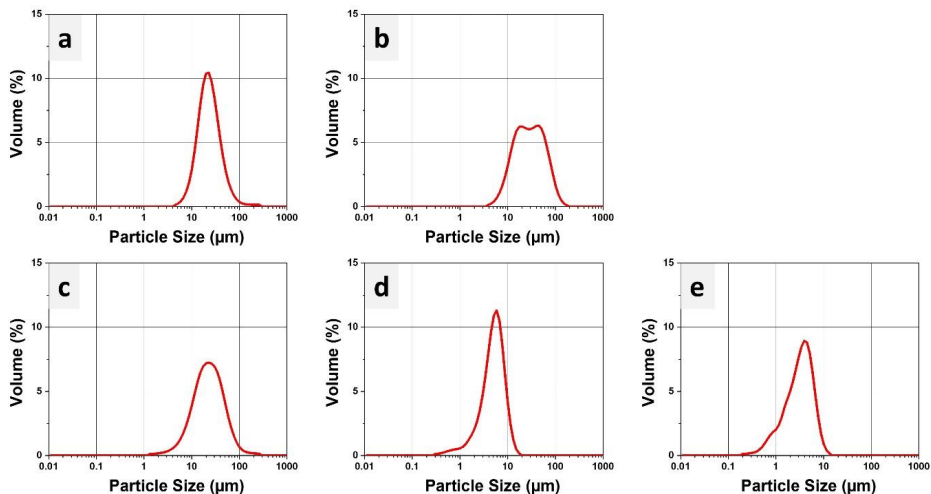


Figure 22 PSD of a) SP319-1 raw powder, b) SP325-3 raw powder, c) SP325-3 ball milled (BM) for 2 minutes, d) SP325-3 BM for 30 minutes, e) SP325-3 BM for 2 hours

Table 7 Particle sizes and BET values of the powders shown are listed here in the same order as in Figure 22

Name	SP 319-1 – LSCF – Raw powder		SP 325-3 – LSCF – Raw powder	
Particle size	D(v,0.1)	10.92 (μm)	D(v,0.1)	10.2 (μm)
	D(v,0.5)	21.02 (μm)	D(v,0.5)	26.3 (μm)
	D(v,0.9)	43.5 (μm)	D(v,0.9)	66.45 (μm)
BET	3.7 m²/g		3.45 m²/g	

Name	SP 325-3 – LSCF – 2 min BM		SP 325-3 – LSCF – 30 min BM		SP 325-3 – LSCF – 2 h BM	
Particle size	D(v,0.1)	7.91 (μm)	D(v,0.1)	2.02 (μm)	D(v,0.1)	1 (μm)
	D(v,0.5)	20.86 (μm)	D(v,0.5)	4.81 (μm)	D(v,0.5)	3.05 (μm)
	D(v,0.9)	51.23 (μm)	D(v,0.9)	8.49 (μm)	D(v,0.9)	6.01 (μm)
BET	3.26 m²/g		4.11 m²/g		4.28 m²/g	

### 5.2.2. Paste compositions and preparation routes

Several pastes with different compositions were prepared and listed in Table 8, which also includes the recipe of the former IEK-1 employee (“Paste of David”). The latter was attempted to be reproduced and therefore paste X1 was prepared. Paste X3v2 was kept as a reference paste for comparison. Paste X3v1 was prepared to compare the effect of monomodal and polymodal PSD on the paste behavior. Similar to the latter paste, OSB-a, and OSB-b were prepared to observe the effect of different particle sizes on paste behavior and printing results. OSB-c was used to observe the effect of dispersant on rheology and printing characteristics.

*Table 8 Contents of the recipes for the prepared pastes are listed below*

<b>Name of the paste</b>	<b>Content of transport agent (g)</b>	<b>EC in transport agent (%)</b>	<b>Chain length of EC (CPs)</b>	<b>Content of solid (LSCF powder) (g)</b>	<b>Content of additional solvent (g)</b>	<b>Dispersant (g)</b>	<b>EC in the paste (wt.%)</b>	<b>Powder in the paste (wt.%)</b>	<b>Solvent in the paste (wt.%)</b>	<b>Dispersant in the paste (wt.%)</b>
Paste of David	24	15	10	160	66	0	1.4	65	33	0
Paste X1	24	15	10	200	127	0	1	57	42	0
Paste X3v1	10	15	10	100	40	5	1	64.5	31.3	3.2
Paste X3v2	10	15	10	100	40	5	1	64.5	31.3	3.2
Paste X4	20	15	45	100	40	5	1.8	60.6	34.5	3
OSB-a	10	15	10	100	40	5	1	64.5	31.3	3.2
OSB-b	10	15	10	100	40	5	1	64.5	31.3	3.2
OSB-c	10	15	10	100	40	0	1	66.7	32.3	0

Regarding the paste preparation, the same route used by the former employee was followed for paste X1 with 3 roll milling and centrifugal mixing steps, schematically shown in Figure 23-a. The transport agent was mixed with solid content and solvent by hand using a spatula. The 3-roll mill ground and mixed the ingredients well according to a program. More solids were then added and mixed 5 times (90 sec each at 1000 U/min) using a centrifugal mixer (THINKY mixer ARV-930 TWIN).

For the other pastes, the route shown in Figure 23-b was followed. A pre-suspension was prepared with the mixture of dispersant and solvent by handshake for about 2-3 minutes. Then, the solid content (addition of powders with two different ball milling times in the ratio of 50:50) and transport agent were added in two steps. Between the two steps and at the end, the ingredients were mixed via a centrifugal mixer.

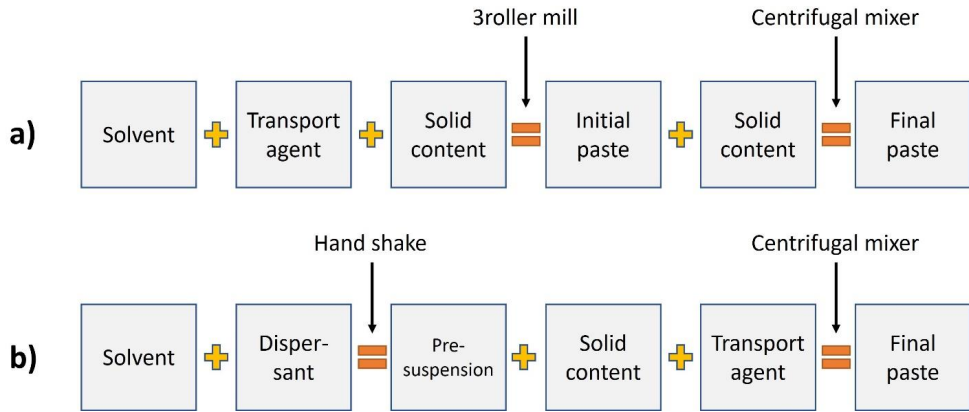
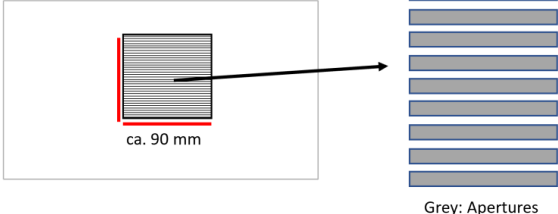
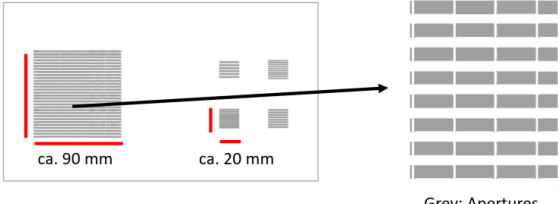


Figure 23 Paste preparation routes of a) Paste of David and Paste X1; b) the rest of the pastes listed in Table 8

### 5.2.3. Stencil printing experiment and process parameters

The stencil printing technique was applied via an EKRA E2 semi-automatic printer with two different stencils (No:1 and No:2) and two squeegees at a 30° angle. The No:1 stencil has a size of 9 cm to 9 cm size with a channel width of 1.5 mm and rib width of 1.5 mm, too (see Table 9). It is used for the pastes listed in Table 8. Stencil No:2 has four small stencil squares with different designs in the size of approx. 20 mm to 20 mm and one larger stencil square in the size of 9 cm to 9 cm with bridges along the length of the aperture as shown in Table 9. This stencil was used with Paste X3v2 and Paste X4.

Table 9 Schematical illustration of two different stencils

Stencil No:1	 <p>ca. 90 mm</p> <p>Grey: Apertures</p>
Stencil No:2	 <p>ca. 90 mm      ca. 20 mm</p> <p>Grey: Apertures</p>

Two different substrates were used for printing. One is an LSCF pellet in the size of 35 mm in diameter and Elcogen 10 cm to 10 cm full solid oxide cells. During printing, the squeegee moves forward and backward, technically printing the paste twice on the substrate. This was done for the old paste and paste X1. The other pastes were printed with only one direction of squeegee movement.

In addition, there are parameters to be set on the screen printer device and two different setups were utilized during printing (see Table 10). Print 1 was used for paste X1, while Print 2 was used for the rest of the pastes listed in Table 8.

Table 10 Listed printing parameters in two different setups

Variations	Print 1	Print 2
Snap-off Distance	0.5 mm	0 mm
Pressure of Squeegees	0.5 Bar	5 Bar
Separation Speed	0.5 mm/s	1 mm/s
Separation Distance	3 mm	3 mm
LP Thickness	0.5 mm	0.5 mm
Speed of Squeegees	110 mm/s	20 mm/s

#### 5.2.4. Characterization of the pastes and printed ribs

Rheological data were collected via a rheometer (Physica MCR 301) with a plate-plate measuring setup (PP25/S) with a distance of 0.5 mm. All rheological measurements were performed at 20 °C, and a pre-shearing of 1 s<sup>-1</sup> for 30 seconds with a resting time of 30 seconds at a shear rate of 0.1 s<sup>-1</sup> was applied to all samples right before the measurements to obtain reproducible results.

The flow behavior of the pastes was determined over the shear rate range of 0.1 - 2154 s<sup>-1</sup>. The viscoelastic behavior of the pastes was determined using the oscillatory amplitude sweep test (frequency: 10 rad/s), which provides information on how the paste structure changes under applied deformation. The response of the paste to the applied deformation is measured in terms of G', which refers to the elastic response (solid-like behavior) and G'', which refers to the viscous response (liquid-like behavior). However, the oscillatory test does not provide any information about the structural recovery of the paste. Questions such as "How long will the recovery take" and "How complete will the recovery be" etc. require a step test, also known as the three-interval thixotropy test. At the first interval, the paste is at rest under a low shear rate of 0.1 s<sup>-1</sup>, and then a high shear rate is applied at the second interval to demonstrate the printing process. Finally, a low shear rate of 0.1 s<sup>-1</sup> was applied to observe the paste and how it behaves as it is kept at rest. The above questions can be answered through the latter test.

The printed ribs were dried at 60 °C overnight and heat-treated at 850 °C for 10 hours in air with a 5 K/min ramp for both heating and cooling in a furnace. The geometries of the three-dimensional printed ribs in terms of surface flatness and edge cavity were determined from cross-sectional images via scanning electron microscopy (SEM) (Hitachi TM 3000), which was also used for microstructural evaluation of the ribs. The EDS mode of the SEM was also used to detect secondary phases in the microstructure. Image J/Fiji software was utilized to detect porosity from SEM images.

A laser microscope with profile mode was used to observe the surface flatness of the ribs. The height distribution of printed ribs over the whole area of the whole cell was detected by white light topography.

### 5.3. Results & Discussion

#### 5.3.1. Achievement of the desired printing results

Surface flatness and edge sharpness on printed ribs were promising and were achieved by using Paste X3v2. The achievement depended not only on achieving viscoelasticity and full recovery after printing, but also on well considering the recovery time of the paste as a printing parameter.

Viscoelasticity with the existence of yield point and structural build-up will be explained under the rheology part in this chapter, however, a complementary role of the recovery time for successful printing results, when it is considered during printing, was shown here in Figure 24-a. With no consideration of this waiting time led to an uneven surface flatness (see Figure 24-b).

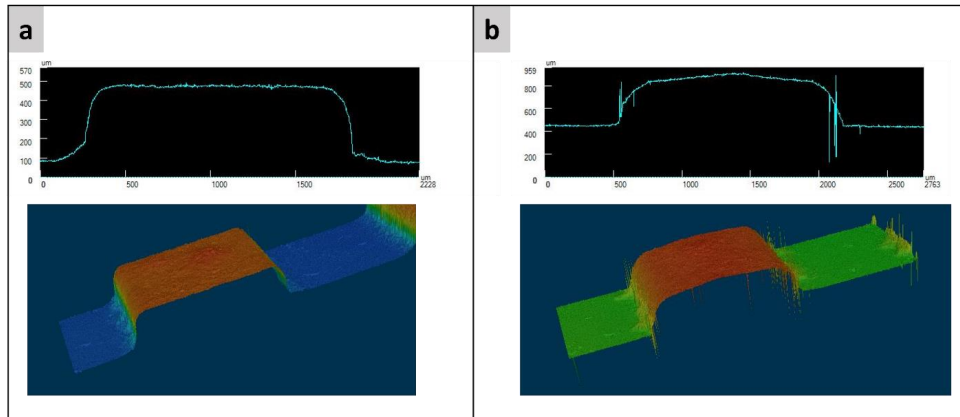


Figure 24 Printed ribs of Paste X3v2 under a laser microscope; a) after 20 sec. waiting time before separation of the substrate from the stencil, b) direct separation after printing (printed ribs were in a dried state)

The challenge with the recovery time is that there is no setup parameter in the screen printer, so the print must be manually stopped before the substrate and stencil are separated. This allows the paste to solidify and maintain its given shape through the stencil apertures, which act as a mold for 20 seconds. This waiting time was another challenge that could have caused the paste to be lost by sticking to the wall of the apertures; however, this did not happen due to the quality of the paste.

### 5.3.2. Characterization of the printed ribs from Paste X3v2

The first approach to characterize the printed ribs was to detect the surface flatness and the edge of them. It has been done via scanning electron microscopy (SEM) which was also used to detect the microstructure. An SEM image (see Figure 25-a) and a laser microscope image (see Figure 24-a) clearly showed the shape of the printed ribs, and the quality level of flatness seems promising. However, at this point, how much contact will be provided after the cells are assembled into a stack needs further investigation. Either a simulation to predict or a post-mortem stack test analysis to see the performance of these printed ribs under stack running conditions is required.

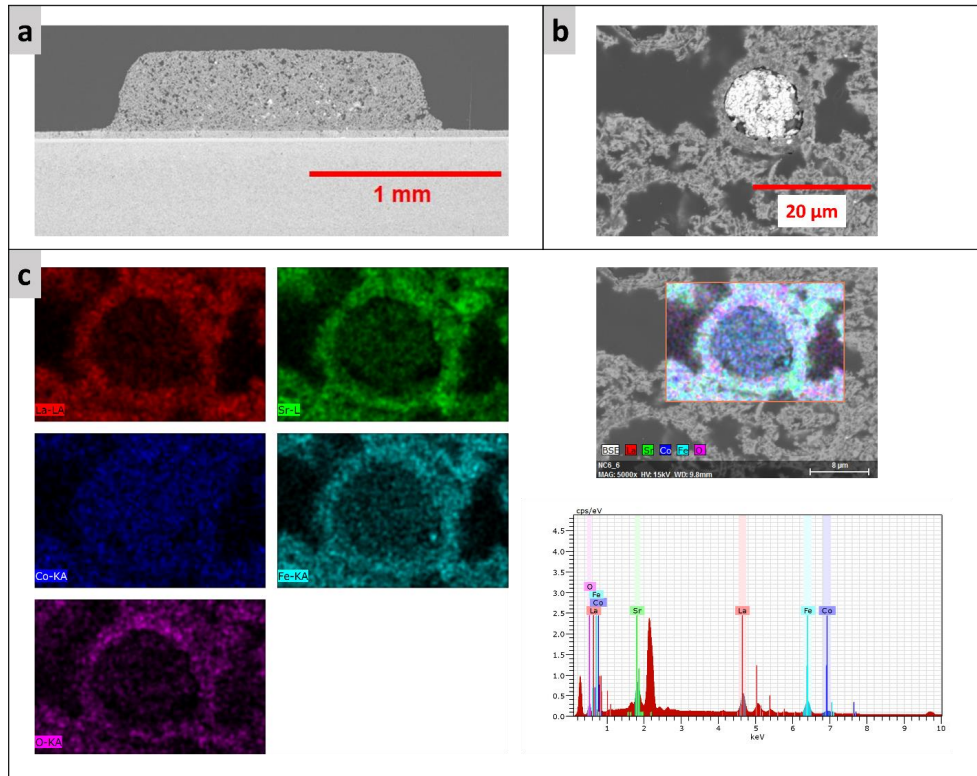


Figure 25 Printed and heat-treated rib under SEM (a and b) and its elemental analysis was studied by EDS (c)

In the context of cell assembly into a stack, the height distribution is an important factor for successful contact between the cell and the interconnect. The white light topography results (see Figure 26) showed that the 30 printed stripes through stencil no:1 appear to have a homogeneous distribution. Precise values and comparisons of the height of each stripe are required by measuring both sides using the same topography measurements. On the other hand, surface roughness was also detected, again shown in Figure 26, highlighted by the red rectangle, indicating that the smoothness is open to improvement. A general assumption was made in a study in the literature that a low recovery ratio and a high viscosity were found to be favorable to achieve surface smoothness on printed lanthanum and iron co-doped strontium titanate (LSTF) ceramic films [103]. However, this is an assumption based on comparisons of a few LSTF pastes within the study, which cannot be generalized and may vary in different batches under different printing conditions.



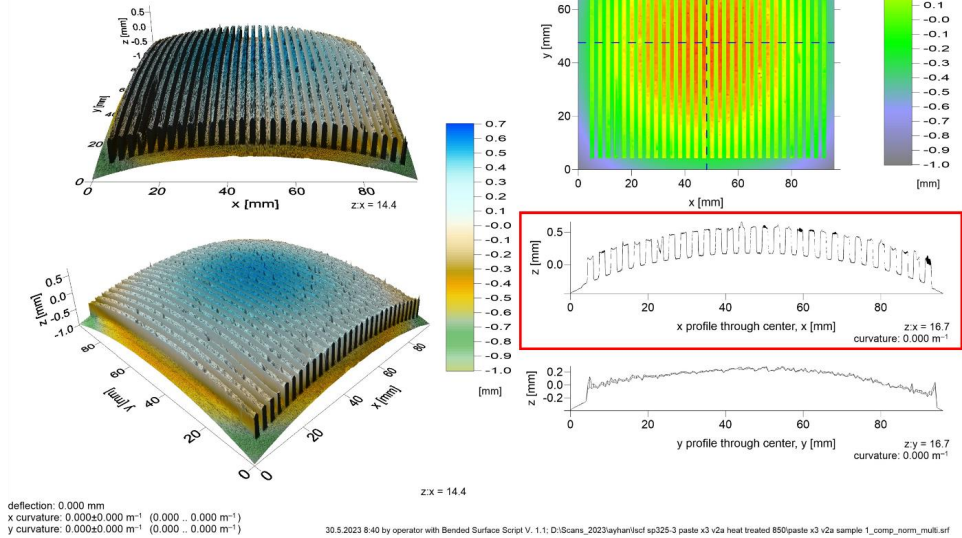
**Printed ribs on Elcogen cell - heat treated @850 °C**9601 x 193 pts 96.000 x 96.000 x 1.708 mm (step z/ize: 10.00 x 500.00  $\mu\text{m}$ )

Figure 26 Printed and heat-treated stripes under white light topography. Highlighted area with red rectangle to show surface roughness of the ribs

According to the functionality of cathode contact layers in SOFC stack systems, in addition to electron conduction, gas transport is also critical, which is provided by a coarse microstructure. Therefore, the porosity of the heat-treated ribs was calculated using Image J/Fiji from a microscopy image. A porosity of  $25\% \pm 8\%$  was found, which can be further improved. While K. Sick et al. [79] mentioned that the coarse-structured LSCF cathode contact layer is a suitable contacting for SOC Jülich stacks, J. H. Zhu et al. [104] claimed that the sintered LSM reaching 45% porosity is beneficial for a cathode contact layer.

Moreover, secondary phases were detected in the microstructure, where inclusion-like phases in white color can be seen in detail in Figure 25-b. According to the EDS results, it is found that these are cobalt oxides (CoO) as residual oxides left from the synthesis process of the spray-drying powder and have not reacted to form perovskites. A similar situation was experienced at LSM when manganese oxide (MnO) was found as a residual oxide by colleagues using this in-house synthesized perovskite material. Additionally, it is discussed that these remaining oxides do not harm the functionality of CCL since they are not massively distributed in the structure.

### 5.3.3. Study of the rheology for paste X3v2

For successful printing, the rheology of the pastes reveals how the pastes behave under measurement conditions in a rheometer. This can be attributed to the printing process and helps to predict whether the

paste will work during printing or not. As an example, R.R. Lathrop [105] defined in the literature some factors that influence the printability of the paste and one of them is the rheology. On the other hand, it would be helpful to define the meaning of a "working paste". This means not only that the rheology of the paste appears to be adequate for printing, but also that the printing results should be as desired. In this context, the rheology-printability relationship has been highlighted by D. A. Rau et al [106]. In the context of this relationship, the evaluation of rheological results should be application specific, i.e. what paste behavior is required, how printing works and what printing results are needed. For example, printing approximately 500  $\mu\text{m}$  thick stripes with a gap in between can easily lead to a sagging problem if the paste does not provide a specifically higher structural recovery performance after printing.

The shear rate vs. viscosity plot (Figure 27-a) indicates the flow behavior of the paste X3v2, and the viscosity decreases with increasing shear rate indicating that the paste has a shear-thinning behavior. It is beneficial for this work that the paste should flow and pass through the apertures of the stencil during printing with a force applied by the squeegee. The paste is also stable at rest, as evidenced by the lack of a zero-shear plateau at lower shear rates.

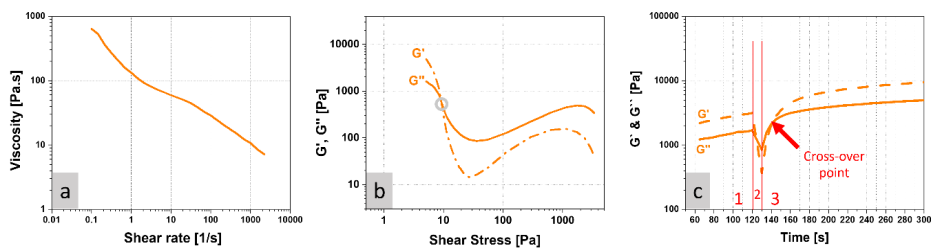


Figure 27 Results of rheology measurements for paste X3v2 showing a) flow curve, b) viscoelastic behavior, and c) time-dependent behavior

The existence/strength of the three-dimensional structure within the paste can be evaluated by an oscillatory test. The yield point is the point at which structural breakdown begins and is an indicator of the presence of viscoelastic behavior. At the cross-over point in the shear stress vs  $G'$  and  $G''$  plot is shown in Figure 27-b,  $G' > G''$  (dominance of solid-like behavior) turns into  $G'' > G'$  (dominance of liquid-like behavior), which is the yield point with the value of about 10 Pa. It is difficult to define in real application how much shear is applied by the squeegee during printing, but the paste will structurally break down after the yield point and will flow during printing with enough shear applied. This value is useful for making comparisons with other pastes.

The Time vs.  $G'$  and  $G''$  plot shown in Figure 27-c for the 'Paste X3v2' has three intervals. In the first interval, the paste is at rest. At the second interval, high shear is applied, which means it represents the printing process. This is the exact reason why a transformation from solid to liquid state takes place. At the third interval, the printing is already done and the paste behavior can be observed how it behaves and how fast it recovers. It takes 10-15 seconds to reach the crossover point where the paste is in a solid state again. Subsequently, the storage and loss modulus show an increase than the first interval over the test

of almost 700 s (up to 300 s are shown in the plot for better visualization of the cross-over point). This recovery trend on the paste means that the viscosity increases over time during the paste is at rest right after the printing. This rebuilds the ruptured structure and helps to print relatively thick shapes without sagging, i.e. about 500  $\mu\text{m}$  thickness was reached in this work.

The trend of paste recovery explained above may be mixed with the term "rheopexy" which is not well known, but has been used and studied in the literature [107–109]. It is defined as a reverse effect of thixotropy and explained as "an increase in viscosity with time at a constant shear rate" [107]. At the third interval of time-dependent behavior (see Figure 27-c), this viscosity increase can be observed by an increase in both  $G'$  and  $G''$  over time. However, the third interval represents that the paste is at rest after shear is applied at the second interval and therefore the shear applied at the third interval is almost zero (0.1 1/s), which does not match with the definition of rheopexy behavior. Furthermore, despite the fact that the recovery of the paste takes 10-15 sec. (not a quick recovery), the structural build-up was maximized by using a rheology aid that is also in agreement with the literature [108]. The relatively slow recovery time was compensated by using the stencil as a mold, as explained earlier in this chapter.

#### 5.3.4. Effect of dispersant and PSD on paste behavior with respect to printing results

Successful printing is based on several factors. Two of them are highlighted in the literature [98,110,111]:

- Use of a dispersant as a rheology additive
- Achieving different particle sizes within the paste

In industry, i.e. the coating industry, for products such as paints and slurries these factors have been considered and found helpful to control the paste behavior in order to achieve desired printing results. Within the framework of this thesis, the challenge was the same: "How to control the paste behavior?".

Compared to the former employee's paste and most of the LCC2-containing pastes, the above-suggested two main factors were considered for paste X3v2. The dispersant was chosen to generate a three-dimensional structure. It has a direct effect on recovery and particle-particle interactions. When shear is applied, particles interact in the direction of flow, and particle size plays a role in both viscosity and paste behavior (discussed in detail: paste P6 in Chapter 4).

The two factors mentioned above were applied to the paste at the same time, so it is not known which one has a greater effect on the successful printing results. Comparisons between pastes may provide a better understanding and help to distinguish the effects of these two factors. Therefore, the following comparisons were made:

1. The recipe of paste X3v2 has been adjusted by removing the dispersant. The rest is the same in the recipe while the PSD remained similar (see Figure 28-c and -d) and it is called OSB-c. This adjusted paste was characterized, also printed, and compared with the results of paste X3v2.
2. The recipe of paste X3v2 was adjusted two times. One batch contained two minutes of ball-milled powder; the other batch contained 2 hours of ball-milled powder. The new two pastes were named OSB-a and OSB-b, respectively. As in the last example, the whole characterization steps and the comparison were performed.

For the sake of simplicity, all the adjustments were made based on the paste X3v2 recipe, even though the reality of "each paste is unique" was known. Not only the wettability of solid contents may vary, but also the binder and dispersant with solvent amount may vary according to the changes in any recipe. Nevertheless, everything in the paste formulations other than the changed factors was kept the same and the characterization of the pastes has been done. As a result, some significant changes in either paste behavior or printing results were observed.

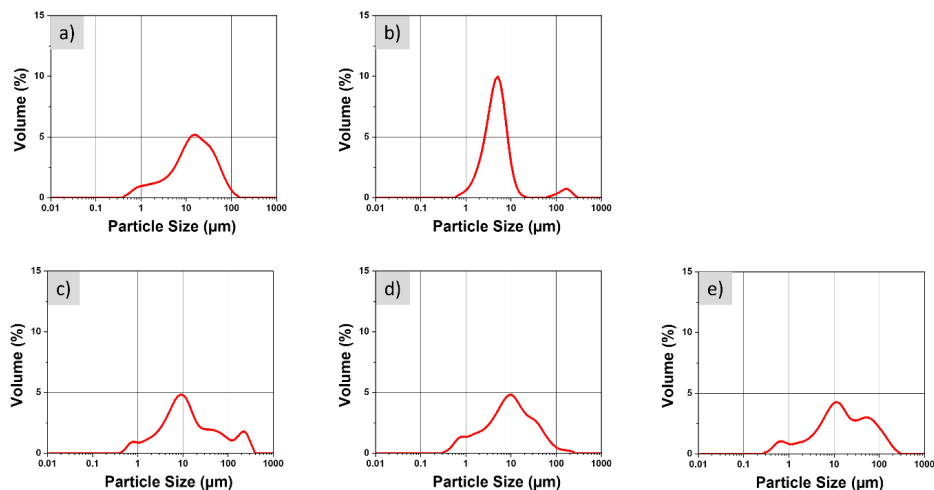


Figure 28 Particle size distribution of a) OSB-a, b) OSB-b, c) OSB-c, d) Paste X3v2, e) Paste X1. Paste formulations can be seen in Table 8

In the first example, the shape characteristics of the printed ribs were directly changed when the dispersant was removed. There was a dominant effect on the printing results. A dome-like shape was observed with the OSB-c (shown in Figure 29-b) similar to other pastes that do not contain the dispersant (see Figure 18 in Chapter 4 and Figure 37-b in Chapter 5). The importance of a 3D-connection-generator dispersant can also be seen in the rheology results. In the shear stress vs.  $G'$  and  $G''$  plot (Figure 30), the yield point of OSB-c (highlighted with a green circle) is less than 2 Pa while paste X3v2 has ca. 10 Pa. This shows that OSB-c will flow earlier under shear than paste X3v2, indicating the strength of the paste structure.

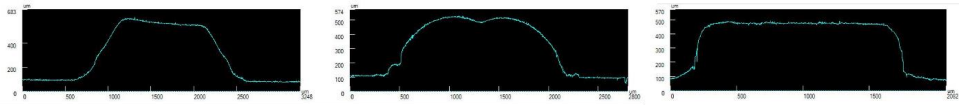


Figure 29 Printed and dried ribs under laser microscope with profile mode; from left to right OSB-b, OSB-c and Paste X3v2 (the latter is included here for ease of comparison)

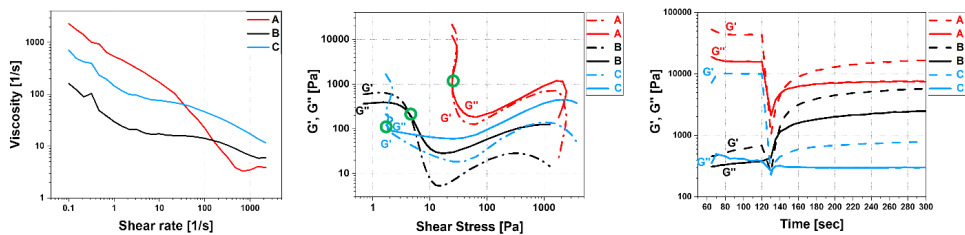


Figure 30 Rheological characterization of prepared pastes of OSB a, b, and c. From left to right: Plot of flow curves, viscoelastic behavior, and time-dependent behavior

In the oscillatory step test (plot of time-dependent behavior in Figure 30), storage modulus decreases from the first to the third interval for OSB-c different from paste X3v2, which shows a structural build-up. It indicates that the internal structure of OSB-c after printing gets weaker and flows until it is solid again showing thixotropy which is not helpful for the aim of this work.

Behind the major effect of the dispersant on paste behavior and the shape characteristics of printed ribs, the importance of particle size can be discussed in the second example. Two paste formulations containing dispersants with different PSD changes yield stress values and paste behavior that ultimately affect the printing results. OSB-a shows thixotropy and higher yield stress (25 Pa) than paste X3v2. Its particle size is distributed in a wide range similar to the PSD of Paste X3v2, however, it contains a higher number of larger particles that result in a great increase in viscosity, which is in agreement with the literature where the effect of particles on flow behavior is also highlighted [112]. Due to the large particles provide resistance against flow, the yield point is higher on this paste with the consistency, which is thick as play dough, therefore it is not suitable for printing.

OSB-b continues to show a full-recovery behavior with a changed yield point (ca. 4 Pa), which is still the closest one to paste X3v2 among the other two adjusted pastes (see the plot of time-dependent behavior in Figure 30). According to the PSD results, d50 became smaller and the distribution range became narrower and it is different than what paste X3v2 shows. Similarly, Yoo and Rao [113] reported that a wide range of particle sizes has higher viscosities than those with narrow particle sizes in concentrates. Despite the differences in particle size and particle size distribution, the printing result of this paste (OSB-b) is the closer one related to the characteristic of the printing shape.

In both examples, the differences in particle size were not able to change the character of the printing results as much as the presence/absence of the dispersant.

### 5.3.5. Mono- and poly-modal PSD effect on the paste behavior with respect to printing results

Paste X3v1 is the modified version of paste X3v2. Instead of adding 2 minutes and 2 hours of ball-milled (BM) powders as in paste X3v2, 30 minutes and 2 hours of BM powders were added to paste X3v1. The rest was kept the same, so only one element was changed compared to the reference paste - paste X3v2 - for the sake of easy comparison. However, the consistency of the paste X3v1 was way thinner than the reference one. The BET-specific surface area results of the added powders (see Table 7) and the rheology results (see Figure 31) are also in agreement with this.

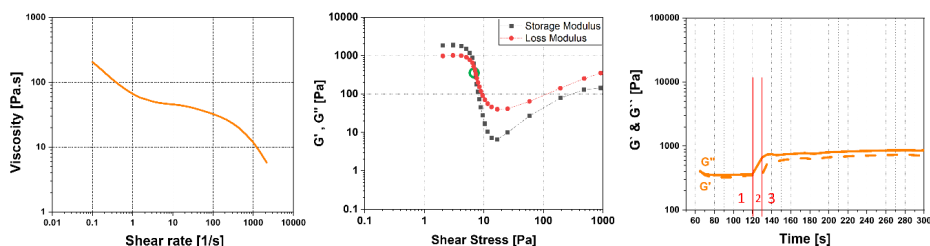
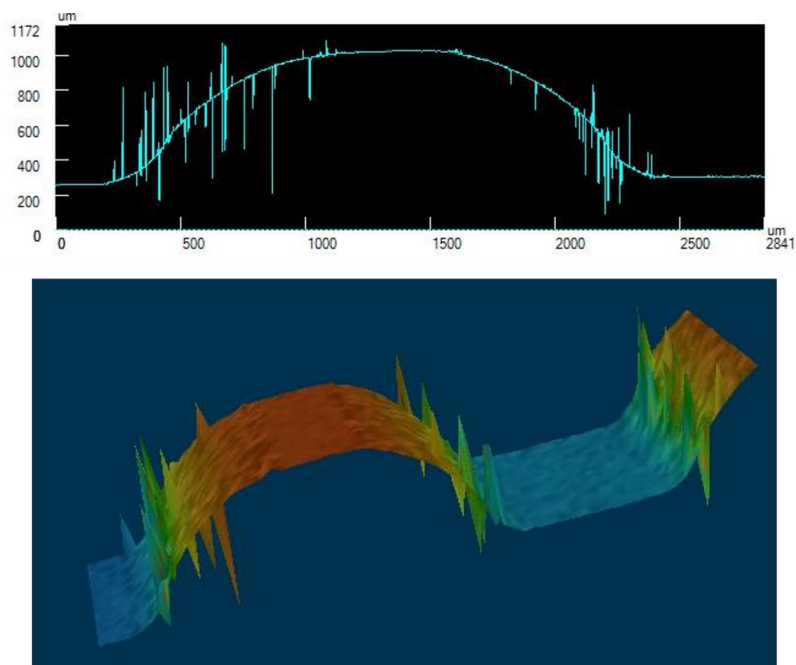


Figure 31 Rheology of paste X3v1 - From left to right; Flow curve; Viscoelastic behavior; Time-dependent behavior

Adjusted paste X3v1 contains powders with more surface area than the reference paste and it is an indicator for the addition of some more binder. With the addition of more binder, other contents are required to normally be also adjusted. However, the aim was not to find a suitable paste for the desired printing results due to the already improved/engineered paste recipe of paste X3v2. Therefore, mono-modal vs poly-modal PSD was under these conditions compared in terms of rheology and printing results.

The modified paste has lower viscosity according to the flow curve in Figure 31, where the yield point is smaller than the reference one, as shown in the viscoelastic behavior graph. This means that the internal structure is weaker and the paste flows more easily than the reference one. The time-dependent behavior gives an important hint that the printing process will not work properly due to the dominance of liquid-like behavior over solid-like behavior at all intervals, even at rest. Therefore, the paste can be described as a viscoelastic liquid. However, the thickening behavior exists with the presence of the dispersant in the paste. This can be seen from the increase of  $G'$  and  $G''$  from the 1<sup>st</sup> to the 3<sup>rd</sup> interval, which imparts that the structural build-up can take place but is limited by the lack of a structural recovery (no cross-over point at the third interval). This could be due to the poor particle interactions. Consistent with this explanation, a small surface flatness was observed at the top of the printed rib as seen in Figure 32 due to the limited structural recovery despite the presence of the dispersant. The rest of the printed rib has a dome-like shape due to the sagging behavior of the paste.



*Figure 32 Characterization results of printed paste X3v1 under laser microscope in profile mode*

As can be seen in Figure 33, the PSD of paste X3v1 became narrower and mono-modal than a wider and poly-modal PSD of paste X3v2 (see Figure 28-d). According to Khecho et al. [114], moving from a wide bimodal to a narrow unimodal distribution improves the shear thinning behavior with the deposition process in printing. This trend is observed for the application of the direct ink writing process and is in contrast to the results obtained for paste X3v1. However, it is known that the PSD affects the packing ability of the particles in the suspension, where the viscosity reduction depends on the particle size ratio reported by Greenwood et al. [115]. The decrease in viscosity with the paste X3v1 can be explained by the fact that the packing ability of the particles was increased with the addition of smaller particles (30 minutes of BM powder) rather than larger ones (2 minutes of BM powder), which led to a decrease in viscosity.

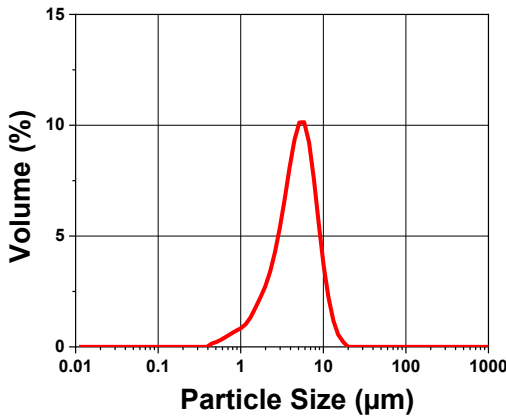


Figure 33 PSD of paste X3v1

#### 5.3.6. Printing of different rib-channel designs

Stencil No. 2, shown in Table 9, contains four different rib-channel designs for 20 mm to 20 mm substrates. The idea was to print these different designs with paste X3v2 to determine the best-performing design by electrical characterization. The nonconductive material of yttria-stabilized zirconia (YSZ) substrates was chosen for electrical measurements. Printing of the latter paste was performed but failed due to a massive sagging problem after printing. This is due to the change in surface properties from porous LSCF substrates to dense YSZ. The tackiness of the paste was missing and needed to be improved in order to increase the adhesion ability of the paste to adhere to the surface of the YSZ substrate.

Paste X4 was prepared by adding ethyl cellulose as a binder with a longer chain length (45 cP), different from other pastes listed in Table 8, to achieve tackiness on the paste. By increasing the chain length, the chains become more entangled and stick together better, making the bonds stronger against applied shear. Additionally, more transport agent was added than what is contained in paste X3v2 to ensure that the adhesion of the paste is increased.

Printing was performed with paste X4, which adhered to the surface as expected. However, the print quality was low due to the higher surface roughness at the top of the ribs (see Figure 34). Paste X4 requires more adjustment as well as a printing process to achieve surface flatness. However, it was not studied further due to lack of time.



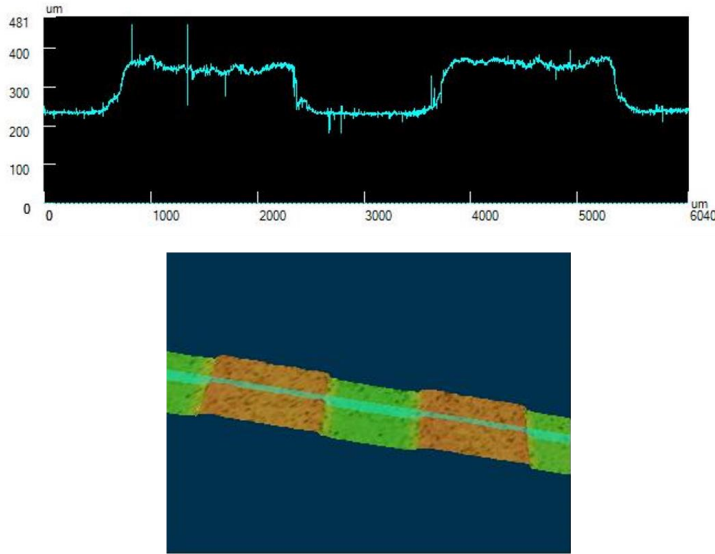


Figure 34 Characterization of printed and dried rib of paste X4 under laser microscope in profile mode

#### 5.3.7. Study of printing parameters

It can be seen that some parameters are different between Print 1 and Print 2 (see Table 10). The snap-off distance was reduced to 0 mm to be able to use the stencil openings as a mold. LP thickness, which is equal to the thickness of the substrates, did not change. Squeegee pressure increased drastically to be sure that the paste would structurally break down during printing. The recommended pressure is 1-3 Pa as mentioned in a study [59]. Another parameter related to the squeegee is its speed. The speed was decreased to see the rolling movement of the paste during printing, which is the quality level for the paste experienced after printing so many different pastes. The speed of 20 mm/s is also in accordance with the recommended value in the literature [59]. The separation speed was doubled in order to speed up the process since a waiting time of 20 seconds slows down the process.

The desired printing results were obtained under Print 2 conditions, but no other parameters were tried to see what changes would occur. The effect of different printing parameters on the printing results was studied in Chapter 4 (4.3.3.).

#### 5.3.8. Reproducibility of paste X3v2 with desired printing results

Reproducibility of the entire paste preparation and printing process was performed twice. In the first attempt, the desired surface flatness was not achieved on all printed stripes, however, the second attempt was successful, as can be seen in Figure 35-b, and compared with the results of the reference paste published again in Figure 35-a as well as Figure 24-a. To understand the reason and to carefully evaluate

the whole process, the term "reproducibility" was divided into two parts: Paste behavior and printing results.

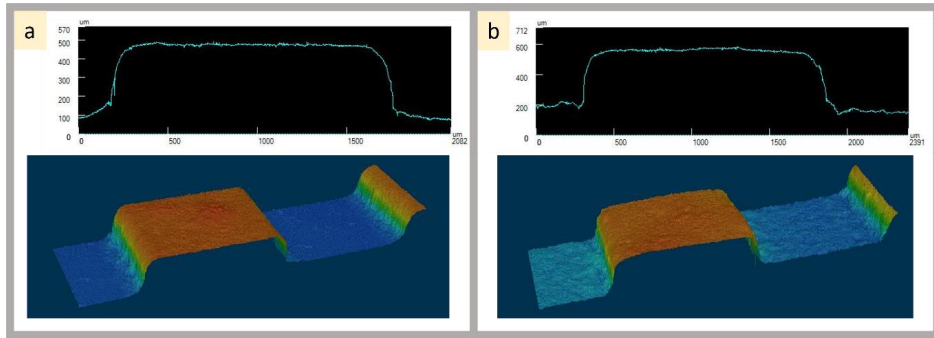


*Figure 35 Characterization of printed and dried ribs under a laser microscope in profile mode, a) original one, b) reproduced*

In terms of paste behavior, the rheological results of the two reproducibility trials were compared with the results of paste X3v2. There are slight differences such as the value of the yield point seen in the plots of viscoelastic behavior in Figure 36-a and -b (ca. 7 Pa for the reproductions and ca. 9 Pa for the reference paste). The structural recovery for both attempts also seems to be similar to that of the reference at ca. 10 seconds as shown in the same figure. This means that the paste preparation step worked for both reproduced pastes.

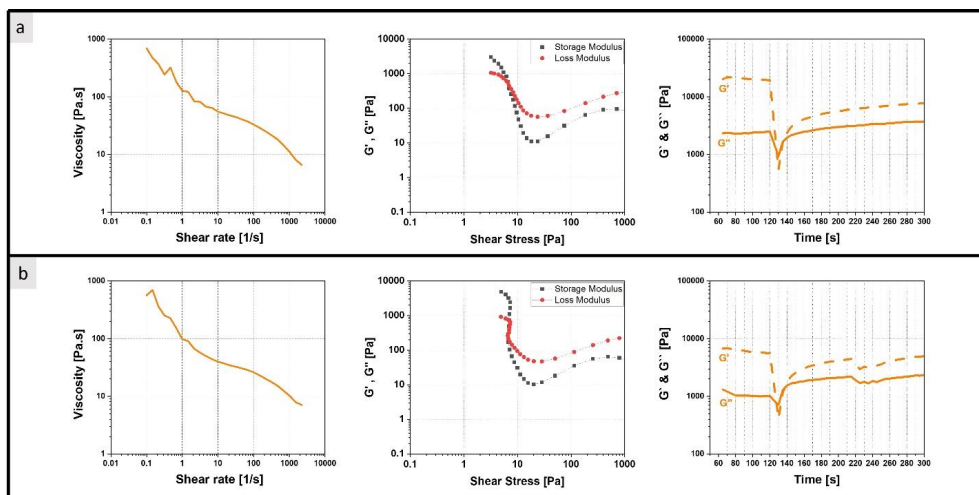


Figure 36 Rheologic characterization of reproduced paste X3v2 with a) first attempt and b) second attempt, and from left to right the same for a and b: flow behavior, viscoelastic behavior, time-dependent behavior

One successful and one unsuccessful print point out that the printing process needs to be on focus. Since the printing parameters were always the same, any other parameters that are intermittent should be considered. These could be environmental effects that have not yet been considered or a user effect due to the semi-automatic screen printer. Temperature differences in the laboratory just before the printing could be a possible reason that could affect the viscosity. On the other hand, there are some parts of the screen printer instrument that need to be set by hand, i.e. fixing the height of the squeegee, which affects the gap between the stencil and the squeegee. This may influence the pressure applied to the paste during the printing, which could be another reason for not achieving surface flatness. Thus, it has been seen that the variable parameters need to be fixed to overcome conditional reproducibility.

### 5.3.9. Reproducibility attempt with old paste

A former employee of IEK-1, Dr. David Udomsilp, suggested that the rib-channel form could be printed directly on solid oxide cells with the goal of both avoiding a machining process on the metal interconnect to make gas channels and improving the contact between cell and interconnect to increase stack performance.

He prepared and printed some cells as these are very early results and achieved some surface flatness as shown in Figure 37-a. His recipe, which was in accordance with the internal LSCF cathode fabrication route, I tried to reproduce, but it never worked. The characteristic of the printed shape was dome-like.

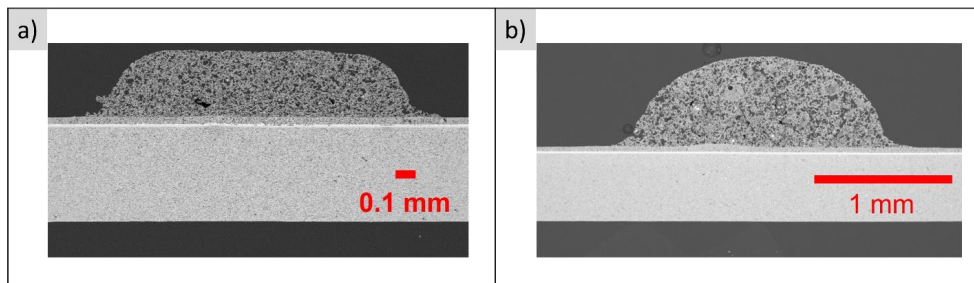


Figure 37 SEM images of printed and heat-treated ribs; a) from Dr. Udomsilp's work, b) reproducibility experiment

Possible reasons why it did not work out;

- Different batches of spray-dried powders were used as solid content. For each different batch, particle size values vary
- He printed his paste by hand in the screen-printing instrument with the squeegee (see Table 9 No:1). User effect on printing parameters matters
- Environmental conditions were not considered in his prints and my reproducibility attempts. Temperature affects the viscosity of the paste

The major effect may be due to differences in particle size. The same amount of powder could not be wetted by the same amount of liquid according to Dr. Udomsilp's recipe. The BET-specific surface areas of both powders were slightly different (see SP 319-1 in Table 7), which also indicates that it is difficult to get the same recipe and the same results.

In his preparation route, all ingredients were ground and mixed by 3 roller mill, and raw powder was added and also mixed by a centrifugal mixer which has no effect on grinding. A poly-modal PSD with possible agglomerates may be obtained (no data). The important point here is that the agglomerates (if present) in the paste may help to stop the flow after printing and contribute to the surface flatness of the printed ribs at the end. In this regard, it has been mentioned in the literature that the strength of the aggregates has a strong influence on the behavior of the paste [116].

Although the same preparation route was followed for the reproduction attempt, a different recipe was finally obtained due to the different wettability of the powders. The paste contains a polymodal particle size distribution (see Figure 28) and shows a dome-like shape under the electron microscope (see Figure 37-b). Printing results were characterized. This characteristic shape of the prints is similar to other prints where the pastes used (studied in this PhD thesis) do not contain a dispersant.

Overall, the user effect may have some influence; however, a major effect may come from the paste behavior. This is directly related to the paste formulation. The temperature effect can change the viscosity before printing and thus can have another effect on the paste. In addition, how Dr. Udomsilp achieved this surface flatness can be answered with a formulation: the paste was printed with the right consistency under the right environmental conditions at the time of printing.

## 5.4. Chapter conclusion

According to the aim of this dissertation, ceramic ribs with ca. 500  $\mu\text{m}$  thickness with promising surface flatness and edge cavity were successfully fabricated by stencil printing, which is rarely known and used in the field of ceramics. It is the first time in the literature that such a thick ceramic stripe has been printed by this method.

The printing is based on several parameters, from the preparation of the paste by choosing a suitable recipe to the printing of the paste with adequate printing parameters. Within this complexity, three points have been defined and discussed as success factors:

- The existence of a yield point for the paste imparts viscoelasticity within the paste structure. It was observed in the shear stress vs.  $G'$  and  $G''$  plot that paste X3v2 provides structural degeneration with the applied shear. The paste flows during printing, filling the openings on the stencil, and then recovers its structure to maintain its given shape after printing.
- Achieving a full recovery behavior of the paste after printing and well evaluating the recovery performance through a three-interval thixotropy test was the second success factor. Structural build-up means that a ruptured structure rebuilds itself (transformation from liquid-like to solid-like behavior) to retain the printed shape detected via plots. The recovery time of the paste was 10-15 seconds.
- Consideration of the recovery time of the paste on the printing action that brought the surface flatness without sagging. The recovery time is the time required for the paste to reach the solid state after flowing. Therefore, the printing was manually stopped for 20 seconds after printing and then the separation of the substrate from the stencil happened.

As seen above, the rheological characterization of pastes plays a crucial role, firstly to predict if the paste will work according to the aim of the printing, and secondly to adjust the parameters in the printing process to achieve the desired printing results. Therefore, paste X3v2 was used as a reference for further comparisons of different pastes to understand the effect of the dispersant used and different particle sizes with their distribution on the paste behavior in terms of printing results. The dispersant used in this work as a 3D structure generator changed the characteristic of the rib shape. Particle size and its distribution influenced the viscosity behavior of the paste and affected the shape of printed ribs.

Reproducibility of paste X3v2 and printing results were studied and it was found that it is conditionally reproducible due to the lack of consideration of environmental factors, i.e. temperature, humidity, also the observation of the user effect with a semi-automatic instrument used for printing. It is assumed that this conditional reproducibility will be transformed into permanent reproducibility by controlling the mentioned factors for the case of mass production in the future.

## 6. Evaluation of the novel idea

### 6.1. Novel idea: How much is it going to contribute to the stack resistance?

It is necessary to look at the novel idea from a different perspective to analyze or even criticize it, which will definitely open new doors to improve it.

A relatively thick layer with a rib channel design is implemented on the cell, which might increase the stack resistance after assembly, causing performance loss, while massive research in the SOC field is going on to reduce the stack resistances.

The first point is the interconnect. Its thickness may decrease since there will be no machined gas channels in the height of 1.5 mm. However, the conductivity of a metallic interconnect (Crofer22APU: 8700 S/cm at 800 °C [79]) is much higher than that of a ceramic layer (LSCF: 100-200 S/cm at 800 °C [79]), so the contribution of the metallic interconnect to the stack resistance can be accepted as negligible.

Second, the thickness of the cathode contact layer in the conventional design is 150  $\mu\text{m}$ , and it will be 500  $\mu\text{m}$  in the novel design.

A rough one-dimensional calculation was made to see the increase in area-specific resistance (ASR) on the ceramic layer and compare it to the stack resistance. Equation 6 shown in Chapter 2 was used. The measured area was assumed to be 1  $\text{cm}^2$  for both cases, and the conductivity value for the LSCF was assumed to be 100 S/cm.

The ASR of 150  $\mu\text{m}$  thick LSCF is 0.00015  $\text{ohm.cm}^2$ , while the ASR of 500  $\mu\text{m}$  thick LSCF is 0.0005  $\text{ohm.cm}^2$ . On the other hand, Jülich's internal ASR value for a single cell SOFC measurement at 800 °C is 0.233  $\text{ohm.cm}^2$  (at 0.5 A/ $\text{cm}^2$ ). As another example from the literature, the ASR of an SOFC stack at 700 °C is 0.25  $\text{ohm.cm}^2$  [7]. These values show that increasing the thickness of the ceramic layer resulted in an order-of-magnitude increase in ASR. The new ASR value of 0.0015 with the new design is two orders of magnitude lower than the stack/single cell ASR value at 700 - 800 °C. Thus, it can be seen from the rough ASR calculations that the thickness increase of a ceramic layer due to the implementation of the novel design idea should not be an issue. It can be very well compensated by the increased contact area in the air-side contact, which increases the stack performance. This can be seen after a stack test is performed.

### 6.2. Rib-channel design: What are the best rib-channel widths?

A numerical approach, which is useful for cost and flexibility reasons, can be used to find the optimal rib-channel widths, as was done by H. Geisler in his PhD thesis [117]. Finite element modeling (FEM) was used to predict the effect of different model geometries on stack performance. He has focused on different geometries at the interconnect and these results can be used to optimize the rib-channel design as a ceramic cathode contact layer. Some points from his study:

- Narrow RPU (half of the sum of the width of a channel and a rib) with thick ribs is beneficial, however, there is no optimal rib/channel ratio given, which depends on the ASR of the contact, which is influenced by several parameters such as temperature, thickness of ribs and cathode

layer. For example, with an increase in the thickness of the latter, the performance of the LSCF-based stack layer increased, which is shown in his work.

- Related to finding an optimal rib channel width (mentioned in the literature by the same author [8]); if the rib width is rather small ( $<1$  mm), the power density decreases due to the small contact area causing a high contact resistance; if the rib width is wider ( $>2$  mm), all ohmic and polarization losses in the cell increase. On the other hand, the applied parameters such as conductivity, porosity, tortuosity, cathode thickness (as mentioned above), etc. vary the optimal design.
- The role of microstructure was also taken into account on cathode contact layers. The advanced design in his work, which is similar to the novel design in this work, functions best with a 0.6 pore volume fraction and more than 200  $\mu\text{m}$  thickness at 800  $^{\circ}\text{C}$  operating temperature.

As a starting point behind these predicted results and assumptions, the printed design (1.5 mm width for each rib and channel) was kept the same as the conventional one in terms of interconnect sizes, so that stack test results become comparable between novel and conventional design. At this point, whether the novel design values with a thickness of a half millimeter is enough for a sufficient gas flow or not was calculated by Roland Peters (IEK-9) through pressure drop calculations, and the value was 20 hPa which was attributed as an acceptable value to go for the design.

### 6.3. Four-point probe (4PP) measurements

4PP measurements were performed separately for a stencil-printed rib of LSCF (paste X3v2) and a screen-printed LSCF cathode layer (standard Jülich paste) printed on alumina. Figure 38 shows their setup.

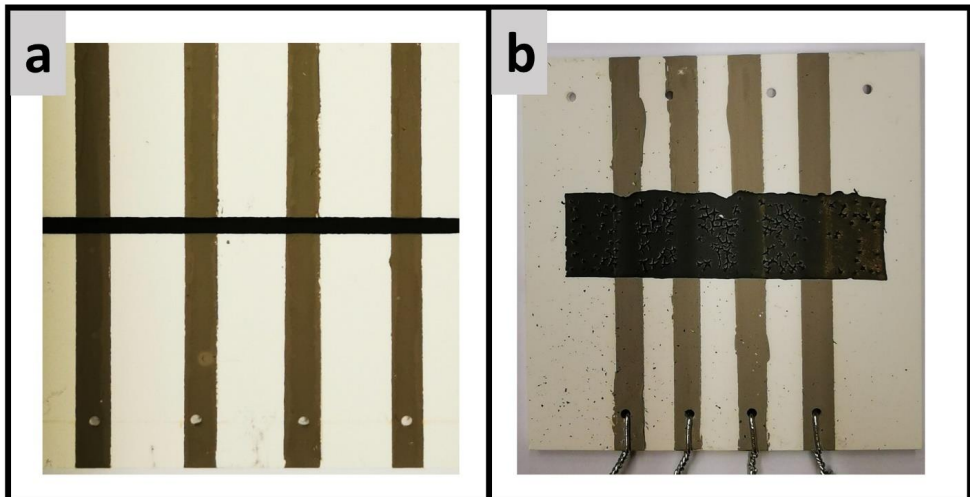


Figure 38 a) Stencil-printed LSCF rib and b) screen-printed LSCF cathode on a porous alumina substrate which was drilled for the wire contact

There are two approaches to these 4PP measurements:

- 1) Calculation of the conductivity values of these layers.
- 2) Consider the movement of electrons through the ribs of the cathode contact layer (CCL) and the cathode layer, where in-plane resistances may occur, resulting in the loss of electrochemically active regions. A FEM simulation can be very helpful to make predictions about the rib channel design used.

After the measurements, the I-V curves of the two samples were plotted, as shown in Figure 39. Their slopes were also calculated and written on the plots as resistivity values ( $R=V/I$ ). These values were further used in equation 6 to find the conductivity values of the samples. The effective conductivity for the LSCF rib (L: 0.8 cm, A: 0.01 cm<sup>2</sup>) after calculation was about 5 S/cm, and for the cathode layer (L: 0.46 cm, A: 0.004 cm) was 84.5 S/cm. The cathode layer has a higher conductivity than the CCL, which may result in a lower in-plane resistance on the cathode layer, where electrons can be conducted faster. The lower conductivity of CCL may be related to the microstructure, where electron path can be prevented in the microstructure.

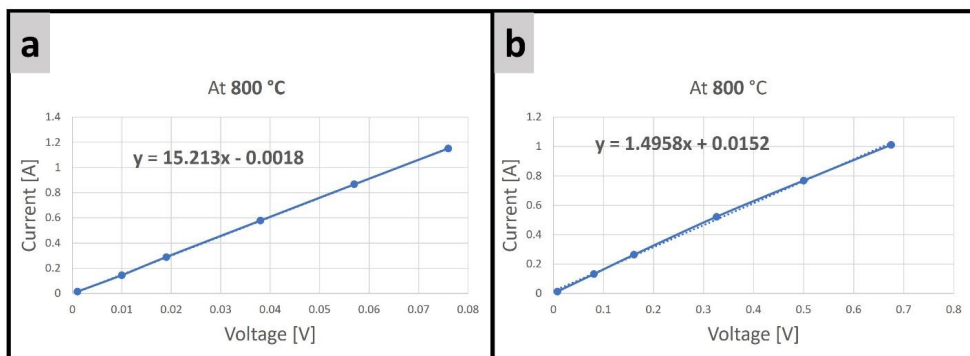


Figure 39 I-V curves of both a) stencil-printed LSCF rib and b) screen-printed LSCF cathode on the porous alumina substrate at 800 °C

## 6.4. Cell assembly

The printed and sintered stripes from the successful paste (paste X3v2) have been characterized via confocal microscopy and white light topography to prove the surface flatness and the height distribution of the prints. Although white light topography showed a promising height distribution in terms of height homogeneity, which is important for cell assembly, a precise measurement would be beneficial because complete cells used as substrates have a bending that can reduce the accuracy of results obtained with one-sided measurements. Both side measurements with the same instrument after an accurate setup can be beneficial.



Regarding the design approach in a stack system, the sealant at the edge of the cells and the bipolar plates used should be well suited to the novel design due to the increased height of the CCL and its height distribution.

Mechanical strength is another issue to consider when evaluating the printed ribs. During cell assembly, a load is applied where the sealant absorbs most of the load and the rest is on the ribs. It is difficult to determine the proportional load distribution on both the sealant and the ribs, but the latter should be able to remain without an issue. Therefore, as a first step, a very simple test, an adhesion test, was performed with adhesive tapes. Two different tapes were applied to the surface of the ribs and then removed from behind as shown in Figure 40. No pieces came out with one type of tape and only one piece came out with the other. Thus, the printed ribs look stable for a cell assembly.

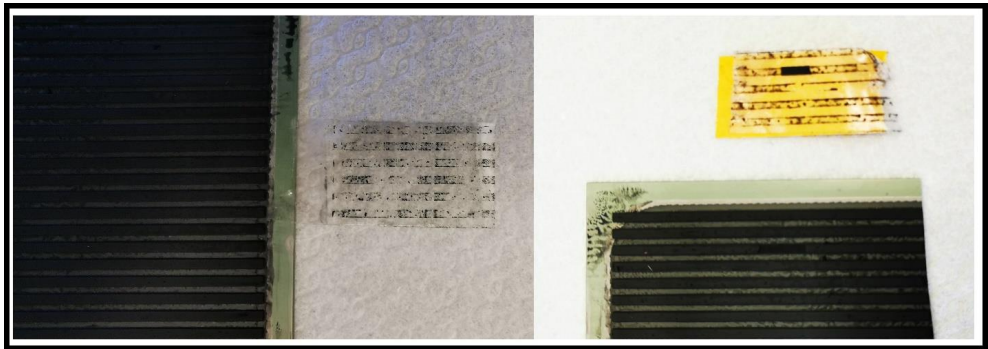


*Figure 40 Tape adhesion test on printed and heat-treated ribs*

## Summary

A need for improvement on the air side of SOC stacks was realized through a novel idea which is stencil printing of a rib-channel design on a cathode surface. It required a detailed investigation for an adequate paste formulation including a suitable rheological behavior and well-adjusted printing parameters. With these considerations in mind, two perovskite materials (LCC2 and LSCF) were used and investigated in the paste preparation process.

LCC2 was used more to trial the whole printing process and to study the influence of the parameters within the process on the paste behavior and the printing results. During the trials, the binder content and solid loading within the paste batches were adjusted, but only the paste consistency was affected, without changing the rheological behavior of the paste, which resulted in either printing failures, i.e. stencil clogging, or undesired printing results, i.e. dome-like shape.

Further literature research was done and the lack of 3D connection within the internal paste structure was realized on the already existing pastes, which became a cornerstone that the paste recipes were revolutionized by adding rheology additive and changing the PSD. The stencil printing parameters were also adjusted. These changes made it possible to improve both the paste rheology and the shape of both LCC2 and LSCF prints.

The desired results on printed ribs with promising surface flatness and edge cavity were achieved with LSCF-containing paste. Therefore, special importance was given to understanding of the paste rheology and its integration with the printing process coupling with the printing parameters. It was found that three points played the most important role in achieving the successful results:

- The existence of a yield point, which is a sign of viscoelastic behavior,
- The existence of a fully structural build-up on the paste after printing and the evaluation of the time-dependent behavior plot for the recovery time,
- Consideration of the recovery time as a printing parameter during the printing process.

Reproducibility was conditionally achieved due to changing environmental conditions, i.e. temperature, and the user effect, i.e. setting up a semi-automatic instrument.

The evaluation of the novel idea was also studied. Its contribution to the cell resistance was roughly calculated, the best-performing rib-channel design was discussed using some results from a literature study, the mechanical strength of the printed ribs was tested using adhesive tapes, and four probe point measurements were performed to characterize the printed ribs electrically.

## Outlook

The reason for applying a novel design to the air-side contacting part of SOCs is to improve the performance of the SOC stacks. For this straightforward aim, a stack test of cells with the novel design will be performed and then compared with the results of a stack with the conventional design, holding other factors constant. If the performance is the same or even better, the novel design will be applied to the Jülich stacks, allowing more efficient stacks to be manufactured in the future. This will then bring the cost-effectiveness that can be achieved due to the need for fewer repeat units reaching the same energy output of stacks with the conventional design.

In cell assembly, component design has eminent importance for reliable stack construction. Sealing and interconnects are adapted to the novel design due to the increased thickness. Deviations in the height distribution of the ribs will be taken into account in the design of the latter components by a design team at Forschungszentrum Jülich, so more precise height distribution of the ribs will be provided by both-side white light topography measurements to support the design team.

Another point is related to the best-performing rib-channel design with regard to materials selection, and microstructural effect (coarse or grain). The design is important to eliminate/reduce in-plane resistance. Therefore, the width of channels and ribs should be well considered. The results of 4PP measurements for LSCF cathode and LSCF cathode contact layer (CCL) can be used in the future for FEM modeling to predict an optimal rib-channel design specifically for Jülich stacks under their specific operating conditions.

The selected materials play a crucial role in terms of their conductivity and coefficient of thermal expansion. Conductivity will fulfill one of the requirements of the CCLs, i.e. the collection of electrons from the cell. A matched thermal expansion will increase the durability of the layers in the cell under thermal cycling. Another state-of-the-art material LSC (lanthanum strontium cobaltite) will be also printed, characterized, and evaluated in the future.

## List of abbreviations

2D	Two-Dimensional
3D	Three-Dimensional
3ITT	Three Interval Thixotropy Test
4PP	Four-Point Probe
ASC	Anode-Supported Cell
ASR	Area-Specific Resistance
BET	Brunner-Emmett-Teller
BM	Ball-Milled
BSE	Backscattered Electrons
CAPEX	Capital Expenditure
CCL	Cathode Contact Layer
CTE	Coefficient of Thermal Expansion
EC	Ethyl Cellulose
EDS	Energy-Dispersive X-Ray Spectroscopy
ESC	Electrolyte-Supported Cell
FEM	Finite Element Modeling
FESC	Fuel Electrode-Supported Cell
G'	Solid-Like Behavior
G''	Liquid-Like Behavior
GDC	Gadolinium Doped Ceria
IC	Interconnect
IoE	Internet of Everything
I	Current
ITON	Nitrogen-Doped Indium Tin Oxide
LCC2	Lanthanum Calcium Chromium Cobalt Copper Oxide
LMS	Lanthanum Strontium Manganite
LSTF	Lanthanum and Iron Co-Doped Strontium Titanate

LSCF	Lanthanum Strontium Cobalt Ferrite
LSC	Lanthanum Strontium Cobaltite
LVR	Linear Viscoelastic Region
MCF	Manganese Cobalt Ferrite
MCFC	Molten Carbonate Fuel Cell
MIEC	Mixed Ionic and Electronic Conducting
MSC	Metal-Supported Cell
MASP	Magnetically Assisted Stencil Printing
nLVR	Non-Linear Viscoelastic Region
PAFC	Phosphoric Acid Fuel Cell
PEEC	Polymer Electrolyte Electrolyzer
PEFC	Polymer Electrolyte Fuel Cell
PSD	Particle Size Distribution
PZT	Lead Zirconate Titanate
rSOC	Reversible Solid Oxide Cell
ScCeSZ	Zirconia Co-Stabilized with Scandia And Ceria
SEM	Scanning Electron Microscopy
SOC	Solid Oxide Cell
SOEC	Solid Oxide Electrolysis Cell
SOFC	Solid Oxide Fuel Cells
SRU	Single Repeat Unit
V	Voltage
YSZ	Yttria-Stabilized Zirconia

## References

- [1] A. Hauch, R. Küngas, P. Blennow, A.B. Hansen, J.B. Hansen, B.V. Mathiesen, M.B. Mogensen, Recent advances in solid oxide cell technology for electrolysis, *Science* 370 (2020).
- [2] M.B. Mogensen, M. Chen, H.L. Frandsen, C. Graves, J.B. Hansen, K.V. Hansen, A. Hauch, T. Jacobsen, S.H. Jensen, T.L. Skaftø, X. Sun, Reversible solid-oxide cells for clean and sustainable energy, *Clean Energy* 3 (2019).
- [3] M. B. Mogensen, S. H. Jensen, A. Hauch, I. Chorkendorff, T. Jacobsen, Performance of reversible solid oxide cells: A review, *European Fuel Cell Forum* (2006).
- [4] L.G.J. (Bert) De Haart, S.B. Beale, R. Deja, L. Dittrich, T. Duyster, Q. Fang, S. Foit, S. Gross-Barsnick, N. Margaritis, U. de Haart, I. Hoven, N. Kruse, C. Lenser, Q. Ma, N.H. Menzler, D. Naumenko, M. Nohl, R. Peters, D. Sebold, F. Thaler, W. Tiedemann, I. Unachukwu, B.A. Varghese, V. Vibhu, I.C. Vinke, S.E. Wolf, S. Zhang, J. Zurek, L. Blum, Forschungszentrum Jülich – Current Activities in SOC Development, *ECS Trans.* 103 (2021) 299–305.
- [5] M.B. Mogensen, Materials for reversible solid oxide cells, *Current Opinion in Electrochemistry* 21 (2020) 265–273.
- [6] S. Harboe, A. Schreiber, N. Margaritis, L. Blum, O. Guillon, N.H. Menzler, Manufacturing cost model for planar 5 kWel SOFC stacks at Forschungszentrum Jülich, *International Journal of Hydrogen Energy* 45 (2020) 8015–8030.
- [7] C. Lenser, J. Zurek, D. Naumenko, C.-A. Thieu, J.-W. Son, U. de Haart, Q. Fang, L. Blum, N.H. Menzler, Performance analysis of a planar solid oxide fuel cell stack between 750 °C and 500 °C, *Journal of Power Sources* 474 (2020) 228671.
- [8] A. Weber, H. Geisler, FEM Model-Based Design Optimization of a Planar SOFC Interconnector Flowfield, *ECS Trans.* 91 (2019) 2233.
- [9] R. Spotorno, P. Piccardo, G. Schiller, Effect of Cathode Contacting on Anode Supported Cell Performances, *J. Electrochem. Soc.* 163 (2016) F872–F876.
- [10] J.W. Phair, Rheological Analysis of Concentrated Zirconia Pastes with Ethyl Cellulose for Screen Printing SOFC Electrolyte Films, *Journal of the American Ceramic Society* 91 (2008) 2130–2137.
- [11] P. Von Dollen, S. Barnett, A Study of Screen Printed Yttria-Stabilized Zirconia Layers for Solid Oxide Fuel Cells, *J American Ceramic Society* 88 (2005) 3361–3368.
- [12] T. Studnitzky, M. Dressler, M. Jurisch, K. Reuter, S. Riecker, B. Kieback, 3D Screen and Stencil Printing: Real Mass Production for Metals, Ceramics and their Combinations, *World PM* (2016).
- [13] J. Kloeser, K. Heinrich, E. Jung, L. Lauter, A. Ostmann, R. Aschenbrenner, H. Reichl, Low cost bumping by stencil printing: process qualification for 200 lm pitch, *Microelectronics Reliability* (2000) 9.
- [14] S. Mallik, J. Thieme, R. Bauer, N.N. Ekere, A. Seman, R. Bhatti, R. Durairaj, Study of the rheological behaviours of Sn-Ag-Cu solder pastes and their correlation with printing performance, in: 2009 11th Electronics Packaging Technology Conference, (2009) 869–874.
- [15] J. Pan, G.L. Tonkay, R.H. Storer, R.M. Sallade, D.J. Leandri, Critical variables of solder paste stencil printing for micro-BGA and fine pitch QFP, in: Twenty Fourth IEEE/CPMT International Electronics Manufacturing Technology Symposium (Cat. No.99CH36330), (1999) 94–101.
- [16] A. Gondolini, E. Mercadelli, A. Sangiorgi, A. Sanson, Integration of Ni-GDC layer on a NiCrAl metal foam for SOFC application, *Journal of the European Ceramic Society* 37 (2017) 1023–1030.
- [17] T. Siponkoski, M. Nelo, H. Jantunen, J. Juuti, A printable P(VDF-TrFE)-PZT Composite with Very High Piezoelectric Coefficient, *Applied Materials Today* 20 (2020) 100696.
- [18] J. Turner, G. Sverdrup, M.K. Mann, P.-C. Maness, B. Kroposki, M. Ghirardi, R.J. Evans, D. Blake, Renewable hydrogen production, *Int. J. Energy Res.* 32 (2008) 379–407.
- [19] I. Dincer, C. Acar, Review and evaluation of hydrogen production methods for better sustainability, *International Journal of Hydrogen Energy* 40 (2015) 11094–11111.

- [20] S.D. Ebbesen, S.H. Jensen, A. Hauch, M.B. Mogensen, High Temperature Electrolysis in Alkaline Cells, Solid Proton Conducting Cells, and Solid Oxide Cells, *Chem. Rev.* 114 (2014) 10697–10734.
- [21] A. Waegel, J. Byrne, D. Tobin, B. Haney, Hydrogen Highways: Lessons on the Energy Technology-Policy Interface, *Bulletin of Science, Technology & Society* 26 (2006) 288–298.
- [22] K. Oshiro, S. Fujimori, Role of hydrogen-based energy carriers as an alternative option to reduce residual emissions associated with mid-century decarbonization goals, *Applied Energy* 313 (2022) 118803.
- [23] S. Yousef, Hydrogen as a clean and sustainable energy for green future, *Sustain. Tech, Green Econ.* 1 (2021) 8–13.
- [24] S. Brauner, A. Lahnaoui, S. Agbo, S. Bösch, W. Kuckshinrichs, Towards green hydrogen? – A comparison of German and African visions and expectations in the context of the H<sub>2</sub>Atlas-Africa project, *Energy Strategy Reviews* 50 (2023) 101204.
- [25] N.H. Menzler, D. Schäfer, N. Kruse, R. Peters, F. Kunz, Solid Oxide Cells for Hydrogen Generation and Usage: From Materials to Systems, *Ceramic forum international* 100(3), (2023) 48–56.
- [26] I. Pilatowsky, R.J. Romero, C.A. Isaza, S.A. Gamboa, P.J. Sebastian, W. Rivera, *Cogeneration Fuel Cell-Sorption Air Conditioning Systems*, Springer London, (2011).
- [27] S. Hussain, L. Yangping, Review of solid oxide fuel cell materials: cathode, anode, and electrolyte, *Energy Transit* 4 (2020) 113–126.
- [28] Y.S. Ayhan, A. Buyukaksoy, Impact of fabrication temperature on the stability of yttria doped bismuth oxide ceramics, *Solid State Ion.* 338 (2019) 66–73.
- [29] K. Kendall, M. Kendall, *High-temperature solid oxide fuel cells for the 21st century: fundamentals, design and applications*, Academic Press is an imprint of Elsevier, London, (2016).
- [30] F. Tietz, H.-P. Buchkremer, D. Stöver, 10 years of materials research for solid oxide fuel cells at forschungszentrum jülich, *J Electroceram* 17 (2006) 701–707.
- [31] S. Yang, J. Gao, M. Trini, S. De Angelis, P.S. Jørgensen, J.R. Bowen, L. Zhang, M. Chen, Ni coarsening in Ni-yttria stabilized zirconia electrodes: Three-dimensional quantitative phase-field simulations supported by ex-situ ptychographic nano-tomography, *Acta Materialia* 246 (2023) 118708.
- [32] J.D. Kirtley, M.D. McIntyre, D.M. Halat, R.A. Walker, Insights into SOFC Ni/YSZ Anode Degradation Using In-Situ Spectrochronopotentiometry, *ECS Trans.* 50 (2013) 3–15.
- [33] A. Hauch, A. Hagen, J. Hjelm, T. Ramos, Sulfur Poisoning of SOFC Anodes: Effect of Overpotential on Long-Term Degradation, *J. Electrochem. Soc.* 161 (2014) F734–F743.
- [34] T. Namioka, T. Naruse, R. Yamane, Behavior and mechanisms of Ni/ScSZ cermet anode deterioration by trace tar in wood gas in a solid oxide fuel cell, *International Journal of Hydrogen Energy* 36 (2011) 5581–5588.
- [35] K. Sick, N. Grigorev, N.H. Menzler, O. Guillon, Development of cathode contacting for SOFC stacks, *Ceramic Engineering and Science Proceedings* (2009) 39 - 2.
- [36] L. Blum, An Analysis of Contact Problems in Solid Oxide Fuel Cell Stacks Arising from Differences in Thermal Expansion Coefficients, *Electrochimica Acta* 223 (2017) 100–108.
- [37] J.N. Davis, K.F. Ludwig, K.E. Smith, J.C. Woicik, S. Gopalan, U.B. Pal, S.N. Basu, Surface Segregation in Lanthanum Strontium Manganite Thin Films and Its Potential Effect on the Oxygen Reduction Reaction, *J. Electrochem. Soc.* 164 (2017) F3091–F3096.
- [38] E. Bucher, W. Sitte, F. Klauser, E. Bertel, Oxygen exchange kinetics of La<sub>0.58</sub>Sr<sub>0.4</sub>Co<sub>0.2</sub>Fe<sub>0.8</sub>O<sub>3</sub> at 600°C in dry and humid atmospheres, *Solid State Ionics* 191 (2011) 61–67.
- [39] D. Rembelski, J.P. Viricelle, L. Combemale, M. Rieu, Characterization and Comparison of Different Cathode Materials for SC-SOFC: LSM, BSCF, SSC, and LSCF, *Fuel Cells* 12 (2012) 256–264.
- [40] M. Riegraf, F. Han, N. Sata, R. Costa, Intercalation of Thin Film Gd-doped Ceria Barrier Layers in Electrolyte Supported Solid Oxide Cells: Physico-chemical Aspects, *ACS Appl. Mater. Interfaces* 13, (2021) 37239–37251.

- [41] J. Railsback, S.H. Choi, S.A. Barnett, Effectiveness of dense Gd-doped ceria barrier layers for (La,Sr)(Co,Fe)O<sub>3</sub> cathodes on Yttria-stabilized zirconia electrolytes, *Solid State Ionics* 335 (2019) 74–81.
- [42] R. Knibbe, J. Hjelm, M. Menon, N. Pryds, M. Søgaaard, H.J. Wang, K. Neufeld, Cathode–Electrolyte Interfaces with CGO Barrier Layers in SOFC, *Journal of the American Ceramic Society* 93 (2010) 2877–2883.
- [43] P. Huczowski, N. Christiansen, V. Shemet, L. Niewolak, J. Piron-Abellan, L. Singheiser, W.J. Quadackers, Growth Mechanisms and Electrical Conductivity of Oxide Scales on Ferritic Steels Proposed as Interconnect Materials for SOFC's, *Fuel Cells* 6 (2006) 93–99.
- [44] N.H. Menzler, D. Sebold, E. Wessel, Interaction of La<sub>0.58</sub>Sr<sub>0.40</sub>Co<sub>0.20</sub>Fe<sub>0.80</sub>O<sub>3-δ</sub> cathode with volatile Cr in a stack test – Scanning electron microscopy and transmission electron microscopy investigations, *Journal of Power Sources* 254 (2014) 148–152.
- [45] M.V.F. Schlupp, J.W. Kim, A. Brevet, C. Rado, K. Couturier, U.F. Vogt, F. Lefebvre-Joud, A. Züttel, Avoiding chromium transport from stainless steel interconnects into contact layers and oxygen electrodes in intermediate temperature solid oxide electrolysis stacks, *Journal of Power Sources* 270 (2014) 587–593.
- [46] N. Grünwald, D. Sebold, Y.J. Sohn, N.H. Menzler, R. Vaßen, Self-healing atmospheric plasma sprayed Mn<sub>1.0</sub>Co<sub>1.9</sub>Fe<sub>0.1</sub>O<sub>4</sub> protective interconnector coatings for solid oxide fuel cells, *Journal of Power Sources* 363 (2017) 185–192.
- [47] X. Montero, F. Tietz, D. Sebold, H.P. Buchkremer, A. Ringuede, M. Cassir, A. Laresgoiti, I. Villarreal, MnCo<sub>1.9</sub>Fe<sub>0.1</sub>O<sub>4</sub> spinel protection layer on commercial ferritic steels for interconnect applications in solid oxide fuel cells, *Journal of Power Sources* 184 (2008) 172–179.
- [48] N.K. Karri, B.J. Koepfel, B.N. Nguyen, K. Lai, Structural Reliability of Cathode Contact Materials in Planar SOFCs, *ECS Trans.* 78 (2017) 1701–1712.
- [49] J. Tong, X. Du, M. Han, The Development of Sealant for Planar SOFC, *ECS Transactions* 57 (2013) 2395–2401.
- [50] N. Margaritis, L. Blum, P. Batfalsky, D. Bohmann, S. Ceschini, Q. Fang, D. Federmann, J. Kroemer, R. Peters, R. Steinberger-Wilckens, Status of Light Weight Cassette Design of SOFC, *ECS Trans.* 68 (2015) 209–220.
- [51] F. Grimm, Charakterisierung des Werkstoffverhaltens während des Kosinterns einer neuartigen, inert gestützten Festoxidbrennstoffzelle, *Forschungszentrum Jülich GmbH Zentralbibliothek, Verlag, Jülich*, (2020).
- [52] F. Han, N. Sata, M. Riegraf, F.-M. Fuchs, R. Semerad, C. Geipel, C. Walter, R. Costa, Thin-Film Gd-Doped Ceria Sr-Barrier Layers for Electrolyte Supported SOFCs, *ECS Trans.* 91 (2019) 1157–1163.
- [53] F. Grimm, N.H. Menzler, O. Guillon, Selection of cathode materials for forsterite supported solid oxide fuel cells – Part I: Materials interactions, *Journal of Power Sources* 451 (2020) 227607.
- [54] S. Opakhai, K. Kuterbekov, Metal-Supported Solid Oxide Fuel Cells: A Review of Recent Developments and Problems, *Energies* 16 (2023) 4700.
- [55] D. Udomsilp, J. Rechberger, R. Neubauer, C. Bischof, F. Thaler, W. Schafbauer, N.H. Menzler, L.G.J. de Haart, A. Nenning, A.K. Opitz, O. Guillon, M. Bram, Metal-Supported Solid Oxide Fuel Cells with Exceptionally High-Power Density for Range Extender Systems, *Cell Reports Physical Science* 1 (2020).
- [56] W. Schafbauer, N.H. Menzler, H.P. Buchkremer, Tape Casting of Anode Supports for Solid Oxide Fuel Cells at Forschungszentrum Jülich, *International Journal of Applied Ceramic Technology* 11 (2014) 125–135.
- [57] N.H. Menzler, J. Malzbender, P. Schoderböck, R. Kauert, H.P. Buchkremer, Sequential Tape Casting of Anode-Supported Solid Oxide Fuel Cells, *Fuel Cells* 14 (2014) 96–106.
- [58] R.K. Nishihara, P.L. Rachadel, M.G.N. Quadri, D. Hotza, Manufacturing porous ceramic materials by tape casting—A review, *Journal of the European Ceramic Society* 38 (2018) 988–1001.



- [59] N.A. Baharuddin, N.F. Abdul Rahman, H. Abd. Rahman, M.R. Somalu, M.A. Azmi, J. Raharjo, Fabrication of high-quality electrode films for solid oxide fuel cell by screen printing: A review on important processing parameters, *Int J Energy Res* 44 (2020) 8296–8313.
- [60] O. Vazquez-Mena, L. Gross, S. Xie, L.G. Villanueva, J. Brugger, Resistless nanofabrication by stencil lithography: A review, *Microelectronic Engineering* 132 (2015) 236–254.
- [61] U. Zschieschang, J.W. Borchert, M. Geiger, F. Letzkus, J.N. Burghartz, H. Klauk, Stencil lithography for organic thin-film transistors with a channel length of 300 nm, *Organic Electronics* 61 (2018) 65–69.
- [62] A. Barnabé, M. Lalanne, L. Presmanes, J.M. Soon, Ph. Tailhades, C. Dumas, J. Grisolia, A. Arbouet, V. Paillard, G. BenAssayag, M.A.F. van den Boogaart, V. Savu, J. Brugger, P. Normand, Structured ZnO-based contacts deposited by non-reactive rf magnetron sputtering on ultra-thin SiO<sub>2</sub>/Si through a stencil mask, *Thin Solid Films* 518, (2009), 1044–1047.
- [63] A.J. Medesi, F. Hagedorn, M. Schepperle, C. Megnin, T. Hanemann, The co-casting process: A new manufacturing process for ceramic multilayer devices, *Sensors and Actuators A: Physical* 251 (2016) 266–275.
- [64] Y. Li, C. Hui, M. Wu, Y. Li, Y. Wang, Textured (K<sub>0.5</sub>Na<sub>0.5</sub>)NbO<sub>3</sub> ceramics prepared by screen-printing multilayer grain growth technique, *Ceramics International* 38 (2012) S283–S286.
- [65] X. Zhao, R. Wang, Y. Liu, X. Deng, H. Jiang, W. Zhang, High temperature thermoelectric properties of nitrogen doped ITO thin films, *Vacuum* 172 (2020) 109054.
- [66] D. Manassis, R. Patzelt, A. Ostmann, R. Aschenbrenner, H. Reichl, Technical challenges of stencil printing technology for ultra fine pitch flip chip bumping, *Microelectronics Reliability* 44 (2004) 797–803.
- [67] E.H. Amalu, N.N. Ekere, S. Mallik, Evaluation of rheological properties of lead-free solder pastes and their relationship with transfer efficiency during stencil printing process, *Materials & Design* 32 (2011) 3189–3197.
- [68] N. Khader, J. Lee, D. Lee, S.W. Yoon, H. Yang, Multi-objective optimization approach to enhance the stencil printing quality, *Procedia Manufacturing* 38 (2019) 163–170.
- [69] T.-N. Tsai, Improving the fine-pitch stencil printing capability using the Taguchi method and Taguchi fuzzy-based model, *Robotics and Computer-Integrated Manufacturing* 27 (2011) 808–817.
- [70] N. Khader, S.W. Yoon, Online control of stencil printing parameters using reinforcement learning approach, *Procedia Manufacturing* 17 (2018) 94–101.
- [71] A. Lofti, M. Howarth, Industrial application of fuzzy systems: Adaptive fuzzy control of solder paste stencil printing, *Information Sciences* 107 (1998) 273–285.
- [72] W.E. Coleman, Two Print Stencils Systems, Photo Stencil, Colorado Springs, CO (Year not defined).
- [73] B. Illés, O. Krammer, A. Géczy, Introduction to surface-mount technology, in: *Reflow Soldering*, Elsevier (2020) 1–62.
- [74] O. Krammer, L.M. Molnár, L. Jakab, A. Szabó, Modelling the effect of uneven PWB surface on stencil bending during stencil printing process, *Microelectronics Reliability* 52 (2012) 235–240.
- [75] R. Durairaj, S. Ramesh, S. Mallik, A. Seman, N. Ekere, Rheological characterisation and printing performance of Sn/Ag/Cu solder pastes, *Materials & Design* 30 (2009) 3812–3818.
- [76] T.A. Nguty, N.N. Ekere, A. Adebayo, Correlating solder paste composition with stencil printing performance, in: *Twenty Fourth IEEE/CPMT International Electronics Manufacturing Technology Symposium* (Cat. No.99CH36330) (1999) 304–312.
- [77] J.C. Li, Y. Wang, D.C. Ba, Characterization of Semiconductor Surface Conductivity by Using Microscopic Four-Point Probe Technique, *Physics Procedia* 32 (2012) 347–355.
- [78] R. Steinberger-Wilckens, L.G.J. Haart, I.C. Vinke, L. Blum, A. Cramer, J. Remmel, G. Blass, F. Tietz, W.J. Quadackers, Recent Results of Stack Development at Forschungszentrum Jülich, in: N. Sammes, A. Smirnova, O. Vasylyev (Eds.), *Fuel Cell Technologies: State and Perspectives*, Springer-Verlag, Berlin/Heidelberg (2005) 123–134.

- [79] K. Sick, N. Grigorev, N.H. Menzler, O. Guillon, Development of Cathode Contacting for SOFC Stacks, in: J. Salem, D. Koch, P. Mechnich, M. Kusnezoff, N. Bansal, J. LaSalvia, P. Balaya, Z. Fu, T. Ohji (Eds.), *Ceramic Engineering and Science Proceedings*, John Wiley & Sons, Inc., Hoboken, NJ, USA, (2019) 99–111.
- [80] E. Ostrovskiy, Y.-L. Huang, E.D. Wachsman, Effects of surface chemical potentials on cation segregation, *J. Mater. Chem. A* 9 (2021) 1593–1602.
- [81] H.-W. Lin, C.-P. Chang, W.-H. Hwu, M.-D. Ger, The rheological behaviors of screen-printing pastes, *Journal of Materials Processing Technology* 197 (2008) 284–291.
- [82] H.G. Merkus, *Particle size measurements: fundamentals, practice, quality*, 1. Ed, Springer, Dordrecht, (2009).
- [83] C.O.R. Abbireddy, C.R.I. Clayton, A review of modern particle sizing methods, *Proceedings of the Institution of Civil Engineers - Geotechnical Engineering* 162 (2009) 193–201.
- [84] A. Papadopoulou, J.J.J. Gillissen, M.K. Tiwari, S. Balabani, Effect of Particle Specific Surface Area on the Rheology of Non-Brownian Silica Suspensions, *Materials* 13 (2020) 4628.
- [85] A. Ul-Hamid, *A Beginners' Guide to Scanning Electron Microscopy*, Springer International Publishing, Cham (2018).
- [86] A.V. Girão, G. Caputo, M.C. Ferro, Application of Scanning Electron Microscopy–Energy Dispersive X-Ray Spectroscopy (SEM-EDS), in: *Comprehensive Analytical Chemistry*, Elsevier (2017) 153–168.
- [87] B.V.R. Tata, B. Raj, Confocal laser scanning microscopy: Applications in material science and technology, *Bull Mater Sci* 21 (1998) 263–278.
- [88] S. Aravamudhan, D. Santos, G. Pham-Van-Diep, F. Andres, A study of solder paste release from small stencil apertures of different geometries with constant volumes, in: *27th Annual IEEE/SEMI International Electronics Manufacturing Technology Symposium* (2002) 159–165.
- [89] S.H. Mannan, N.N. Ekere, I. Ismail, M.A. Currie, Flow processes in solder paste during stencil printing for SMT assembly, *J Mater Sci: Mater Electron* 6 (1995).
- [90] K. Drabczyk, P. Panek, Influence of screen-printing parameters on the front metallic electrodes geometry of solar cells, *Circuit World* 40 (2014) 23–26.
- [91] S. Murakami, K. Ri, T. Itoh, N. Izu, W. Shin, K. Inukai, Y. Takahashi, Y. Ando, Effects of ethyl cellulose polymers on rheological properties of (La,Sr)(Ti,Fe)O<sub>3</sub>-terpineol pastes for screen printing, *Ceramics International* 40 (2014) 1661–1666.
- [92] S. Lee, U. Paik, S.-M. Yoon, J.-Y. Choi, Dispersant-Ethyl Cellulose Binder Interactions at the Ni Particle-Dihydroterpineol Interface, *J American Ceramic Society* 89 (2006) 3050–3055.
- [93] U. Paik, V.A. Hackley, H.-W. Lee, Dispersant-Binder Interactions in Aqueous Silicon Nitride Suspensions, *Journal of the American Ceramic Society* 82 (1999) 833–840.
- [94] A. Tsetsekou, C. Agrafiotis, I. Leon, A. Milias, Optimization of the rheological properties of alumina slurries for ceramic processing applications Part II: Spray-drying, *Journal of the European Ceramic Society* 21 (2001) 493–506.
- [95] M.R. Somalu, V. Yufit, N.P. Brandon, The effect of solids loading on the screen-printing and properties of nickel/scandia-stabilized-zirconia anodes for solid oxide fuel cells, *International Journal of Hydrogen Energy*, Volume 38, Issue 22 (2013) 9500–9510.
- [96] Z. Chen, J. Li, C. Liu, Y. Liu, J. Zhu, C. Lao, Preparation of high solid loading and low viscosity ceramic slurries for photopolymerization-based 3D printing, *Ceramics International* 45 (2019) 11549–11557.
- [97] G. Tari, J.M.F. Ferreira, A.T. Fonseca, O. Lyckfeldt, Influence of particle size distribution on colloidal processing of alumina, *Journal of the European Ceramic Society* 18 (1998) 249–253.
- [98] S.M. Olhero, J.M.F. Ferreira, Influence of particle size distribution on rheology and particle packing of silica-based suspensions, *Powder Technology* 139 (2004) 69–75.
- [99] P.F. Luckham, M.A. Ukeje, Effect of Particle Size Distribution on the Rheology of Dispersed Systems, *Journal of Colloid and Interface Science* 220 (1999) 347–356.

- [100] W. Shin, M. Nishibori, M. Ohashi, N. Izu, T. Itoh, I. Matsubara, Ceramic catalyst combustors of Pt-loaded-alumina on microdevices, *J. Ceram. Soc. Japan* 117 (2009) 659–665.
- [101] V. Thoréton, M. Niania, J. Druce, H. Tellez, J.A. Kilner, Oxygen Diffusion in Ceramic Mixed Conducting  $\text{La}_{0.6}\text{Sr}_{0.4}\text{Co}_{0.2}\text{Fe}_{0.8}\text{O}_{3-\delta}$ : The Role of Grain and Twin Boundaries, *J. Electrochem. Soc.* 169 (2022) 044513.
- [102] A. Ansar, D. Soysal, Z. Ilhan, N. Wagner, S. Wolf, R. Ruckdäschel, Improving Stoichiometry and Processing of LSCF Oxygen Electrode for SOFC, *ECS Trans.* 25 (2009) 2443–2453.
- [103] K. Inukai, Y. Takahashi, K. Ri, W. Shin, Rheological analysis of ceramic pastes with ethyl cellulose for screen-printing, *Ceramics International* 41 (2015) 5959–5966.
- [104] J.H. Zhu, H. Ghezel-Ayagh, Cathode-side electrical contact and contact materials for solid oxide fuel cell stacking: A review, *International Journal of Hydrogen Energy* 42 (2017) 24278–24300.
- [105] R.R. Lathrop, Solder paste print qualification using laser triangulation, *IEEE Transactions on Components, Packaging, and Manufacturing Technology: Part C* 20 (1997) 174–182.
- [106] D.A. Rau, C.B. Williams, M.J. Bortner, Rheology and printability: A survey of critical relationships for direct ink write materials design, *Progress in Materials Science* 140 (2023) 101188.
- [107] I. Masalova, M. Taylor, E. Kharatiyan, A.Ya. Malkin, Rheopexy in highly concentrated emulsions, *Journal of Rheology* 49 (2005) 839–849.
- [108] A. Potanin, Thixotropy and rheopexy of aggregated dispersions with wetting polymer, *Journal of Rheology* 48 (2004) 1279–1293.
- [109] E. N'gouamba, M. Essadik, J. Goyon, T. Oerther, P. Coussot, Yielding and rheopexy of aqueous xanthan gum solutions, *Rheol. Acta* 60 (2021) 653–660.
- [110] J. Kim, Y.-J. Choi, C.W. Gal, H. Park, S.-Y. Yoon, H. Yun, Effect of dispersants on structural integrity of 3D printed ceramics, *International Journal of Applied Ceramic Technology* 19 (2022) 968–978.
- [111] I. Kim, S. Kim, A. Andreu, J.-H. Kim, Y.-J. Yoon, Influence of dispersant concentration toward enhancing printing precision and surface quality of vat photopolymerization 3D printed ceramics, *Additive Manufacturing* 52 (2022) 102659.
- [112] M.S. Kalamaki, A.L.T. Powell, K. Struijs, J.M. Labavitch, D.S. Reid, A.B. Bennett, Transgenic Overexpression of Expansin Influences Particle Size Distribution and Improves Viscosity of Tomato Juice and Paste, *J. Agric. Food Chem.* 51 (2003) 7465–7471.
- [113] B. Yoo, M.A. Rao, Effect of unimodal particle size and pulp content on rheological properties of tomato puree, *Journal of Texture Studies* 25 (1994) 421–436.
- [114] A. Khecho, S.A. Ghaffari, B. Eftekhari Yekta, The influence of particle size distribution on rheological properties of fused silica pastes for direct ink writing, *Int J Applied Ceramic Tech* (2022) 14109.
- [115] R. Greenwood, P.F. Luckham, T. Gregory, The Effect of Diameter Ratio and Volume Ratio on the Viscosity of Bimodal Suspensions of Polymer Latexes, *Journal of Colloid and Interface Science* 191 (1997) 11–21.
- [116] M.G. Rasteiro, E. Antunes, Correlating the Rheology of PVC-Based Pastes with Particle Characteristics, *Particulate Science and Technology* 23 (2005) 361–375.
- [117] H.I. Geisler, Finite Element Method (FEM) Model and Performance Analysis of Solid Oxide Fuel Cells. Karlsruhe: KIT Scientific Publishing (2019).

## Index of Figures

Figure 1 a) SEM images showing actual non-ideal contact between the interconnect and the cell with a schematic illustration of a single repeat unit, b) SEM image of newly stencil printed layer with improved surface flatness coupled with the schematic illustration of a novel design in a single repeat unit of a stack .....	7
Figure 2 Schematic illustration of the working principles of solid oxide electrolysis cells (left) and solid oxide fuel cells (right).....	10
Figure 3 I-V curve for the ideal and actual performance of a fuel cell [26] .....	11
Figure 4 Conductivity of oxygen ion conductors at different temperatures. $\text{La}_{0.8}\text{Sr}_{0.2}\text{Ga}_{0.9}\text{Mg}_{0.1}\text{O}_{3-\delta}$ (LSGM), $\text{Zr}_{0.84}\text{Y}_{0.16}\text{O}_{1.92}$ (8YSZ), $\text{Na}_{0.5}\text{Bi}_{0.49}\text{Ti}_{0.98}\text{Mg}_{0.02}\text{O}_3$ (NBT), $\text{Ce}_{0.9}\text{Nd}_{0.1}\text{O}_{1.95}$ (CND), $\text{Bi}_2\text{O}_3$ and $\text{La}_{10}\text{Si}_{5.8}\text{Mg}_{0.3}\text{O}_{26.8}$ (Apatite) [29] .....	13
Figure 5 Cross-sectional schematic of a single repeat unit for SOCs .....	15
Figure 6 Relative contribution of SOC elements on the cell impedance within a stack at different temperatures [7].....	16
Figure 7 Schematic representation of SOFC cell types. Green, purple, and blue stand for functional layers of anode, electrolyte, and cathode, respectively [51] .....	17
Figure 8 Typical illustration of a tape casting setup [58].....	18
Figure 9 Schematic illustration of screen printing [59] .....	18
Figure 10 (a) 2D view of ZnO patterns deposited by stencil lithography; (b) 3D profile of the same patterns; (c) thickness of these two ZnO profiles [62].....	19
Figure 11 (left) Flowchart of the deposition steps for the anodic layer; (right) printed and sintered anodic layer on metal foam [16] .....	20
Figure 12 Stencil printed ITON/Pt thin film thermocouple on alumina substrate [65] .....	21
Figure 13 Schematic illustration of the collinear four-point probe measurement setup in macro (left) and micro (right) scale [77].....	22
Figure 14 a) PSD of LCC2 raw powder after the spray drying process, b) PSD of LCC2 raw powder after 2 hours of ball milling .....	29
Figure 15 Paste preparation routes for a) Pastes P1 to P5 and b) Paste P6 .....	31
Figure 16 Rheological results of a) pastes P1 to P5 with their flow curves, b) paste P6 with its flow curve, c) pastes P2 and P3 with a plot for their viscoelastic behavior, d) paste P6 with a plot for its viscoelastic behavior and e) paste P6 with a plot for its time-dependent behavior .....	35
Figure 17 Printed stripes from a) paste P1 and b) paste P4 after drying in a furnace .....	36
Figure 18 SEM images of Paste a) P2, b) P3, and c) P5 under Print A conditions, d) SEM image of paste P5 under Print A-5 conditions .....	36
Figure 19 Left) Stencil clogging due to the extreme tackiness of paste P5; right) An almost empty substrate surface after printing .....	38
Figure 20 SEM images of paste P3 printed under four different printing conditions listed in Table 6. a) was under Print A-1, b) was under Print A-2, c) was under Print A-3 and d) was under Print A-4 printed.....	39
Figure 21 Characterization of paste P6 under confocal laser microscopy in profile mode after printing under Print B conditions (dried at 60 °C overnight) .....	41
Figure 22 PSD of a) SP319-1 raw powder, b) SP325-3 raw powder, c) SP325-3 ball milled (BM) for 2 minutes, d) SP325-3 BM for 30 minutes, e) SP325-3 BM for 2 hours .....	44

Figure 23 Paste preparation routes of a) Paste of David and Paste X1; b) the rest of the pastes listed in Table 8 .....	47
Figure 24 Printed ribs of Paste X3v2 under a laser microscope; a) after 20 sec. waiting time before separation of the substrate from the stencil, b) direct separation after printing (printed ribs were in a dried state).....	50
Figure 25 Printed and heat-treated rib under SEM (a and b) and its elemental analysis was studied by EDS (c).....	51
Figure 26 Printed and heat-treated stripes under white light topography. Highlighted area with red rectangle to show surface roughness of the ribs .....	52
Figure 27 Results of rheology measurements for paste X3v2 showing a) flow curve, b) viscoelastic behavior, and c) time-dependent behavior .....	53
Figure 28 Particle size distribution of a) OSB-a, b) OSB-b, c) OSB-c, d) Paste X3v2, e) Paste X1. Paste formulations can be seen in Table 8 .....	55
Figure 29 Printed and dried ribs under laser microscope with profile mode; from left to right OSB-b, OSB-c and Paste X3v2 (the latter is included here for ease of comparison) .....	56
Figure 30 Rheological characterization of prepared pastes of OSB a, b, and c. From left to right: Plot of flow curves, viscoelastic behavior, and time-dependent behavior .....	56
Figure 31 Rheology of paste X3v1 - From left to right; Flow curve; Viscoelastic behavior; Time-dependent behavior.....	57
Figure 32 Characterization results of printed paste X3v1 under laser microscope in profile mode.....	58
Figure 33 PSD of paste X3v1 .....	59
Figure 34 Characterization of printed and dried rib of paste X4 under laser microscope in profile mode	60
Figure 35 Characterization of printed and dried ribs under a laser microscope in profile mode, a) original one, b) reproduced .....	61
Figure 36 Rheologic characterization of reproduced paste X3v2 with a) first attempt and b) second attempt, and from left to right the same for a and b: flow behavior, viscoelastic behavior, time-dependent behavior.....	62
Figure 37 SEM images of printed and heat-treated ribs; a) from Dr. Udomsilp's work, b) reproducibility experiment .....	63
Figure 38 a) Stencil-printed LSCF rib and b) screen-printed LSCF cathode on a porous alumina substrate which was drilled for the wire contact.....	66
Figure 39 I-V curves of both a) stencil-printed LSCF rib and b) screen-printed LSCF cathode on the porous alumina substrate at 800 °C.....	67
Figure 40 Tape adhesion test on printed and heat-treated ribs .....	68

## Index of Tables

Table 1 Properties of some SOC materials [35].....	14
Table 2 Particle sizes of LCC2 as raw and 2 hours ball-milled powder .....	30
Table 3 Compositions of prepared pastes.....	31
Table 4 Listed printing parameters under Print A conditions for pastes P1 to P5, and Print 2 conditions for paste P6 .....	32
Table 5 Varied printing parameters of Print A .....	32
Table 6 Thickness values of printed ribs from paste P3 under four different printing conditions .....	39
Table 7 Particle sizes and BET values of the powders shown are listed here in the same order as in Figure 22.....	45
Table 8 Contents of the recipes for the prepared pastes are listed below .....	46
Table 9 Schematical illustration of two different stencils .....	48
Table 10 Listed printing parameters in two different setups .....	48

## Acknowledgments

Improvements in any field/area of science/technology should enhance the beauty of life, which is intimately connected to the value of people who can smile and preserve that beauty. During my PhD studies, I was inspired by many smiles of people who contributed to my work, enabling me to complete this thesis successfully.

I would like to take this opportunity to express my sincere gratitude to my PhD advisor and day-to-day supervisor, Hon.-Prof. Dr.-Ing. Norbert H. Menzler, for his technical support and the countless discussions and meetings that significantly improved my research. I also sincerely thank Prof. Dr. Olivier Guillon, the head of IEK-1, for his valuable feedback on my work reports, which enriched my research.

I also want to convey my sincere appreciation to Dr. Christian Lenser, Dr. Robert Mücke, and Dr. Mariya Ivanova for their guidance and support throughout my PhD studies. Additionally, I am grateful to my colleagues at IEK-1, especially Werner Herzhof, Jan-Philipp Treitz, Volker Bader, Erhan Sucuoglu, Dr. Martin Juckel, Dr. Christian Dellen, Michael Xhonneux, Dr. Emine Bakan, Franziska E. Winterhalder, Laura-Elena Schäfer, Stephan Sarner, Denise Ramler, Maheshwar R. Bagathi, Fadi H. Al-Jaljouli, Martin Hilger, Kaouther Toudjine, and Dima Abubaker, who made this PhD journey more rewarding.

I am grateful to Prof. Jesus Gonzalez-Julian for being in my defense committee and to the Doctoral Committee of the Faculty of Georesources and Materials Engineering for their support during my PhD process.

I would also like to acknowledge the financial support from the BMBF under the project name "WirLebenSOFC" (FKZ 03FS0622B) and thank my colleagues from the project partners: Bosch GmbH, RIL Micro & Analytic GmbH, Karlsruhe Institute of Technology (KIT), Hochschule Karlsruhe, and Hochschule Aalen.

Last but not least, I would like to thank my wife, Miraç, for her support and for taking on additional responsibilities to make my work life easier. As a father of two children, Mehmet Fatih and Ahmet Selim, I hope to inspire others that pursuing a PhD with children is possible. My nucleus and big family hold an important place in my life, so my deepest gratitude goes to my mother, Sibel, my father, Mustafa, and all the other family members who have supported me.

Band / Volume 638

**Modellgestützte Analyse zukünftigen Mobilitätsverhaltens**

J. P. Reul (2024), XVI, 291 pp

ISBN: 978-3-95806-771-4

Band / Volume 639

**Insights into Mechanisms of Secondary Organic Aerosol Formation:  
Approaching Atmospherically Relevant Conditions  
in an Atmospheric Reaction Chamber**

Y. Baker (2024), XVII, 122 pp

ISBN: 978-3-95806-776-9

Band / Volume 640

**Advancing the representation of agricultural systems  
in Land Surface Models: systematic model evaluations  
and technical model developments**

T. S. Boas (2024), xxi, 145 pp

ISBN: 978-3-95806-777-6

Band / Volume 641

**Imaging spatial and temporal soil water content variations of the soil-plant  
continuum using ground penetrating radar**

L. Lärm (2024), xii, 303 pp

ISBN: 978-3-95806-778-3

Band / Volume 642

**Development of Iridium-based Nanostructures for Oxygen Evolution  
Reaction in PEM Water Electrolysis**

S. Park (2024), 135 pp

ISBN: 978-3-95806-779-0

Band / Volume 643

**Multi-dimensional GPR full-waveform inversion for small-scale  
hydrogeophysical soil characterization**

D. Hoven (2024), IX, 163 pp

ISBN: 978-3-95806-781-3

Band / Volume 644

**Analyse des Gastransports in komplexen Membransystemen durch  
Modellierung und multiskalige Simulation**

K. Wilkner (2024), VIII, 122 pp

ISBN: 978-3-95806-784-4



Band / Volume 645

**Deployment of Fuel Cell Vehicles in Road Transport and the  
Expansion of the Hydrogen Refueling Station Network: 2024 Update**

T. Grube; M. Rex (2024), iii, 26 pp

ISBN: 978-3-95806-786-8

Band / Volume 646

**Modellgestützte Analyse treibhausgasneutraler Transformationsstrategien  
für Deutschland**

T. F. Schöb (2024), XII, 228 pp

ISBN: 978-3-95806-789-9

Band / Volume 647

**Future Distribution Grids Using Geo-Referenced Synthetic Network  
Topologies**

A. Bandam (2024), ix, 237 pp

ISBN: 978-3-95806-790-5

Band / Volume 648

**Multi-scenario, high-resolution Lagrangian transport modeling for the  
analysis of the Asian tropopause aerosol layer**

J. H. Clemens (2024), 143 pp

ISBN: 978-3-95806-792-9

Band / Volume 649

**Prospektive Lebenszyklusanalysen von Power-to-Gas-Optionen**

J. C. Koj (2024), XVIII, 197 pp

ISBN: 978-3-95806-794-3

Band / Volume 650

**Assimilation of groundwater level and cosmic-ray neutron sensor soil  
moisture measurements into integrated terrestrial system models for  
better predictions**

F. Li (2024), xvii, 172 pp

ISBN: 978-3-95806-796-7

Band / Volume 651

**Integration of a rib-channel design to improve air-side contacting in solid  
oxide cell (SOC) stacks**

Y. S. Ayhan (2024), 82 pp

ISBN: 978-3-95806-797-4



Energie & Umwelt / Energy & Environment  
Band / Volume 651  
ISBN 978-3-95806-797-4